University of Oxford

Department of Engineering Science

Structure Engineering of Nitrogen Carriers for Chemical Looping Ammonia Synthesis



A thesis submitted for the degree of

Master of Science by Research in Engineering Science

Hangzuo Guo

Reuben College

Supervisors: Dr Binjian Nie, Professor Zhanfeng Cui

Trinity Term 2026

Declaration

The work described in this thesis was carried out in the Energy Storage and Energy Carriers Group, Department of Engineering Science, University of Oxford, primarily in the laboratories at the Institute of Advanced Technology, Begbroke Science Park, under the supervision of Dr Binjian Nie and Professor Zhanfeng Cui.

Except where otherwise stated, this thesis and the data reported are the results of my own work and has not been submitted, either in whole or in part, for any degree, diploma or other qualification at the University of Oxford or any other institution. All sources of information, data, figures, methods and materials from other authors have been properly acknowledged.

Hangzuo Guo

Trinity Term 2026

Acknowledgements

I am sincerely grateful to my supervisors, **Dr Binjian Nie** and **Professor Zhanfeng Cui**, for their invaluable guidance throughout this project. Their advice not only shaped the scientific direction of my work but also influenced my approach to research, responsibility, and long-term development. I am especially thankful for their patience, trust, and practical support during challenging periods of my study, when their assistance extended well beyond routine academic supervision.

I am also grateful to my family for their unwavering support. My parents have consistently provided advice, confidence, and care during my time away from home, and I thank my younger brother and sister for their encouragement throughout this period. I owe my deepest personal thanks to my wife, **Ms Chen Liu**. Her companionship, understanding, and patience have sustained both my research and daily life, particularly during times of pressure and uncertainty.

I would also like to thank my friends **Dr Xuefeng Lin, Dr Weiyu Deng, Dr Siyuan Dai** and **Ms Dan Zhang**. Their concern, advice and kindness have helped me in both my personal life and career development, and I am sincerely grateful for the time and care they have given me.

Finally, I thank my colleagues **Haoliang Hong** and **Zhenyu Zhou** for their discussions, suggestions, and practical help with my research. I am also grateful to the members of

the **Energy Storage and Energy Carriers Group** for providing a supportive research environment during my time at Oxford.

Table of Contents

Abstract vi
List of Figures x
List of Abbreviations xii
List of Publications xv
1. Introduction 1
1.1 Background 1
1.1.1 Energy and climate challenges 1
1.1.2 Hydrogen and hydrogen carriers 1
1.1.3 Ammonia as a hydrogen carrier 2
1.2 Ammonia synthesis pathways 4
1.2.1 Haber-Bosch process 4
1.2.2 Limitations of the Haber-Bosch process 4
1.2.3 Alternative ammonia synthesis pathways 5
1.3 Aims and objectives 8
2. Literature Review 12
2.1 System-level constraints of conventional ammonia synthesis 12
2.1.1 Energy and process coupling 12
2.1.2 Scale and decentralisation constraints 14
2.2 Alternative ammonia synthesis pathways 16
2.2.1 Thermocatalytic ammonia synthesis 20
2.2.2 Electrocatalytic ammonia synthesis 21
2.2.3 Photocatalytic ammonia synthesis 22
2.2.4 Plasma-assisted ammonia synthesis 23
2.2.5 Summary of alternative routes and transition to chemical looping 24
2.3 Chemical looping ammonia synthesis 25
2.3.1 Metal nitride-based pathways 28
2.3.2 Alkali and alkaline-earth metal imide-based pathway 31
2.3.3 Catalytic and structural optimisation 34
2.3.4 Reactor and system-level considerations 40
3. Methodology 45
3.1 Materials 46
3.2 Material preparation 48
3.2.1 Preparation of TM-promoted LiH composites 48
3.2.2 Preparation of supported LiH-based composites 51
3.3 Material characterisation 52
3.3.1 Scanning electron microscopy and energy-dispersive X-ray spectroscopy 53

3.3.2 X-ray diffraction 55
3.3.3 Transmission electron microscopy and TEM-EDS 56
3.3.4 X-ray photoelectron spectroscopy 58
3.4 Evaluation of CLAS performance 59
3.4.1 Test rig setup 60
3.4.2 Gas supply, flow control and temperature monitoring 61
3.4.3 CLAS testing procedure 63
3.4.4 Ammonia absorption and conductivity measurement 65
3.4.5 Main equipment and operating parameters 70
4. Results and Discussion 71
4.1 Initial morphology of LiH-based composites 72
4.2 Effect of transition metal promoter and loading 75
4.2.1 Screening of transition metal promoters 75
4.2.2 Effect of promoter loading 78
4.3 Support-assisted optimisation of Ni-LiH composites 83
4.3.1 Screening of support materials 84
4.3.2 Effect of TiO_2 loading 88
4.4 Phase evolution, local structure and surface state 91
4.4.1 XRD phase evolution during nitridation 92
4.4.2 SEM-EDS mapping of fresh, nitrided and hydrogenated TiO_2-Ni-LiH 97
4.4.3 TEM-EDS and HRTEM analysis of local structure 99
4.4.4 XPS analysis of surface states 106
4.5 Fixed-bed operating behaviour of Ni-LiH composites 110
4.5.1 Temperature effects in single- and two-temperature CLAS operation 110
4.5.2 Effect of nitridation and hydrogenation time 115
4.5.3 Effect of gas flow rate 118
4.5.4 Cycling behaviour of Ni-LiH composites 120
4.5.5 Effect of fixed-bed loading 124
4.6 Summary 128
5. Conclusions and Outlook 132
5.1 Main conclusions 132
5.2 Scope and limitations 135
5.3 Future research 139
References 148

Abstract

Chemical looping ammonia synthesis (CLAS) is a potential low-pressure route for ammonia production because it separates nitrogen fixation and ammonia-forming hydrogenation into sequential gas-solid steps. This separation can reduce the dependence on direct high-pressure N_2/H_2 synthesis and offers greater flexibility for modular ammonia production. However, CLAS remains limited by the reactivity, accessibility and cycling behaviour of solid nitrogen carriers. In LiH-based hydride-imide systems, efficient ammonia production requires not only nitrogen activation, but also effective contact among the transition metal promoter, LiH and the reacting gas phase.

This thesis investigates transition-metal-promoted and supported LiH-based composites for low-pressure CLAS. A lab-scale fixed-bed CLAS reactor was designed and fabricated for alternating N_2 and H_2 operation. Furnace-temperature calibration, gas-flow control, acid absorption and conductivity calibration enabled comparative ammonia quantification under controlled cycling conditions. Ball-milled LiH composites promoted with Ni, Co, Mn and Fe were prepared and tested. Among these promoters, Ni gave the highest activity. The Ni loading showed a non-monotonic dependence, with 50 wt.% Ni-LiH giving the best balance between metal-assisted nitrogen activation and effective LiH utilisation. At 300 °C under ambient pressure, 50 wt.% Ni-LiH produced approximately 1531 μmol NH_3 g_{LiH}^{-1} h^{-1}.

Parametric studies showed that Ni-LiH performed best around 300 °C. Separate nitridation and hydrogenation temperature control did not substantially improve the maximum rate over single-temperature operation. Longer nitridation increased the hydrogenation-accessible nitrogen inventory, higher gas flow improved ammonia release, and repeated cycling showed stable performance after an initial activation stage. Fixed-bed loading tests showed that higher powder loadings reduced material utilisation, highlighting the importance of gas-solid accessibility.

Support-assisted modification was then investigated by comparing oxide, carbon-based, and mineral supports, including TiO_2, SiO_2, expanded graphite, graphene nanoplatelets, and diatomaceous earth. Among these supports, TiO_2 consistently provided the greatest enhancement, with 10-15 wt.% TiO_2 representing the optimal performance range. The highest observed rate was approximately 2050 μmol NH_3 g_{LiH}^{-1} h^{-1} for 15 wt.% TiO_2. XRD indicated partial conversion of LiH to Li_2NH, with minor Li_3N detected in selected nitrided samples. SEM, TEM-EDS and HRTEM showed that TiO_2 changed compact agglomerated Ni-LiH particles into a more fragmented and granular microstructure and promoted spatial association among Ni-rich promoter domains, Ti/O-rich support regions, and N-containing LiH-derived reaction domains.

Overall, this work establishes a structure-engineering principle for LiH-based low-pressure chemical looping ammonia synthesis (CLAS). Achieving effective performance requires not only the selection of an active promoter, but also the combined optimisation of Ni-assisted N_2 activation, LiH-based hydride-imide nitrogen

storage, support-assisted particle structuring, and fixed-bed gas-solid transport. The TiO_2-Ni-LiH system serves as a practical model for developing more accessible hydride-imide nitrogen carriers for low-pressure ammonia synthesis. Furthermore, these findings indicate that future CLAS development should integrate material optimisation with reactor-bed design.

List of Tables

Table 1.1. Characteristics of hydrogen carriers [2, 10-14]. 3

Table 2.1. Energy efficiency and consumption for ammonia and hydrogen production [19, 26]. 13

Table 2.2. Ammonia synthesis is transitioning towards sustainable production approaches [18, 19]. 15

Table 2.3. Comparison of sustainable ammonia synthesis routes [21, 29-33]. 18

Table 2.4. The operating conditions and NH_3 production rate of various N carriers [21]. 35

Table 2.5. Comparative energy costs and technical parameters for ammonia production routes [130]. 44

Table 3.1. Materials. 47

Table 3.2. Main equipment and operating parameters used in the CLAS reactor system. 70

Table 4.1. XRD-estimated crystalline phase fractions of 10 wt.% TiO_2-50 wt.% Ni-LiH after different N_2 exposure times. 94

Table 4.2. XPS-estimated surface atomic composition of as-prepared 10 wt.% TiO_2-50 wt.% Ni-LiH. 108

List of Figures

Figure 1.1. Schematic illustration of the preparation and structural concept of TiO_2-supported Ni-LiH composites [20, 21]. 10

Figure 2.1. Conceptual process flow diagram for chemical looping ammonia synthesis. 26

Figure 2.2. Schematics of CLAS mediated by a metal nitride using **(a)** H_2O, **(b)** H_2 as hydrogen source. **(c)** CLAS mediated by an alkali metal. 27

Figure 3.1. Preparation of ball-milled LiH-based composites and representative photographs of the sample handling and milling equipment. 50

Figure 3.2. Lab-scale CLAS reactor system. 59

Figure 3.3. Sample loading configuration inside the CLAS reactor. 61

Figure 3.4. Calibration of furnace setpoint against reaction-zone temperature under Ar flow. 62

Figure 3.5. Conductivity calibration and temperature correction for NH_3 quantification. 68

Figure 4.1. SEM images of LiH and LiH-based composites. 73

Figure 4.2. NH_3 production rates of pure LiH and 50 wt.% TM-LiH composites under ambient pressure CLAS processes. 76

Figure 4.3. Comparison of the NH_3 production rates of 50 wt.% Ni-LiH and 50 wt.% Co-LiH at different reaction temperatures under ambient-pressure CLAS conditions. 77

Figure 4.4. Effect of Ni loading on NH_3 production rate over Ni-LiH composites at 300 °C. 79

Figure 4.5. Combined effect of Ni loading and reaction temperature on NH_3 production over Ni-LiH composites. 81

Figure 4.6. Effect of Co loading on NH_3 production rate over Co-LiH composites at 300 °C. 82

Figure 4.7. Effect of 10 wt.% support material on the NH_3 production rate of Ni-LiH composites under low-pressure CLAS conditions. 85

Figure 4.8. Effect of TiO_2 loading on the NH_3 production rate of TiO_2-Ni-LiH composites. 89

Figure 4.9. XRD patterns of 10 wt.% TiO_2-50 wt.% Ni-LiH after different N_2 exposure times during nitridation at 300 °C. 93

Figure 4.10. SEM-EDS maps of representative fresh, nitrided and hydrogenated TiO2-Ni-LiH samples. 98

Figure 4.11. HAADF-STEM image and EDS elemental maps of 10 wt.% TiO_2-50 wt.% Ni-LiH after 30 min N_2 exposure at 300 ℃. 100
Figure 4.12. Local EDS point analysis of 10 wt.% TiO_2-50 wt.% Ni-LiH after 30 min N_2 exposure at 300 ℃. 102
Figure 4.13. HRTEM lattice-fringe analysis of 10 wt.% TiO_2-50 wt.% Ni-LiH after 30 min N_2 exposure at 300 ℃. 104
Figure 4.14. XPS analysis of as-prepared 10 wt.% TiO_2-50 wt.% Ni-LiH before nitridation. 106
Figure 4.15. Effect of reaction temperature on NH_3 production rate over 50 wt.% Ni-LiH under single-temperature CLAS operation. 111
Figure 4.16. NH_3 production over 50 wt.% Ni-LiH under separate temperature control of nitridation and hydrogenation. 112
Figure 4.17. Effect of nitridation and hydrogenation time on NH_3 release over 50 wt.% Ni-LiH at 300 ℃. 116
Figure 4.18. Effect of gas flow on NH_3 production amount over 50 wt.% Ni-LiH. . 119
Figure 4.19. Cycling stability of 50 wt.% Ni-LiH under standard CLAS operation. 121
Figure 4.20. Cycling comparison of unsupported Ni-LiH and TiO_2-Ni-LiH composites under repeated CLAS operation after activation. 123
Figure 4.21. Effect of fixed-bed loading on the NH_3 production rate of 50 wt.% Ni-LiH. 125

List of Abbreviations

Abbreviation	Full term
AMH	Alkali/alkaline-earth metal hydride
AMNH	Alkali/alkaline-earth metal nitrogen-hydrogen system
AMNH-CLAS	Alkali/alkaline-earth metal nitrogen-hydrogen-mediated chemical looping ammonia synthesis
ASU	Air separation unit
at.%	Atomic percentage
BET	Brunauer-Emmett-Teller
CCS	Carbon capture and storage
CLAS	Chemical looping ammonia synthesis
DE	Diatomaceous earth
EDS	Energy-dispersive X-ray spectroscopy
EELS	Electron energy-loss spectroscopy
EG	Expanded graphite
EPR	Electron paramagnetic resonance
FFT	Fast Fourier transform
GHG	Greenhouse gas
GNP	Graphene nanoplatelets
H_2-CLAS	Hydrogen-mediated chemical looping ammonia synthesis
H_2O-CLAS	Water-mediated chemical looping ammonia synthesis
HAADF	High-angle annular dark-field
HAADF-STEM	High-angle annular dark-field scanning transmission electron microscopy
HB	Haber-Bosch
HHV	Higher heating value
HRTEM	High-resolution transmission electron microscopy
Li-N-H	Lithium-nitrogen-hydrogen species
LHV	Lower heating value
LH_2	Liquid hydrogen
MCH	Methylcyclohexane
SEM	Scanning electron microscopy
SMR	Steam methane reforming
STEM	Scanning transmission electron microscopy

Abbreviation	Full term
TEM	Transmission electron microscopy
TGA	Thermogravimetric analysis
TM	Transition metal
TRL	Technology readiness level
UV-vis	Ultraviolet-visible spectroscopy
wt.%	Weight percentage
XPS	X-ray photoelectron spectroscopy
XRD	X-ray diffraction

Chemical Formulas

Symbol	Full name / meaning
Ar	Argon
Al_2O_3	Aluminium oxide / alumina
BaH_2	Barium hydride
BaNH	Barium imide
CeO_2	Cerium dioxide / ceria
CH_3OH	Methanol
Co	Cobalt
Fe	Iron
H_2	Hydrogen
H_2O	Water
H_2SO_4	Sulfuric acid
LiH	Lithium hydride
Li_2NH	Lithium imide
$LiNH_2$	Lithium amide
Li_3N	Lithium nitride
Li_2O	Lithium oxide
MgO	Magnesium oxide
Mn	Manganese
N_2	Nitrogen
NH_3	Ammonia
Ni	Nickel
Ni-LiH	Nickel-promoted lithium hydride composite

Symbol	Full name / meaning
O_2	Oxygen
SiO_2	Silicon dioxide / silica
TiO_2	Titanium dioxide
TiO_{2-x}	Oxygen-deficient or reduced titanium dioxide
ZrO_2	Zirconium dioxide / zirconia

Nomenclature

Symbol	Description	Unit
n_{NH3}	Amount of ammonia produced or absorbed in the acid solution	μmol
$r_{NH3\text{-}m}$	Sample-normalised ammonia production rate	μmol g^{-1} h^{-1}
$r_{NH3\text{-}mLiH}$	LiH-normalised ammonia production rate	μmol g_{LiH}^{-1} h^{-1}
$\Delta\kappa_{corr}$	Dilution-corrected conductivity decrease used for ammonia quantification	μS cm^{-1}
κ_0	Initial conductivity of the dilute H_2SO_4 absorption solution	μS cm^{-1}
κ_{NH3}	Conductivity of the absorption solution after NH_3 absorption or ammonia addition	μS cm^{-1}
κ_{water}	Conductivity after adding the same volume of deionised water for blank correction	μS cm^{-1}
σ_T	Measured conductivity at temperature T before temperature correction	μS cm^{-1}
$\sigma_{displayed}$	Temperature-corrected conductivity displayed at the reference temperature	μS cm^{-1}
α	Temperature correction coefficient for conductivity	% $°C^{-1}$
T	Measurement temperature or reaction temperature	°C
T_{ref}	Reference temperature used for conductivity correction	°C
$t_{nitridation}$	Duration of the nitridation step under N_2	min or h
$t_{hydrogenation}$	Duration of the hydrogenation step under H_2	min or h
m	Mass used for ammonia-rate normalisation	g
m_{LiH}	Mass of LiH contained in the tested composite	g
2θ	XRD diffraction angle	degree
d	Lattice spacing measured from HRTEM or assigned from diffraction data	nm

Symbol	Description	Unit
BE	XPS binding energy	eV

List of Publications

- **Hangzuo Guo**, Alexander RP Harrison, Mingchen Gao, Xusheng Zhang, Qicheng Chen, Zhanfeng Cui, Binjian Nie. Chemical looping based Low-pressure ammonia synthesis, Chemical Engineering Journal, Volume 500, 2024, 157321 10.1016/j.cej.2024.157321.
- Haoliang Hong, **Hangzuo Guo**, Zhanfeng Cui, Anthony Ball, Binjian Nie. Structure modification of magnesium hydride for solid hydrogen storage, International Journal of Hydrogen Energy, Volume 78, 2024, Pages 793-804, 10.1016/j.ijhydene.2024.06.327.
- Xusheng Wang, Longfei Shao, Shouyi Hu, Zi Li, **Hangzuo Guo**, Jiaqi Zhang, Yingyan Zhao, Xi Lin, Binjian Nie, Zhigang Hu, Jianxin Zou. A techno-economic study of photovoltaic-solid oxide electrolysis cell coupled magnesium hydride-based hydrogen storage and transportation toward large-scale applications of green hydrogen, Energy & Environmental Science, Volume 17, 2024. Pages 8429-8456, ISSN 1754-5692, 10.1039/D4EE04224G.
- Xusheng Wang, Tao Cheng, Haoliang Hong, **Hangzuo Guo**, Binjian Nie, Zhigang Hu, Jianxin Zou, Challenges and opportunities in hydrogen storage and transportation: A comprehensive review, Renewable and Sustainable Energy Reviews, Volume 219, 2025, 115881, ISSN 1364-0321, 10.1016/j.rser.2025.115881.

1. Introduction

1.1 Background

1.1.1 Energy and climate challenges

The use of energy has supported economic growth and technological development, but the present energy system still relies heavily on fossil fuels [1]. More than 80% of the global energy supply comes from fossil sources, creating a linked problem of resource depletion and climate impact. At the current rate of use, fossil fuels are consumed on timescales far shorter than those required for their natural formation [2, 3]. More importantly, fossil-fuel combustion accounts for nearly three-quarters of global greenhouse gas (GHG) emissions, which are a major driver of climate change and associated extreme weather. Reducing this dependence requires energy technologies that can store, transport and convert renewable energy more effectively.

1.1.2 Hydrogen and hydrogen carriers

Hydrogen is widely discussed as a clean energy carrier because of its high gravimetric energy density (120 MJ kg^{-1}) and its ability to generate electricity without direct carbon emissions when used in fuel cells [4, 5]. However, its wider use is still limited by the way it is produced, stored and transported. Most of the hydrogen produced is still dependent on steam methane reforming (SMR), which leads to significant greenhouse gas emissions. Blue hydrogen is produced through SMR with carbon capture and

storage (CCS), while green hydrogen is produced through renewable-powered electrolysis; both routes face cost and scale-up challenges [6, 7].

Storage and transport are particularly difficult parts of the hydrogen supply chain. Although hydrogen has a high gravimetric energy density, its volumetric energy density under ambient conditions is very low. Practical storage normally requires either compression to high pressures, up to 700 bar, or liquefaction at -253 ℃. Both approaches add energy penalties, cost and safety concerns [8, 9]. These limitations make chemical hydrogen carriers attractive for long-duration storage and long-distance transport, especially for storing or transporting renewable energy over long distances.

1.1.3 Ammonia as a hydrogen carrier

Ammonia (NH_3) is one of the most promising chemical hydrogen carriers because it combines high hydrogen density with relatively practical storage conditions. Compared with representative hydrogen carriers, as summarised in **Table 1.1**, ammonia has a high volumetric hydrogen density and can be stored either by moderate pressurisation at room temperature or by cooling to -33 ℃ at ambient pressure [2, 10-14]. As a carbon-free compound, ammonia can be synthesised from nitrogen and hydrogen and later decomposed to release hydrogen, making it relevant to energy storage, transport and low-carbon fuel applications [15, 16].

Table 1.1. Characteristics of hydrogen carriers [2, 10-14].

Properties	Phase	Density (kg m^{-3})	Boiling point (°C)	Volumetric H_2 content (kg_{H2} m^{-3})	Volumetric energy density (MJ L^{-1})	Gravimetric H_2 content (wt.%)	Gravimetric energy density (MJ kg^{-1})
LH_2*	liquid	70.8	-253	71	8.5	100	120.2
CH_4	liquid	422	-161	105	22.2	25	50.5
CH_3OH	liquid	792	65	99	11.9	13	19.7
MCH*	liquid	770	101	47	5.7	6	7.3
NH_3	liquid	610	-33	121	12.7	18	18.6

**LH₂: liquid hydrogen; *MCH: methylcyclohexane.*

Ammonia also benefits from existing industrial infrastructure for production, storage and distribution [17]. This is important because any future energy carrier must be assessed not only by energy density, but also by its compatibility with existing transport, storage and handling systems. Ammonia is toxic at high concentrations and therefore requires proper safety controls. At the same time, it has practical safety features: its pungent odour allows leakage to be detected at low concentrations, and its flammability range in air is narrower than that of hydrogen. These features do not remove the hazards associated with ammonia, but they support its use as a chemical hydrogen carrier when appropriate engineering controls are applied [12, 15].

1.2 Ammonia synthesis pathways

1.2.1 Haber-Bosch process

Currently, global ammonia production exceeds 200 Mt per year, and approximately 96% is produced through the Haber-Bosch (HB) process [18]. In this process, nitrogen and hydrogen are converted to ammonia over promoted iron-based catalysts at elevated temperatures and high pressures, typically 450-600 °C and 100-250 bar [19]. The HB process is robust, mature and highly scalable, and it has supported global fertiliser production and chemical manufacturing for more than a century.

1.2.2 Limitations of the Haber-Bosch process

Despite its technical maturity, the HB process is not aligned with future low-carbon approaches and decentralised energy systems. First, the process is energy intensive

because nitrogen activation is difficult and because high pressure is required to achieve practical ammonia conversion and productivity. Ammonia production via conventional HB routes contributes approximately 1.2% of global anthropogenic CO2 emissions, mainly because hydrogen is still produced primarily from fossil fuels [19].

Second, the HB process is designed for large-scale continuous operation. Industrial plants commonly operate at capacities of thousands of tonnes per day, which helps reduce costs in centralised production but requires large capital investment, compression infrastructure, heat management, and gas recycling [18]. These features make the process less suitable for small-scale, modular or distributed ammonia production.

Third, conventional HB synthesis is difficult to couple directly with intermittent renewable electricity. Wind and solar power are variable and geographically distributed, whereas HB plants are designed to operate continuously under stable conditions. Even if renewable-based hydrogen is used, the synthesis loop still requires high pressure and hence all parts of the processes, feed gases purification, ammonia synthesis and separation, recycling of unreacted gases are all at the high pressure, that need to consume compression energy. Therefore, replacing fossil-derived hydrogen with green hydrogen does not by itself solve the pressure, scale and flexibility limitations of conventional ammonia synthesis.

1.2.3 Alternative ammonia synthesis pathways

Several alternative ammonia synthesis pathways have been investigated to address the pressure, scale and flexibility limitations of the Haber-Bosch process. These include thermocatalytic synthesis under milder conditions, electrocatalytic nitrogen reduction, photocatalytic nitrogen reduction, plasma-assisted ammonia synthesis and chemical looping ammonia synthesis. These approaches aim to reduce pressure requirements, use renewable energy more directly, or change the way nitrogen is activated.

However, each route still faces substantial technical barriers. Electrocatalytic systems are constrained by low Faradaic efficiency, slow ammonia production rates, and competing hydrogen evolution. Photocatalytic systems typically exhibit low reaction rates, limited nitrogen activation, and inefficient energy utilisation. Plasma-assisted processes can activate nitrogen at moderate bulk temperatures, yet they generally display low energy efficiency and require complex reactor configurations. Consequently, none of these emerging methods has been demonstrated at a practical scale with the combined activity, efficiency, stability, and scalability necessary for industrial ammonia production. The challenges extend beyond catalytic activity to include product separation, reactor design, cycling stability, and energy integration.

Chemical looping ammonia synthesis (CLAS) is particularly significant because it changes the reaction framework rather than only modifying the catalyst or the external energy input. In conventional thermocatalytic ammonia synthesis, N_2 activation, H_2 activation and NH_3 formation occur within the same reaction environment. In contrast,

CLAS separates nitrogen fixation from ammonia-forming hydrogenation. During the first step, N_2 is incorporated into a solid nitrogen carrier to form a nitrogen-containing intermediate. This intermediate is subsequently reacted with H_2 or H_2O to release NH_3 and return the carrier to a state capable of participating in the next cycle. By temporarily storing nitrogen in the solid phase, CLAS reduces the requirement for simultaneous N_2 and H_2 activation under high pressure and enables greater flexibility in carrier design, cyclic operation, and reactor configuration. As a result, CLAS presents a potential pathway for lower-pressure and modular ammonia production [20, 21].

The current state of the art includes two main classes of nitrogen carriers: metal nitride-based systems and alkali or alkaline-earth metal hydride/imide systems. Metal nitrides can store lattice nitrogen and release it as NH_3 during hydrogenation or hydrolysis. However, many of these systems are constrained by strong metal-nitrogen bonding, incomplete nitrogen release, difficult regeneration or high-temperature reduction requirements. Hydride/imide systems, such as LiH/Li_2NH-based carriers, facilitate more favourable nitrogen-hydrogen chemistry under comparatively mild conditions [22-25]. Transition-metal promotion has been shown to improve N_2 activation and ammonia production, while support materials can reduce agglomeration and enhance access to reactive domains. Despite these advances, most CLAS systems remain in the early stages of development and are limited by low overall productivity, incomplete carrier utilisation, uncertain long-term cycling stability, and complex gas-solid reaction

behaviour. Their performance remains inferior to that of established Haber-Bosch systems, although CLAS may provide benefits for lower-pressure, flexible, and decentralised operation.

A significant research gap remains in developing nitrogen carriers that combine effective nitrogen-fixation chemistry with an accessible and stable composite structure. In LiH-based CLAS, ammonia production depends not only on the ability of the transition metal to activate N_2, but also on maintaining effective contact among the promoter, LiH-derived nitrogen-storage domains and the gas phase during repeated nitridation and hydrogenation. The combined influence of promoter identity, promoter loading, support-assisted structural modification and fixed-bed operating conditions is not yet fully understood. This gap motivates the present investigation of transition-metal-promoted and supported LiH-based composites, with particular emphasis on Ni promotion, TiO_2-assisted structural modification and gas-solid accessibility in fixed-bed CLAS operation.

1.3 Aims and objectives

Conventional Haber-Bosch ammonia synthesis is difficult to adapt to low-pressure, modular and intermittently operated systems because it relies on high-pressure operation, continuous gas recycling and large-scale process integration. CLAS provides an alternative reaction framework by separating nitrogen fixation and ammonia-forming hydrogenation into sequential steps. This separation gives greater flexibility in

material and reactor design. However, the practical development of CLAS is still limited by the performance of solid nitrogen carriers, especially their nitrogen fixation activity, hydrogenation behaviour, cycling stability and gas-solid accessibility.

LiH-based hydride-imide systems are attractive model nitrogen carriers because LiH can react with nitrogen to form Li-N-H species such as Li_2NH, which can subsequently be hydrogenated to produce ammonia. However, pure LiH has limited reactivity under low-pressure conditions and can suffer from particle agglomeration and poor gas-solid contact. Transition metal promotion can improve nitrogen activation, while support-assisted structural modification may improve dispersion, particle morphology and gas contact with reactive LiH-containing regions. The central question addressed in this thesis is therefore how promoter identity, promoter loading, support addition and reactor operating parameters influence the effective utilisation of LiH-based nitrogen carriers in low-pressure CLAS. **Figure 1.1** summarises the material-design strategy and working hypothesis of this thesis. Ni is introduced to promote nitrogen activation in LiH-based composites, while TiO_2 is used as a structural support to modify the agglomeration state of Ni-LiH and improve gas contact with LiH-rich domains during alternating nitridation and hydrogenation [20, 21].

The aim of this thesis is to develop and evaluate transition-metal-promoted and supported LiH-based composites for chemical looping ammonia synthesis, with

emphasis on linking material structure, operating conditions and ammonia production performance.

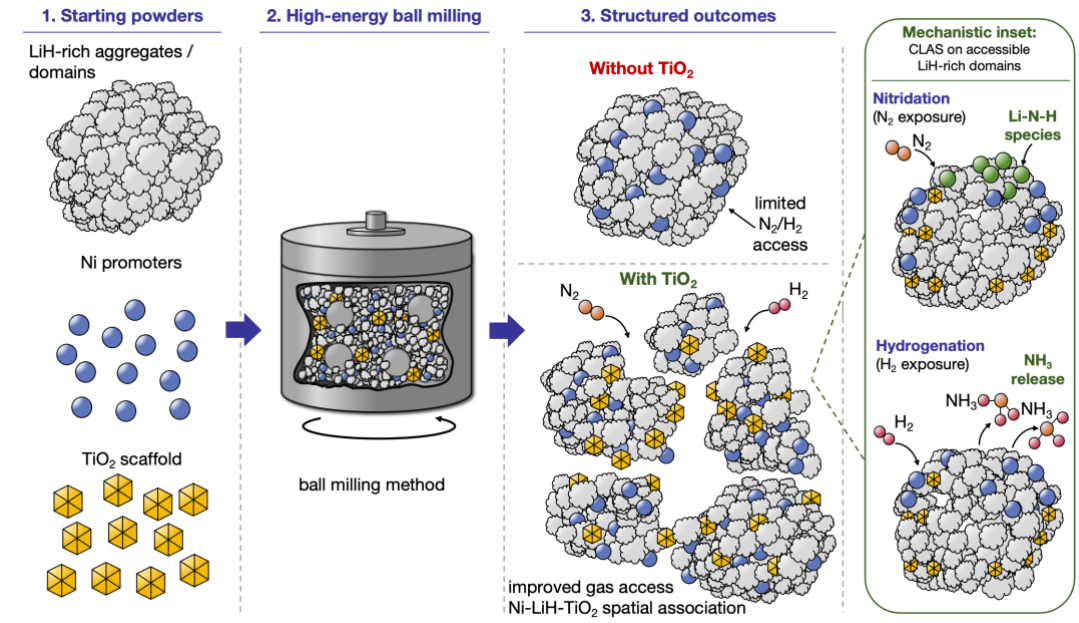


Figure 1.1. Schematic illustration of the preparation and structural concept of TiO_2-supported Ni-LiH composites [20, 21].

The objectives of this work are:

i. To design, construct and commission a lab-scale fixed-bed CLAS reactor for alternating N_2 and H_2 operation under controlled low-pressure conditions.

ii. To prepare transition-metal-promoted LiH composites and determine how promoter identity and promoter loading influence ammonia production.

iii. To investigate how reaction temperature, nitridation time, hydrogenation time, gas flow rate, cycling and fixed-bed loading affect the CLAS performance of Ni-LiH composites.

iv. To evaluate support-assisted structural modification of Ni-LiH composites using oxide, carbon-based and mineral supports, with particular focus on TiO_2-supported Ni-LiH.

v. To characterise the morphology, phase evolution, local elemental distribution and surface state of selected LiH-based composites using SEM, XRD, TEM-EDS, HRTEM and XPS.

The thesis is organised into 5 chapters. **Chapter 2** reviews ammonia synthesis routes, with emphasis on chemical looping systems and hydride-imide nitrogen carriers. **Chapter 3** describes material preparation, reactor testing and characterisation methods. **Chapter 4** presents the experimental data on performance, phase-evolution and structural results. **Chapter 5** summarises the main conclusions, limitations and suggests possible future research directions.

2. Literature Review

2.1 System-level constraints of conventional ammonia synthesis

The Haber-Bosch process remains the dominant industrial route for ammonia synthesis because it is reliable, mature and capable of very large-scale production. However its future role in low-carbon energy systems is limited not only by catalyst performance, but also by the linked requirements for hydrogen production, gas compression, ammonia separation, gas recycling and continuous operation. These factors become especially important when ammonia production is coupled to green hydrogen and variable renewable electricity. The following sections therefore consider why the conventional HB process is difficult to adapt to low-pressure, flexible and decentralised operation.

2.1.1 Energy and process coupling

From an energy perspective, ammonia synthesis is closely linked to hydrogen production. In conventional ammonia production, hydrogen is mainly produced from fossil-based routes such as steam methane reforming, which contributes substantially to both energy consumption and CO_2 emissions [18, 19]. In green ammonia production, this fossil-derived hydrogen is replaced with hydrogen produced by water electrolysis. This can reduce direct carbon emissions, but it also introduces a large electricity demand and makes the overall process strongly dependent on electrolyser efficiency, electricity cost and renewable power availability [18, 19, 26].

Table 2.1. Energy efficiency and consumption for ammonia and hydrogen production [19, 26].

Hydrogen energy carrier		Energy efficiency (LHV*) (%)	Energy efficiency (HHV*) (%)	Energy consumption (kJ mol_{H2}^{-1})						
				Total	Electrolysis	SMR	ASU	HB	CCS	Liquefaction
NH_3	Green NH_3	56.1	67.8	377	354	-	5.22	16.8	-	-
	Blue NH_3	66.2	80.0	323	-	289	5.22	16.8	12	-
	Grey NH_3	67.9	82.0	311	-	289	5.22	16.8	-	-
H_2	Green H_2	68.4	80.8	354	354	-	-	-	-	-
	Blue H_2	66.5	78.6	364	-	351	-	-	13	-
	Grey H_2	68.9	81.4	351	-	351	-	-	-	-
LH_2	Green LH_2	55.7	65.8	435	354	-	-	-	-	80.7
	Blue LH_2	54.1	63.9	448	-	351	-	-	16	80.7
	Grey LH_2	56.1	66.2	432	-	351	-	-	-	80.7

**LHV: lower heating value; *HHV: Higher heating value*

A system-level comparison is useful because the energy required for hydrogen production and that required for the ammonia synthesis loop are not equivalent. **Table 2.1** summarises representative energy efficiencies and energy consumption values for ammonia and hydrogen production routes [19, 26]. In this table, energy efficiency refers to the ratio between the useful chemical energy retained in the produced energy carrier and the total energy input required for production, expressed on either a lower heating value (LHV) or higher heating value (HHV) basis. These data indicate that the energy profile of green ammonia is dominated by renewable hydrogen production, which requires substantially more energy than the Haber-Bosch synthesis loop itself. It indicates that improvements in sustainable ammonia production must be considered at the level of the integrated process, including hydrogen supply, compression, synthesis, separation and recycling. In addition, the Haber-Bosch synthesis requires elevated pressure, heat management, ammonia separation and recycling of unreacted gases. These requirements add process complexity and limit operational flexibility. Future sustainable ammonia synthesis routes should therefore reduce pressure requirements, simplify gas recycling and operate more effectively with variable renewable energy inputs.

2.1.2 Scale and decentralisation constraints

The scale and operating mode of Haber-Bosch ammonia production create another limitation. Modern plants are usually designed for very large capacities, commonly

reaching 2000-3000 t day^{-1} or higher. This helps reduce production cost in conventional industrial supply chains, but it requires high capital investment, complex compression and recycling equipment, and long construction and commissioning periods [18, 19]. As a result, the Haber-Bosch process is most effective and economically favourable when operated continuously at large, centralised plants.

Table 2.2. Ammonia synthesis is transitioning towards sustainable production approaches [18, 19].

Stage	Process	Ammonia	TRL	Present NH_3 demonstrated scale (tons per day)
0^{th}	SMR-HB	Grey	9	>2000
1^{st}	SMR-HB + CCS	Blue	7-9	>2000
2^{nd}	Electrolysis + HB	Green	5-8	0.02-0.03
3^{rd}	Electrolysis + Sustainable ammonia synthesis	Green + Carbon-free	1-5	<0.001

While grey ammonia production routes are well supported by established infrastructure for hydrogen production, synthesis, storage and distribution, emerging sustainable routes remain at much smaller demonstration scales. This contrast between conventional, transitional and emerging ammonia production pathways is summarised in **Table 2.2** [18, 19]. The key implication is that sustainable ammonia production cannot be assessed only by theoretical energy efficiency or carbon intensity. Grey ammonia remains dominant because it is technologically mature and built into existing industrial infrastructure. Blue ammonia can reduce emissions by adding carbon capture to fossil-based production. Green ammonia based on electrolysis and Haber-Bosch

synthesis is more sustainable in principle, but it still relies on high-pressure synthesis and has so far been demonstrated at much smaller scales. More advanced carbon-free routes, including chemical looping and other emerging ammonia synthesis methods, are at lower technology readiness levels (TRL).

The mismatch between renewable energy supply and conventional ammonia production highlights the need for alternative routes. Wind and solar energy are variable and geographically dispersed, while conventional Haber-Bosch plants require stable conditions. Frequent changes in power supply demand additional hydrogen storage, electricity buffering, or flexible plant operation, which increases system complexity and cost [27, 28].

Therefore, decentralised ammonia production that operates under milder conditions, reduces reliance on high-pressure compression, and adapts to variable renewable energy input is needed.

2.2 Alternative ammonia synthesis pathways

To address the limitations of the Haber-Bosch process, several alternative ammonia synthesis pathways have been investigated. These include improved thermocatalytic synthesis, electrocatalytic nitrogen reduction, photocatalytic nitrogen reduction, plasma-assisted ammonia synthesis and chemical looping ammonia synthesis. These

routes aim to reduce the dependence on high pressure, improve compatibility with renewable energy, or introduce different mechanisms for nitrogen activation.

The main alternative routes differ not only in their operating conditions, but also in the way nitrogen is activated and the source from which hydrogen is supplied. **Table 2.3** compares these routes in terms of feedstock, pressure, temperature, energy input, maturity and principal technical challenges [21, 29-33].

This comparison highlights key trade-offs among maturity, operating severity, energy input, and scalability. Thermocatalytic synthesis is the most established method, but it faces equilibrium limitations and requires high-pressure operation. Electrocatalytic and photocatalytic routes enable direct use of renewable electricity or solar energy, though their ammonia production rates and long-term stability are limited. Plasma-assisted ammonia synthesis activates nitrogen under mild conditions, but energy efficiency and reactor scale-up remain significant challenges. Chemical looping ammonia synthesis is less mature, yet it stands out by separating nitrogen fixation from ammonia formation through a solid nitrogen carrier. This distinction makes CLAS particularly relevant to the present thesis.

Table 2.3. Comparison of sustainable ammonia synthesis routes [21, 29-33].

Parameters	**Thermocatalytic (Haber-Bosch)**	**Electrochemical**	**Photocatalytic**	**Plasma-assisted**	**Chemical Looping Process**
N_2 Source	ASU*	ASU*	ASU*	ASU*, plasma activation	ASU*
H_2 Source	SMR, electrolysis	Water electrolysis	Water	H_2 (plasma discharge)	H_2/H_2O (electrolysis)
Pressure (MPa)	10-25	Ambient	Ambient	Ambient	Ambient
Reaction Temp. (°C)	450-600	25-700	25-50	25-200	300-600
Active material	Fe-based (promoted)	Pd, Ru, Fe-based	Semiconductors, TiO_2	Plasma-enhanced, metallic catalysts	Metal nitrides/Metal imides
Energy Efficiency (%)	37-65	55-88.5	<5	10-20	32-61
Energy Input	Heat/Electricity	Electricity	Solar light	Electricity (plasma)	Heat/ Electricity
CO_2 emission	High (from SMR), significant emissions	None (renewable electricity)	None (renewable electricity)	Low to none (renewable electricity)	None (potentially renewable heat/electricity)
Rate-limiting step	N_2 dissociation to N atoms	N_2 hydrogenation to N_2H*	N_2 activation and hydrogenation	N_2 dissociation (plasma activated)	N_2 fixation into carriers
TRL	9	3-5	1-3	3-5	1-3
Advantages	Proven technology, high scalability	Direct renewable electricity integration	Sustainable solar utilisation, no emissions	Rapid kinetics, ambient conditions	Direct renewable electricity integration,

					modular, distributed potential
Challenges	High energy intensity, CO_2 emissions, large-scale dependency	Catalyst durability, selectivity, efficiency	Low catalytic efficiency, photonic utilisation	Energy efficiency, plasma instability	N_2 carrier reactivity, long term cycling stability, complex reactor management
Future research	CCS integration, catalyst optimisation	Improved electrocatalyst stability and scale-up methods	High efficiency photocatalysts, photoreactor design	Advanced plasma reactors, catalyst-plasma synergy	Stable N_2 carriers and reactor design, techno-economic assessments

**ASU: air separation unit.*

2.2.1 Thermocatalytic ammonia synthesis

Thermocatalytic ammonia synthesis is the most established route because it is based on the direct reaction between nitrogen and hydrogen. Industrial Haber-Bosch catalysts are mainly based on promoted iron catalytic systems, which have been developed and optimised for more than a century [34-36]. The overall reaction is shown in **Eq. 1**.

$$N_2 + 3H_2 \rightarrow 2NH_3 \ (\Delta H = -92.4\ kJ\ mol^{-1}) \qquad (1)$$

This reaction is reversible and exothermic. Increasing temperature improves reaction kinetics, but lower temperature favours ammonia formation at equilibrium. Industrial ammonia synthesis therefore normally uses high pressure to achieve practical ammonia conversion and productivity, and the typical single-pass conversion rate is about 10-15% [19, 36-38]. Unreacted nitrogen and hydrogen must then be separated from ammonia and recycled back to the reactor, which increases process complexity and energy use.

Ruthenium-based catalysts have been widely studied as alternatives to iron catalysts because they can show higher activity under milder conditions (280-400 ℃ & 50-100 bar) [39, 40]. Their performance can be improved using suitable supports and promoters, such as carbon materials, electrides and electron-rich oxides, which promote nitrogen activation [41, 42]. The studies show that catalyst design can reduce the severity of reaction conditions to some extent.

However, even highly active thermocatalysts do not alter the equilibrium limitation of the direct N_2/H_2 reaction. At low pressure, ammonia concentration remains low, which makes product separation difficult [43]. Integrated ammonia separation methods, such as absorption using metal halides or other solid absorbents, have therefore been proposed to improve single-pass conversion [44-46]. These approaches are promising, but they also add further complexity to reactor and separation design.

Thermocatalytic ammonia synthesis can therefore be improved through better catalysts and separation strategies, but it still follows the same direct reaction pathway as the Haber-Bosch process. Pressure, equilibrium and gas recycling remain difficult to avoid. A different reaction pathway is therefore required if ammonia synthesis is to become more suitable for low-pressure and flexible operation.

2.2.2 Electrocatalytic ammonia synthesis

Electrocatalytic ammonia synthesis uses electricity to drive nitrogen reduction under mild conditions. In principle, it can use renewable electricity to convert nitrogen and water into ammonia through proton-coupled electron transfer. This is attractive because it could avoid the separate production and compression of hydrogen used in conventional ammonia synthesis [47-50].

Many electrocatalysts have been investigated, including transition metals, transition metal nitrides, single-atom catalysts and doped carbon materials [47-54]. These materials aim to enhance nitrogen adsorption and activation while minimising the

competing hydrogen evolution reaction. Additional approaches, including defect engineering, interface design, and three-phase reaction interfaces, have also been investigated to improve nitrogen availability and ammonia selectivity [52-56].

However, key challenges remain low production rates, low selectivity, and limited long-term stability. In aqueous electrolytes, nitrogen reduction competes with hydrogen evolution, which consumes electrons and protons needed for ammonia formation [57]. Nitrogen's low solubility in water further restricts its supply to the catalyst surface. In many systems, ammonia is produced at very low concentrations, making reliable quantification difficult [57, 58].

Electrocatalytic ammonia synthesis is promising due to its direct use of electricity, but current systems are not yet viable for large-scale production. Achieving higher ammonia production rates, improved faradaic efficiency, reduced hydrogen evolution, and long-term operational stability are essential.

2.2.3 Photocatalytic ammonia synthesis

Photocatalytic ammonia synthesis seeks to use solar energy to reduce nitrogen under mild conditions. A semiconductor absorbs light, generating electron-hole pairs. The electrons drive nitrogen reduction, while the holes are consumed by water oxidation or another oxidation reaction [50, 59, 60]. The overall reaction is shown in **Eq. 2**, where water is used as the hydrogen source.

$$N_2 + 3H_2O \rightarrow 2NH_3 + 1.5O_2 \quad (2)$$

TiO_2 is widely studied for photocatalytic nitrogen fixation due to its chemical stability, low cost, and non-toxicity [61]. However, its wide band gap restricts light absorption to the ultraviolet region. To enhance its activity, researchers have applied doping, oxygen vacancy engineering, heterojunction construction, and co-catalyst modification [62-65]. These methods aim to improve light absorption, charge separation, and nitrogen activation.

Despite these advances, photocatalytic ammonia synthesis is still in its early stages. Weak nitrogen adsorption, rapid charge recombination, low solar-to-chemical conversion efficiency, and slow reaction kinetics limit performance [59, 60]. Low nitrogen solubility in water further constrains the process. Consequently, reported ammonia production rates remain insufficient for practical use.

In this thesis, photocatalytic ammonia synthesis is discussed within the broader context of mild-condition ammonia synthesis. TiO_2 is later used as a support for LiH-based composites, serving a structural rather than a photocatalytic role.

2.2.4 Plasma-assisted ammonia synthesis

Plasma-assisted ammonia synthesis uses energetic electrons, radicals, ions and excited species to activate nitrogen under mild bulk conditions [66, 67]. Non-thermal plasma is particularly interesting because the electrons can be highly energetic while the overall

gas temperature remains relatively low. This allows nitrogen activation without heating the whole reactor to the high temperatures used in conventional thermocatalysis [67-69].

Catalysts have been introduced into plasma systems to improve ammonia production. Metals and metal oxides, including Ru-, Co-, Ni-, Fe- and Mg-based catalysts, have been studied to promote hydrogenation and ammonia desorption [66, 69, 70]. Hybrid systems that combine plasma with thermal, electrochemical or photochemical effects have also been reported [69-71]. These studies show that plasma can generate reactive nitrogen species and provide alternative pathways for ammonia formation.

However, plasma-assisted ammonia synthesis faces significant challenges. Energy efficiency is often low because much of the electrical energy is consumed by gas excitation, heating, or side reactions instead of ammonia formation. Performance also depends on reactor geometry, discharge type, catalyst position, and plasma-catalyst interaction [66-69]. These factors complicate scale-up and optimisation.

Plasma-assisted systems demonstrate that nitrogen activation is possible under mild conditions, but practical application remains limited by energy efficiency and reactor complexity. Chemical looping ammonia synthesis addresses nitrogen activation differently by using a solid nitrogen carrier instead of plasma-generated excited species.

2.2.5 Summary of alternative routes and transition to chemical looping

The alternative routes discussed above demonstrate that ammonia can be produced under milder conditions than the conventional Haber-Bosch process. However, each method has specific limitations. Thermocatalytic systems are constrained by reaction equilibrium and separation issues. Electrocatalytic systems are limited by rate, selectivity, and stability. Photocatalytic systems have low light utilisation and low ammonia production rates. Plasma-assisted systems struggle with energy efficiency and reactor scale-up.

These limitations suggest that sustainable ammonia synthesis may require a different reaction design, rather than only improving a single catalyst surface. Chemical looping ammonia synthesis provides such a route by separating nitrogen fixation and hydrogenation into two steps. In CLAS, nitrogen is first fixed by a solid nitrogen carrier, and ammonia is then produced in a separate hydrogenation step [20, 36]. This separation can reduce direct competition between nitrogen and hydrogen on the same surface and provides more flexibility in material and reactor design.

For this reason, the following section focuses on chemical looping ammonia synthesis, with particular attention to nitrogen carrier materials, especially metal nitride and alkali/alkaline-earth metal imide systems. This discussion provides the basis for the experimental focus of this thesis on transition-metal-promoted and supported LiH-based nitrogen carriers.

2.3 Chemical looping ammonia synthesis

Building on the comparison above, this section focuses on chemical looping ammonia synthesis as a route that separates nitrogen fixation from ammonia formation through a solid nitrogen carrier.

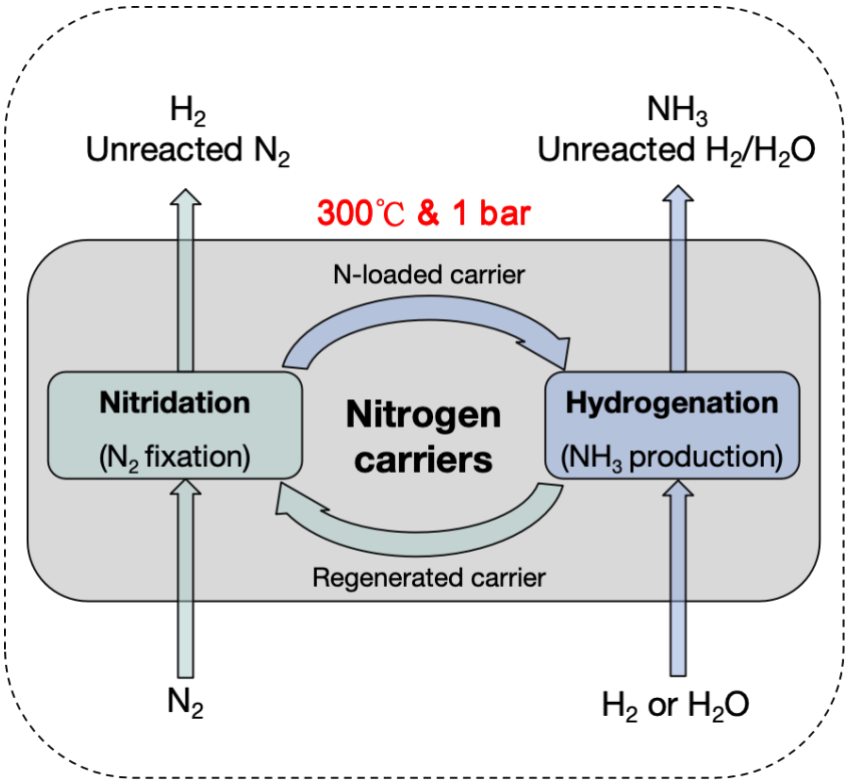


Figure 2.1. Conceptual process flow diagram for chemical looping ammonia synthesis.

In contrast to the direct reaction between N_2 and H_2 in the Haber-Bosch process, CLAS separates ammonia synthesis into two or more steps. In the first step, nitrogen is fixed by a solid nitrogen carrier to form a nitrogen-containing intermediate [72]. In the second step, the nitrogen-containing intermediate reacts with a hydrogen source, such as H_2 or H_2O, to produce ammonia and regenerate the original carrier [36]. **Figure 2.1** illustrates this process. Separating nitrogen fixation from ammonia formation can reduce

competition between nitrogen and hydrogen on the catalytic surface, addressing a key limitation of conventional thermocatalytic ammonia synthesis [73, 74].

The performance of CLAS depends largely on the nitrogen carrier. An effective carrier must fix nitrogen, release ammonia during hydrogenation or hydrolysis, and regenerate without significant degradation. CLAS pathways are classified by carrier type, including metal nitride-based and alkali or alkaline-earth metal imide-based pathways, as shown in **Figure 2.2** [75]. They can also be categorised by hydrogen source, such as H_2O-CLAS and H_2-CLAS. Each classification has specific requirements for temperature, regeneration, stability, and gas-solid reaction behaviour.

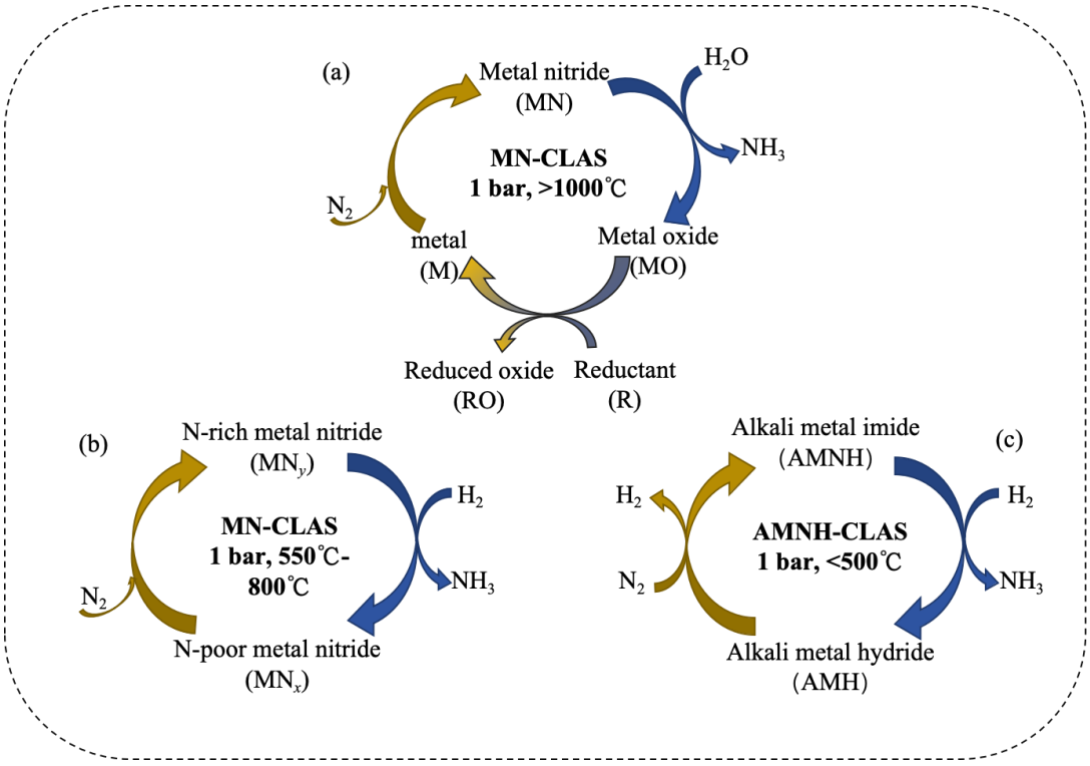


Figure 2.2. Schematics of CLAS mediated by a metal nitride using **(a)** H_2O, **(b)** H_2 as hydrogen source. **(c)** CLAS mediated by an alkali metal.

2.3.1 Metal nitride-based pathways

Metal nitrides are widely studied as nitrogen carriers because they store nitrogen in a solid lattice and release it as ammonia during hydrolysis or hydrogenation. In H_2O-CLAS, a metal or reduced metal species first reacts with nitrogen to form a metal nitride. The nitride then reacts with steam to generate ammonia and a metal oxide. To complete the cycle, the oxide must be reduced back to the initial metal or reduced phase. The general reactions are shown in **Eqs. 3-5**, where *M* denotes a metal species and *R* denotes a reducing agent [76].

Nitrogen Fixation:

$$a\,M + b/2\,N_2 = M_aN_b \quad (3)$$

Hydrogenation

$$M_aN_b + x\,H_2O = M_aO_x + b\,NH_3 + (2x - 3b)/2\,H_2 \quad (4)$$

Reduction

$$M_aO_x + x\,R = a\,M + x\,RO \quad (5)$$

The route is simple in concept, but regeneration is often difficult. For carriers such as AlN, Cr_2N, Mn_5N_2 and Mo_2N, the oxides formed after hydrolysis are highly stable and require very high temperatures for reduction, often above 1200 °C [77-79]. For example, the Al_2O_3/AlN cycle has been explored for solar thermochemical ammonia production, but the reduction of Al_2O_3 to AlN can require temperatures of approximately 1500-

2000 ℃ [80-84]. Such high temperatures increase energy demand and place strict requirements on reactor materials. They can also reduce the surface area and porosity of the solid carrier during repeated cycling, leading to a decline in long-term performance [79, 85].

To avoid the formation of stable oxides, H_2-CLAS pathways have been developed. In these systems, nitrogen carriers cycle between nitrogen-rich and nitrogen-deficient states without complete oxidation. The general reactions are shown in **Eqs. 6-7**, where *M* denotes a metal species.

Nitrogen Fixation & Reduction

$$M_aN_{b-x} + x/2\ N_2 \rightarrow M_aN_b \quad (6)$$

Hydrogenation

$$M_aN_b + 3x/2\ H_2 \rightarrow M_aN_{b-x} + x\ NH_3 \quad (7)$$

This pathway has been demonstrated in lattice-nitrogen-mediated ammonia synthesis over metal nitrides. Hargreaves and co-authors showed that Co_3Mo_3N can release part of its lattice nitrogen as ammonia under H_2 and can then be regenerated under N_2 [86-88]. Isotope exchange experiments indicated that lattice nitrogen participates directly in ammonia formation, demonstrating the feasibility of nitrogen transfer through a solid nitride. Later studies extended this concept to other nitrides, including Cu_3N, Ni_3N, Zn_3N_2 and Ta_3N_5 [89].

However, these nitride systems show clear trade-offs among activity, nitrogen capacity, and regenerability. Cu_3N and Ni_3N demonstrate high reactivity but are prone to structural instability and nitrogen loss during cycling. In contrast, Zn_3N2 and Ta_3N_5 offer greater stability, although their ammonia production rates are comparatively lower. Other nitrides, such as Fe_3N, Co_4N, and Re_3N, are capable of producing ammonia under hydrogenation conditions, yet they frequently display limited nitrogen fixation capacity or incomplete regeneration [90]. **Table 2.4** summarises reported nitrogen carrier systems [21]. As the reported rates are based on varying normalisation methods, reactor configurations, and operating conditions, these values should be interpreted as indicative performance ranges rather than as a direct ranking.

The main difficulty for metal nitride-based CLAS is therefore not simply the ability to form ammonia, but the need to balance nitrogen fixation, ammonia release and regeneration in the same material. Theoretical studies suggest that some carrier systems readily form stable nitrides but resist the release of lattice nitrogen during hydrogenation, whereas others release nitrogen more readily but are difficult to re-nitride under N_2. [91, 92]. Strong metal-nitrogen bonding can stabilise the nitride but reduce the availability of reactive nitrogen species, leading to relatively high operating temperatures [93, 94]. More ionic nitrides, such as Li_3N, Ba_3N_2 and Ca_3N_2, can be more reactive, but their high lattice stability can make regeneration difficult and often requires elevated temperatures [91, 95-97].

Overall, metal nitride-based pathways demonstrate that solid-state nitrogen transfer can be used for ammonia synthesis. However, they do not yet provide an ideal balance of nitrogen fixation, ammonia release, regeneration and cycling stability under mild conditions. This motivates the investigation of alternative nitrogen carrier systems with more favourable hydrogen and nitrogen chemistry.

2.3.2 Alkali and alkaline-earth metal imide-based pathway

Alkali and alkaline-earth metal hydride-imide systems provide an alternative CLAS pathway that can overcome some of the limitations of conventional metal nitrides. These systems are often referred to as alkali/alkaline-earth metal nitrogen-hydrogen (AMNH)-based CLAS. Their advantage arises from the coupled chemistry of hydrides, imides and ammonia, in which hydrogen can participate in different forms, including hydride H^-, molecular hydrogen H_2 and protonic hydrogen H^+ [98]. This hydrogen-based chemistry enables nitrogen fixation and ammonia release via hydride-imide transformations, rather than requiring complete oxidation and reduction of a metal carrier.

Early work on lithium nitride-imide systems showed that Li_3N and Li_2NH can reversibly interact with hydrogen under relatively mild conditions [22]. This finding established the foundation for Li-N-H chemistry, in which nitrogen species transition between nitride, imide, and amide-like environments. In AMNH-mediated chemical looping ammonia synthesis (CLAS), hydride species are directly involved in nitrogen

fixation and imide formation. During the hydrogenation step, the imide reacts with H2 to regenerate the hydride and release ammonia. The general reactions are shown in **Eqs. 8-9** [99]. Here, AMH_x refers to an alkali or alkaline-earth metal hydride, and $AM_{2/x}NH$ denotes the corresponding imide phase.

Nitrogen Fixation

$$4\ AMH_x + x\ N_2 \rightarrow 2x\ AM_{2/x}NH + x\ H_2 \quad (8)$$

Hydrogenation

$$x\ AM_{2/x}NH + 2x\ H_2 \rightarrow 2\ AMH_x + x\ NH_3 \quad (9)$$

Compared with H_2O-CLAS, this route avoids the need for high-temperature oxide reduction. Both nitridation and hydrogenation can become accessible at lower temperatures, typically between 300 and 500 ℃ [21]. Consequently, AMNH systems are particularly relevant for low-pressure ammonia synthesis.

LiH-based systems exemplify this pathway. During nitrogen fixation, LiH forms Li_2NH, which can be regenerated during hydrogenation, enabling repeated chemical looping operation [100]. Tagawa et al. demonstrated a LiH-based CLAS system in which nitrogen fixation to Li_2NH occurred at approximately 500 ℃, followed by ammonia production at around 350 ℃ [101]. However, the reaction rate decreased during cycling, primarily due to particle agglomeration that reduced gas-solid contact. Structural

modifications, such as the incorporation of Li_2O supports, have been shown to enhance stability and kinetics. Additional studies indicate that transition metals can lower the nitrogen fixation temperature and increase ammonia production [23, 24, 102].

BaH_2-based systems have demonstrated significant potential. Hydrogen vacancies in BaH_2 facilitate nitrogen fixation and the formation of BaNH [103, 104]. These systems can achieve high ammonia production rates and exhibit favourable cycling behaviour. However, not all AMNH systems are suitable. For example, alkali metal amides such as $NaNH_2$ and KNH_2 may promote hydrogenation but do not readily form stable imide intermediates, thereby limiting nitrogen fixation [105]. Similarly, CaNH and MgNH can be unstable under CLAS conditions and may convert to more stable nitride phases, which reduces ammonia production efficiency [106, 107]. Reported studies suggest that catalytic performance follows the approximate order $BaH_2 \geq LiH > KH > CaH_2 > NaH$, indicating the importance of hydrogen vacancy concentration, hydride reactivity, and electronic structure [108].

LiH is employed in this thesis as a model AMNH carrier. It is selected not for its superior activity, but for its experimental accessibility and well-defined hydride-imide chemistry, which are advantageous for studying CLAS. Its limitations, such as slow nitrogen fixation, particle agglomeration, and restricted gas-solid contact, also render it a valuable system for investigating transition metal promotion and support-assisted structural modification.

2.3.3 Catalytic and structural optimisation

Although AMNH-based CLAS exhibits more favourable reaction characteristics than many metal nitride systems, unmodified hydrides often show slow reaction kinetics and limited stability during cycling. In LiH-based systems, nitrogen fixation requires the formation of Li_2NH or related imide species, while the hydrogenation step must regenerate LiH and release NH_3. Both steps depend on reactive contact between the hydride phase, nitrogen-containing intermediates and gas-phase reactants. Pure LiH can therefore be limited by slow nitrogen activation, particle agglomeration and restricted gas access.

Transition metal promotion is an effective strategy for improving the reactivity of hydride-based nitrogen carriers. Metals such as Ni, Fe, Co, Zn and Pd can provide additional sites for nitrogen adsorption and activation, while maintaining contact with the hydride phase that participates in imide formation and hydrogen transfer. The comparison in **Table 2.4** shows that unmodified Li_2NH/LiH gives a reported NH_3 production rate of approximately 100 μmol g^{-1} h^{-1} at 350 °C, while Pd-Li_2NH/LiH reaches 700 μmol g^{-1} h^{-1} at 300 °C, Zn-Li_2NH/LiH reaches 956 μmol g^{-1} h^{-1} at 350 °C, and Ni-Li_2NH/LiH reaches 1533 μmol g^{-1} h^{-1} at 300 °C. These values indicate that the activity of LiH-based AMNH-CLAS can be substantially improved by suitable transition metal promotion.

Table 2.4. The operating conditions and NH_3 production rate of various N carriers [21].

System	N carriers	N carrier pairs	Condition			NH_3 production rate ($\mu mol\ g^{-1}\ h^{-1}$)	Ref.
			Regeneration	Nitridation	Denitridation		
Haber–Bosch process	Fe-based catalysts	Al_2O_3-Fe_3O_4		430 ℃ & 30 bar		11,900	[109]
		K-Al_2O_3-FeOOH		500 ℃ & 90 bar		32,850	[110]
	Ru-based catalysts	Ru-Pr_2O_3		310 ℃ & 10 bar		1000	[111]
		MgO-Cs-Ru		300 ℃ & 10 bar		600	[112]
H_2O-CLAS	Metal Nitride	AlN/Al_2O_3		1500~2000 ℃	1200 ℃	-	[113]
		ZrO_2-AlN/Al_2O_3		1000 ℃	1000 ℃	850	[114]
		NaOH-Mn_5N_2/MnO		1150 ℃	500 ℃	-	[115]
		$Cr/Cr_2N/Cr_2O_3$	500~1000 ℃	1200~1500 ℃	1000 ℃	124	[77, 116]
		$Mo/Mo_2N/MoO_2$	750~1200 ℃	750~850 ℃	500 ℃	1,200.6	[78]
		Mn/Mn_4N_2/MnO	1400 ℃	700 ℃	500 ℃	635.7	[77]
		Ca/Ca_3N_2-Ca_2N/CaO	2000 ℃	1200 ℃	200 ℃	-	[77]
		Zn/Zn_3N_2/ZnO	1000 ℃	1200 ℃	500 ℃	-	[77]
		e-Li/Li_3N/LiOH	450 ℃ & 3V	22~100 ℃	120 ℃	-	[117]
		l-TiN-Mg/Mg_3N_2/MgO*	550 ℃ & 30W cm^{-2}	550 ℃ & 30 W cm^{-2}	550 ℃ & 30 W cm^{-2}	1.67	[118]
H_2-CLAS		$MnN_{x-\delta}/MnN_x$		800 ℃	400 ℃	51.2	[119]
		Li-$MnN_{x-\delta}/MnN_x$		800 ℃	500 ℃	414.4	[119]

	Mo/Mo_2N		600 ℃	450 ℃	4,576	[93]
	Co_6Mo_6N/Co_3Mo_3N		700 ℃	500 ℃	98	[94]
	$Ni_2Mo_3N/Ni_2Mo_3N_{1-x}$		700 ℃	400 ℃	11	[94]
	$Mn_6N_{2.58}/Mn_4N$		700 ℃	550 ℃	61.5	[91]
	SrH_2/Sr_2N		700 ℃	550 ℃	87.6	[91]
	Ca_2NH/Ca_3N_2		700 ℃	550 ℃	120.9	[91, 120]
	Fe/Fe_3N		500 ℃	400 ℃	50	[90]
	Re/Re_3N		700 ℃	350 ℃	130	[90]
	Cu/Cu_3N		-	250 ℃	665	[89]
	Ni/Ni_3N		480 ℃	250 ℃	757.5	[89]
	Zn/Zn_3N_2		-	400 ℃	852	[89]
	Ta/Ta_3N_5		700 ℃	400 ℃	80	[89]
	$Re\text{-}Ta/Ta_{2.5}Re_{0.5}Ny$		-	500 ℃	23.1	[121]
	$Fe\text{-}Ta/Ta_{2.5}Fe_{0.5}Ny$		-	500 ℃	25.1	[121]
	$Co\text{-}Ta/Ta_{2.5}Co_{0.5}Ny$		-	500 ℃	250.8	[121]
	$Co\text{-}Zn/Co_3ZnN$		-	500 ℃	581.8	[122]
	$Ni\text{-}Zn/Ni_3ZnN$		-	500 ℃	576.8	[122]
	$Co\text{-}In/Co_3InN$		-	500 ℃	253.8	[122]
	$Ni\text{-}In/Ni_3InN$		-	500 ℃	467.3	[122]
	$Sn\text{-}Li/Li_3N/LiH$	500 ℃	500 ℃	240 ℃	120	[123]
Metal imides	Li_2NH/LiH		350 ℃	350 ℃	100	[124]

	Pd-Li_2NH/LiH	300 ℃	300 ℃	700	[124]
	Zn-Li_2NH/LiH	350 ℃	350 ℃	956	[125]
	Ni-Li_2NH/LiH	300 ℃	300 ℃	1,533	[23]
	BaNH/BaH_2	350 ℃	350 ℃	198	[23]
	Fe-BaNH/BaH_2	300 ℃	300 ℃	1,703	[23]
	Co-BaNH/BaH_2	300 ℃	300 ℃	1,866	[23]
	Ni-BaNH/BaH_2	300 ℃	300 ℃	3,125	[23]
	Ni-MgO-BaNH/BaH_2	250 ℃	250 ℃	1,530	[23]
	Ni-Al_2O_3-BaNH/BaH_2	250 ℃	250 ℃	2,770	[23]
	molten salt-Li_2NH/LiH	400 ℃	400 ℃	914	[126]
	e-molten salt-Li_2NH/LiH*	400 ℃ & 2V	400 ℃ & 2V	2,058	[126]
	p-$NaNH_2$/NaH*	300 ℃ & 12kV	25~250 ℃ & 12kV	550	[127]
	p-MgO-$NaNH_2$/NaH*	300 ℃ & 12kV	25~250 ℃ & 12kV	2,080	[127]
	p-MgO-KNH_2/KH*	-	25~250 ℃ & 12kV	842	[127]
	Cr-Li_2NH/LiH	300 ℃ & 10 bar	300 ℃ & 10 bar	3,600	[128]
	Mn-Li_2NH/LiH	300 ℃ & 10 bar	300 ℃ & 10 bar	3,100	[24, 128]
	Fe-Li_2NH/LiH	300 ℃ & 10 bar	300 ℃ & 10 bar	4,450	[24, 128]
	Co-Li_2NH/LiH	300 ℃ & 10 bar	300 ℃ & 10 bar	4,200	[24, 128]
Metal imides-nitrides	Mn_2N/Li_2NH-Mn_4N/LiH	200 ℃	300 ℃	1,576	[25]
	Mn_2N/BaNH-Mn_4N/BaH_2	225 ℃	300 ℃	3,142	[25]

**e: electro-driven; l: light-driven; p: plasma-driven*

Although the reported NH_3 production rates are not directly comparable because different studies use different reactor configurations, operating conditions and normalisation methods, **Table 2.4** shows that conventional Fe-based Haber-Bosch catalysts achieve substantially higher production rates under elevated pressures. However, when the direct N2/H2 synthesis pressure is reduced, the equilibrium NH_3 concentration and practical productivity decrease, even when more active catalysts are used. CLAS does not yet match the absolute productivity of mature high-pressure Haber-Bosch synthesis, but its relative advantage becomes more relevant under low-pressure conditions because nitrogen fixation and ammonia-forming hydrogenation are separated into sequential steps. CLAS should therefore be considered as a potential complementary route for low-pressure, modular and flexible ammonia production, rather than as a direct replacement for large-scale high-pressure Haber-Bosch plants.

Ni is particularly relevant to the present work. In LiH-based systems, Ni promotion has been reported to give higher ammonia production than unmodified LiH and several other promoted LiH systems under low-pressure conditions [101-103]. In BaH_2-based systems, Ni-BaNH/BaH_2 has also shown high activity, with reported NH_3 production rates of approximately 3125 μmol g^{-1} h^{-1} at 300 °C [103]. These results suggest that Ni can play an important role in enhancing nitrogen activation and improving hydride-imide cycling.

However, the performance of transition-metal-promoted hydrides is not determined only by the identity or amount of the metal promoter. The physical contact between the metal and hydride phases, the distribution of active components, particle size, agglomeration and gas-solid accessibility all affect the number of active interfaces available during cycling. Mechanical mixing or ball milling can improve contact between LiH and transition metals, but the resulting composite may still contain non-uniform particle distributions or local agglomeration. These structural factors become especially important when the metal loading is increased, because a higher metal fraction may enhance catalytic activity but also reduce the relative amount of active hydride and change the packing structure of the solid bed.

Structural optimisation is therefore a necessary extension of catalytic promotion. Conductive supports, oxide supports, and porous scaffolds can help disperse active phases, reduce particle agglomeration and maintain gas transport pathways within the composite. Reported supported systems provide evidence for this approach. For example, supported Ni-Al_2O_3-BaNH/BaH_2 can reach approximately 2770 μmol g^{-1} h^{-1} at 250 °C, showing that support-assisted dispersion can maintain high activity at lower temperature [23]. Other supported or externally assisted AMNH systems, such as molten salt, electro-driven, and plasma-assisted routes, further demonstrate that the local environment surrounding the nitrogen carrier strongly influences CLAS performance.

These studies show that AMNH-CLAS performance is controlled by carrier chemistry, composite structure and reactor-level gas-solid transport. Transition metals can promote nitrogen activation, while supports can influence dispersion, agglomeration and metal-hydride interfacial contact. However, in fixed-bed CLAS tests, the measured ammonia production also depends on how effectively N_2 and H_2 are distributed through the powder bed and how efficiently NH_3 is removed from the reactor. These bulk transport effects become more important when hydride-containing powders agglomerate or when material loading is increased. Therefore, the central question is not only how the promoter, hydride and support should be arranged, but also whether the resulting bed structure maintains effective gas-solid contact during repeated cycling.

This reasoning defines the material focus of the thesis. LiH is used as the model AMNH carrier, transition metals are introduced to improve nitrogen activation, and support materials are investigated as structural modifiers. The aim is to determine how promoter identity, promoter loading, and support-assisted structural modification affect ammonia production in a laboratory-scale CLAS reactor.

2.3.4 Reactor and system-level considerations

Although the primary focus of this thesis is on nitrogen carrier materials, reactor operation also significantly influences measured CLAS performance. Fixed-bed reactors are advantageous for laboratory comparisons because they enable controlled nitridation and hydrogenation steps. However, the ammonia production rate in a fixed

bed depends not only on intrinsic material reactivity, but also on heat transfer, gas flow, mass-transfer limitations, bed packing and gas-solid contact. These factors are especially important for hydride-based materials, which can agglomerate or restructure during cycling. In fixed-bed CLAS reactors, mass-transfer limitations may arise from non-uniform gas distribution, dense powder packing, limited penetration of N_2 and H_2 into the bed, and delayed removal of NH_3 from the reactor and downstream line. Therefore, flow rate, pressure, residence time, bed geometry and sample loading must be considered when comparing nitrogen-carrier performance.

Several approaches have been explored to improve energy delivery and reaction control in CLAS. External-field-assisted methods, including electro-driven [95, 126], light-driven [77, 78, 118], and plasma-assisted [37, 127], have been reported as ways to enhance nitrogen activation or improve reaction kinetics. For example, electro-driven Li-mediated CLAS using molten salt cells can facilitate both nitrogen fixation and hydrogenation, with reported ammonia production rates of 2058 μmol g^{-1} h^{-1} [126]. Light-assisted systems using photothermal effects from plasmonic materials such as TiN, as well as plasma-assisted activation strategies, have also been investigated [118, 129]. These studies indicate that the way energy is supplied to the nitrogen carrier can strongly influence CLAS performance. However, many of these systems remain at an early stage and introduce additional complexity beyond conventional fixed-bed testing.

Ammonia separation is another important issue for future process development. In conventional ammonia synthesis, integrated absorption strategies have been used to remove ammonia from the reaction environment and improve single-pass conversion. For example, Smith et al. demonstrated an integrated catalyst-absorbent system using $Ru/Cs/CeO_2$ catalysts and $MnCl_2$-based absorbents, enabling ammonia production beyond equilibrium-limited single-pass conversion [45]. Although this example is not directly the focus of the present experimental work, it highlights the broader importance of coupling reaction and separation in low-pressure ammonia synthesis.

At the system level, CLAS has been proposed as a possible route for lower-pressure and more flexible ammonia production. Its potential advantage lies in separating nitrogen fixation from ammonia formation, which may reduce the need for direct high-pressure N_2/H_2 synthesis. **Table 2.5** places this potential in context by comparing representative energy costs and technical parameters for conventional Haber-Bosch, green Haber-Bosch and CLAS routes [130]. The comparison in **Table 2.5** represents a projected system-level scenario for CLAS rather than a mature industrial benchmark. CLAS remains at a lower technology readiness level than conventional Haber-Bosch synthesis, and its projected advantages depend on assumptions about nitrogen carrier lifetime, reactor design, heat integration, electricity source and scale [121, 122]. The role of this comparison in the present thesis is therefore to motivate material-level investigation: any future system-level benefit of CLAS requires nitrogen carriers with

sufficient activity, stability and gas-solid accessibility under repeated nitridation-hydrogenation cycles.

Overall, the literature indicates that CLAS is a promising low-pressure route for ammonia synthesis, but its further development is still limited by nitrogen carrier stability, reaction kinetics and gas-solid accessibility. These limitations are particularly relevant for LiH-based AMNH systems. Transition metal promotion can improve reactivity, but it does not by itself guarantee stable and accessible reactive interfaces during cycling. This thesis therefore investigates ball-milled transition-metal-promoted and supported LiH-based composites to determine how promoter identity, promoter loading and support structure affect ammonia production under low-pressure CLAS conditions.

Table 2.5. Comparative energy costs and technical parameters for ammonia production routes [130].

Route	**Hydrogen Source**	**Energy Source**	**Process Type**	**Energy Cost (£ t_{NH3}^{-1})**	**Energy consumption (GJ t_{NH3}^{-1})**	**CO_2 Emissions (kg_{CO2} kg_{NH3}^{-1})**	**Efficiency (%)**
Conventional HB (Coke, Coal)	Coke, Coal, Heavy Fuel Oil	Fossil Fuels (Coal, Oil)	Gasification	£205	56~64	5.32-6.18	65
Conventional HB (Natural Gas)	Natural Gas, Water	Fossil Fuels (Natural Gas)	Steam Reforming	£160	28~37	1.6~1.8	70
Liquid H_2O Electrolysis / Air Separation / HB	Water	Renewable (Electricity)	Liquid H_2O Electrolysis	£158	27~36	~0.5	54
Steam Solid Oxide Electrolysis / Air Separation /HB	Water	Renewable (Electricity)	Solid Oxide Electrolysis	£126	20~27	~0.5	61
CLAS	Water	Renewable (Electricity)	Chemical looping ammonia synthesis	£122	15~22	0.01~0.1	70

3. Methodology

This chapter describes the materials, sample preparation procedures, characterisation methods and reactor testing protocols used in this study. Based on the literature review in **Chapter 2**, lithium hydride (LiH) was selected as the model hydride-imide nitrogen carrier because it has been widely studied in alkali/alkaline-earth metal nitrogen-hydrogen-mediated chemical looping ammonia synthesis (AMNH-CLAS) and allows comparison with reported LiH-Li_2NH systems.

The experimental work was designed to investigate how transition metal promoters, promoter loading and support-assisted structural modification affect the ammonia production performance of LiH-based materials under low-pressure CLAS conditions. Two categories of materials were prepared: transition-metal-promoted LiH composites and supported transition-metal-promoted LiH composites. All LiH-based composites were prepared by mechanical mixing and ball milling under an inert atmosphere. The prepared samples were then characterised to examine morphology, elemental distribution, crystalline phase composition and near-surface chemistry, and were evaluated in a lab-scale fixed-bed CLAS reactor.

In contrast to previous CLAS studies that primarily examined individual nitrogen-carrier compositions or specific reaction steps, this study employs a unified experimental framework to simultaneously investigate material composition, composite structure, and fixed-bed operating behaviour. Initially, Ni-, Co-, Mn-, and

Fe-promoted LiH composites were synthesised and evaluated under identical low-pressure CLAS conditions, followed by systematic optimisation of promoter loading. Subsequently, oxide, carbon-based, and mineral supports were screened within the Ni-LiH system, and the effect of TiO_2 loading was examined in detail. Performance results were then correlated with morphology, crystalline phase evolution, local elemental distribution, and near-surface composition by series characterisation. Finally, temperature, reaction time, gas flow rate, cycling, and fixed-bed loading were assessed to differentiate material-composition effects from gas-solid accessibility and reactor-bed utilisation. The primary contribution of this study is the integrated investigation of nitrogen-carrier chemistry, support-assisted structural modification, and fixed-bed operating behaviour within a common experimental platform.

3.1 Materials

Table 3.1 summarises the main raw materials used in this study. Lithium hydride (LiH, 95%, powder, ~30 mesh, Sigma-Aldrich) was used as the primary nitrogen carrier. Transition metal promoters, including nickel (Ni, 99.8%, powder, 3-7 μm, Sigma-Aldrich), iron (Fe, ≥99%, powder, 6-8 μm, Sigma-Aldrich), manganese (Mn, 99.9%, ~ 50 μm particle size, Sigma-Aldrich), and cobalt (Co, 99.9%, ~ 2 μm particle size, Sigma-Aldrich), were used as promoters to investigate the effect of metal identity and loading on LiH-based CLAS performance.

Table 3.1. Materials.

Materials	Purity	Key properties	Supplier
Lithium hydride (LiH)	95%	~30 mesh particle size	Sigma-Aldrich
Nickel powder (Ni)	99 %	3-7 μm particle size	Sigma-Aldrich
Iron powder (Fe)	≥99%	6-8 μm particle size	Sigma-Aldrich
Manganese powder (Mn)	99.9%	~50 μm particle size	Sigma-Aldrich
Cobalt powder (Co)	99.9%	~2 μm particle size	Sigma-Aldrich
Titanium dioxide (TiO_2)	≥99.9%	Rutile phase, <5 μm	Sigma-Aldrich
Fumed silica (SiO_2)	~99%	0.2-0.3 μm aggregate size	Sigma-Aldrich
Graphene nanoplatelets (GNP)	~99%	Surface area ~750 m^2 g^{-1}	Sigma-Aldrich
Expanded graphite (EG)	>99%	Expansion ratio 270-325	Sigma-Aldrich
Diatomaceous earth (DE)	-	Porous structure	Sigma-Aldrich

A series of support materials was also selected to investigate the influence of structural modification on composite behaviour. Titanium dioxide (TiO_2, ≥99.9%, rutile, <5 μm, Sigma-Aldrich) and fumed silica (SiO_2, aggregate size 0.2-0.3 μm, Sigma-Aldrich) were used as oxide supports. Expanded graphite (EG, expansion ratio 270-325, Sigma-Aldrich) and graphene nanoplatelets (GNP, surface area ~750 m^2 g^{-1}, particle size <2 μm, Sigma-Aldrich) were selected as carbon-based supports because of their high specific surface area and potential to improve heat and mass transport within the solid bed. Diatomaceous earth (DE, powder, Sigma-Aldrich) was included as a porous mineral support to assess the effect of a low-cost scaffold on gas-solid accessibility.

All materials were used as received without further purification. Because the hydride-containing materials are highly sensitive to oxygen and moisture, all material handling, weighing, mixing and storage steps involving LiH-based samples were carried out

under an inert atmosphere in a glove box. Prepared samples were stored in sealed containers before characterisation and reactor testing.

3.2 Material preparation

All LiH-based composites were prepared by solid-state mixing and ball milling under an inert atmosphere. LiH-containing powders were weighed, manually pre-mixed and sealed in the milling container inside an Ar-filled glove box, before the sealed container was transferred to the planetary ball mill. This preparation route was selected because it enables close contact between LiH, transition metal promoters and support particles, while avoiding solvent exposure during sample handling. Two categories of materials were prepared in this work: TM-promoted LiH composites and supported TM-promoted LiH composites. Representative photographs of the preparation procedure, equipment and samples are shown in **Figure 3.1**.

3.2.1 Preparation of TM-promoted LiH composites

TM-promoted LiH composites were prepared by mechanically mixing LiH with transition metal powders, followed by high-energy ball milling. Ni, Fe, Mn and Co were selected as transition metal promoters. For each sample, LiH and the selected transition metal were weighed in an argon-filled glove box according to the desired composition. The unsupported composites were denoted as X%TM-LiH, where X represents the weight percentage of the transition metal in the sample.

After weighing, the powders were manually pre-homogenised inside the Ar-filled glovebox using an agate mortar and pestle for 5 min. The mixture was then sieved through a 0.125 mm mesh sieve. This pre-homogenisation and sieving procedure was repeated three times before the powder was loaded into the milling vessel. The premixed material was then loaded into a zirconia container together with zirconia milling balls, with a total ball mass of approximately 400 g, corresponding to a ball-to-powder mass ratio of approximately 50:1. The zirconia container was subsequently placed in a sealed steel milling vessel and transferred to a planetary ball mill (PULVERISETTE 6), as illustrated in **Figure 3.1a-d**.

A two-stage milling procedure was implemented. Initially, samples were milled at 200 rpm for 2 hours to promote uniform mixing and reduce compositional heterogeneity. Subsequently, high-energy milling at 300 rpm for 6 hours was conducted to enhance particle refinement and interfacial contact between LiH and the transition metal phase. To minimise overheating during milling, the process was operated intermittently using cycles of 10 min milling followed by 5 min rest. After milling, the samples were returned to the glove box, collected and stored in sealed containers prior to characterisation and reactor testing. Representative pure LiH and ball-milled 50 wt.% Ni-LiH samples are shown in **Figure 3.1e** and **Figure 3.1f**, respectively.

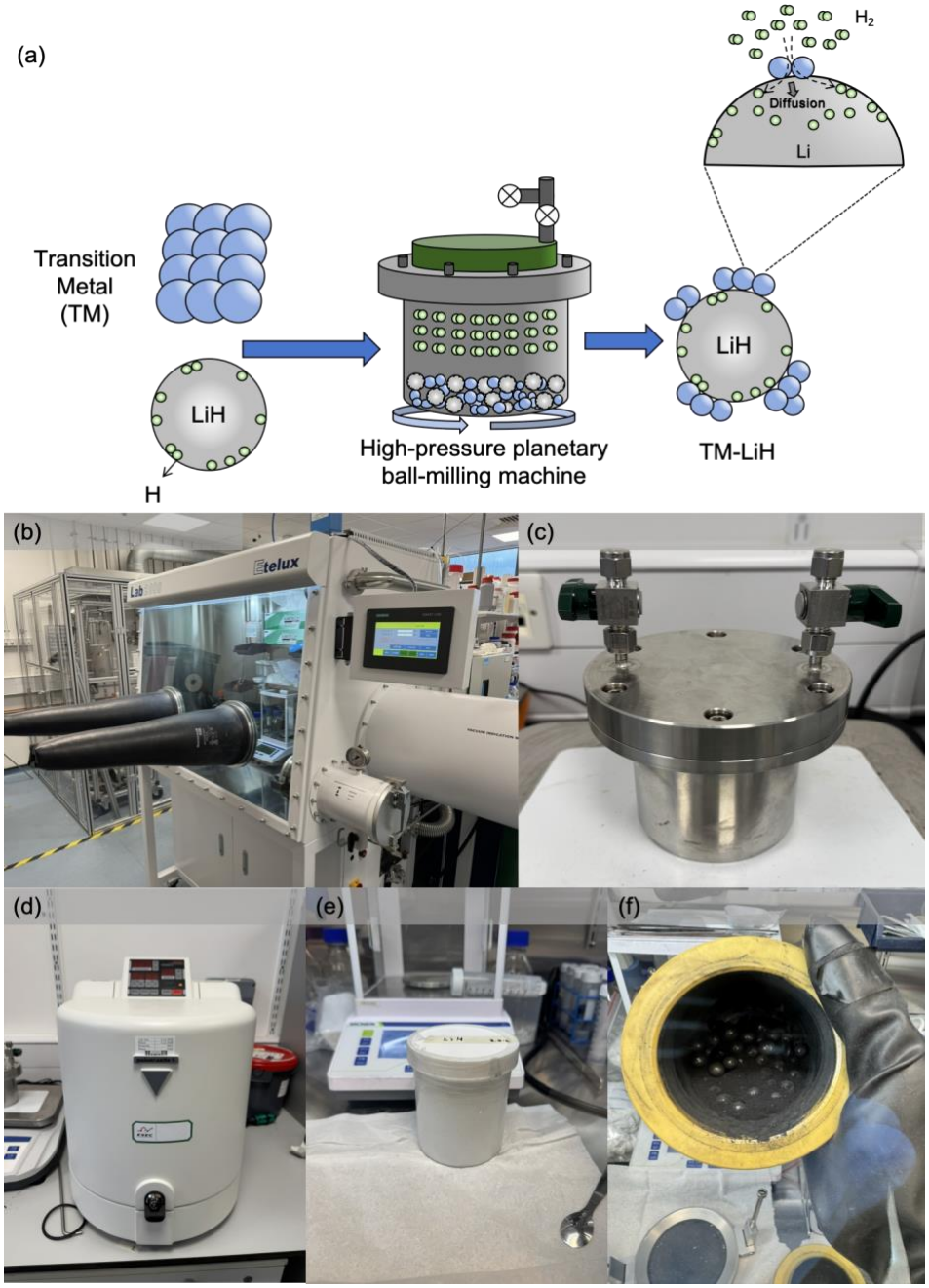


Figure 3.1. Preparation of ball-milled LiH-based composites and representative photographs of the sample handling and milling equipment.

(a) schematic illustration of the ball-milling process used to prepare TM-LiH composites; **(b)** Fe-LiH powder loaded in a zirconia container inside the glove box; **(c)** sealed steel vessel used for high-energy ball milling; **(d)** planetary ball mill; **(e)** pure LiH handled and stored inside the glove box; **(f)** ball-milled 50 wt.% Ni-LiH composite.

3.2.2 Preparation of supported LiH-based composites

Supported LiH-based composites were prepared to investigate the combined effects of transition metal promotion and structural modification by support materials. In this part of the study, support materials including TiO_2, SiO_2, expanded graphite, graphene nanoplatelets and diatomaceous earth were introduced into the LiH-based system.

For supported samples denoted as X wt.% Support-Y wt.% TM-LiH, X represents the support fraction in the total composite, while Y represents the transition-metal fraction within the TM-LiH active component. For example, 10 wt.% TiO_2-50 wt.% Ni-LiH refers to a composite containing 10 wt.% TiO_2 support and 90 wt.% of a Ni-LiH active fraction with a Ni: LiH mass ratio of 50:50.

The supported composites were prepared using the same solid-state route as that used for the unsupported materials. LiH, the selected transition metal powder and the support material were weighed in the glove box according to the target composition. Unless otherwise stated, Ni was used as the representative transition metal promoter for the supported systems. After weighing, the powders were manually pre-homogenised using the same grinding-sieving procedure described in **Section 3.2.1** and then loaded into a zirconia container with zirconia milling balls. The container was placed in a sealed steel milling vessel and milled under the same conditions described in **Section 3.2.1**.

Following ball milling, the supported composites were collected in the glove box and stored in airtight containers before further analysis. This preparation strategy provided

a consistent basis for comparing the effects of transition metal loading, support type and support loading on the ammonia synthesis performance of LiH-based materials under low-pressure CLAS conditions.

3.3 Material characterisation

Material characterisation was conducted to examine four principal aspects of the prepared LiH-based composites: particle morphology and agglomeration, elemental distribution, crystalline phase composition and near-surface chemical composition.

Scanning electron microscopy (SEM) was used to examine particle morphology and agglomeration; energy-dispersive X-ray spectroscopy (EDS) and transmission electron microscopy (TEM)-EDS were used to assess the qualitative spatial distribution of selected elements; X-ray diffraction (XRD) was used to identify crystalline phases and monitor phase evolution during nitridation; and X-ray photoelectron spectroscopy (XPS) was used to examine the near-surface elemental and chemical-state composition of selected samples.

Since LiH and Li-N-H species readily react with oxygen and moisture through oxidation and hydrolysis, air exposure was minimised during sample recovery, storage and transfer. Samples collected after CLAS testing were cooled under Ar before disconnection, recovered rapidly, and stored in sealed containers before characterisation. For XRD analysis, powders were loaded inside the glove box into an

air-sensitive XRD sample holder equipped with an X-ray-transparent dome cap and an O-ring seal, which limited exposure to air during transfer and measurement. For SEM, TEM and XPS analysis, fully air-free transfer was not available because the samples had to be mounted onto SEM stubs, TEM grids or XPS sample holders before insertion into the instrument chamber or load-lock. In these cases, the sealed containers were opened immediately before mounting, and the mounted samples were transferred into the instrument as quickly as possible. The typical exposure to laboratory air during mounting and transfer was kept below approximately 30 s at room temperature and approximately 40% relative humidity. This short exposure may affect the outermost surface chemistry of LiH-containing particles, especially O-, OH- or carbonate-related surface species, and was therefore considered when interpreting EDS and XPS results. Phase identification of LiH, Li_2NH and Li_3N was based primarily on XRD rather than surface-sensitive measurements.

3.3.1 Scanning electron microscopy and energy-dispersive X-ray spectroscopy

SEM was used to examine the particle morphology, particle-size distribution and agglomeration state of the prepared LiH-based composites. In this study, these features were used to assess how transition-metal addition and TiO_2 support addition modified the physical structure of the powders and the potential accessibility of LiH-containing regions to the reacting gases. For SEM analysis, a small amount of powder sample was

mounted onto conductive carbon tape attached to an SEM stub. The carbon tape was used to immobilise the powder and improve electrical contact, but it did not provide an air-tight seal. Therefore, brief air exposure during sample mounting and transfer to the SEM chamber could not be fully avoided. This exposure was minimised by preparing and transferring the samples as quickly as possible. As a result, SEM analysis was used mainly to compare morphology and agglomeration behaviour, rather than to assign air-sensitive LiH or Li-N-H phases.

EDS mapping was used to examine the qualitative spatial distribution of Ni, Ti, O and N within selected composite regions. The measurements were used to assess whether promoter-rich, support-rich and N-containing regions were locally distributed within the same particles or agglomerates. Particular attention was given to the distribution of Ni and Ti in supported TiO_2-Ni-LiH samples. SEM and EDS measurements were performed using a Zeiss scanning electron microscope. The accelerating voltage was typically 10-15 kV, depending on the sample and imaging mode. EDS maps and spectra were collected for selected elements, including Ni, Ti, O and N where applicable. EDS was used mainly as a qualitative elemental mapping method. Li and H could not be reliably detected by conventional EDS, and N signals were interpreted qualitatively because they can be affected by background, surface condition and sample geometry. Therefore, Li-N-H phase identification was based primarily on XRD, while SEM-EDS

was used to support discussion of particle morphology and qualitative elemental distribution.

3.3.2 X-ray diffraction

XRD was used as the primary technique for identifying crystalline phases and evaluating crystalline phase evolution during nitridation. In the context of this study, the formation of Li_2NH and Li_3N following N_2 exposure provided the principal structural evidence that nitrogen had been incorporated into the LiH-based carrier. Changes in the relative crystalline phase fractions were used to assess the extent and progression of crystalline nitridation under different N_2 exposure times. XRD was also used to identify residual LiH, metallic Ni and rutile TiO_2 in the supported composites.

Powder samples were collected before and after selected reaction steps. For nitridation studies, samples were collected after different N_2 exposure times to follow phase evolution during nitrogen fixation. Since LiH and Li-N-H species are sensitive to air and moisture, powders were loaded into an air-sensitive XRD sample holder inside the glove box. The holder was equipped with an X-ray-transparent dome cap and an O-ring seal to limit air exposure during transfer and measurement. The holder reduced contact with ambient oxygen and moisture, although it was not treated as a perfect air-free system. Samples were measured as soon as possible after loading.

XRD measurements were performed using Cu Kα radiation with a wavelength of 1.54060 Å. Diffraction patterns were collected over a 2θ range of 10-80°, with a step size of 0.02° and a counting time of 1 s per step. Each scan took approximately 1.25 h. Phase identification was carried out by comparison with reference patterns for LiH, Li_2NH, $LiNH_2$, Li_3N, Ni and rutile TiO_2 where applicable. For selected samples with sufficient signal quality, semi-quantitative crystalline phase fractions were estimated by Rietveld refinement using Profex with the BGMN backend. Because Li-containing hydride, imide and amide phases are air- and moisture-sensitive, and because poorly crystalline or amorphous species may not be clearly detected by XRD, the diffraction results were interpreted together with ammonia quantification and microscopy-based characterisation in **Chapter 4**. For selected reflections with sufficient peak quality, apparent coherent domain sizes were estimated using peak broadening analysis. These values were used only for comparative discussion because the estimates may be affected by instrumental broadening, microstrain, preferred orientation and overlapping reflections.

3.3.3 Transmission electron microscopy and TEM-EDS

TEM and HAADF-STEM were used to examine the local nanoscale morphology and internal domain structure of selected TiO_2-Ni-LiH composites. TEM-EDS was used to determine the qualitative local distribution of Ni, Ti, O and N, and to assess the spatial association between promoter-rich, support-rich and N-containing regions within

individual nitrided particles. HRTEM and FFT analysis were used to measure selected lattice-fringe spacings and provide supplementary local evidence for TiO_2- and Li-N-related crystalline domains. TEM measurements were performed using a Thermo Scientific Talos F200X G2 S/TEM. Dry powder samples were directly loaded onto lacey carbon film TEM grids supported on 300 mesh Cu or Ni grids. Dry powder loading was used to avoid solvent exposure during sample preparation.

The sealed sample container was opened immediately before grid loading. A small amount of powder was placed on the TEM grid, and the grid was then loaded into a standard TEM sample holder as quickly as possible before insertion into the TEM column. The typical air exposure during grid loading and transfer was kept below approximately 30 s at room temperature and approximately 40% relative humidity. A dedicated air-free or vacuum-transfer TEM holder was not used in this work. Therefore, TEM results were used mainly to examine local morphology, spatial association of Ni-, Ti/O- and N-containing regions, and selected lattice fringes, rather than to provide standalone identification of air-sensitive LiH or Li-N-H phases.

High-angle annular dark-field scanning transmission electron microscopy (HAADF-STEM) images were collected from selected regions of the samples. TEM-EDS spectra and elemental maps were acquired to examine the local distribution of Ni, Ti, O and N where detectable. Cu signals in the EDS spectra were assigned mainly to the TEM grid. N signals, where present, were used as qualitative compositional information. Since Li

and H cannot be reliably detected by conventional TEM-EDS, assignment of LiH, Li_2NH and Li_3N was based primarily on XRD.

HRTEM images and fast Fourier transform analysis were used where lattice fringes were sufficiently resolved. The measured fringe spacings were compared with reference values for TiO_2- and Li-N-containing phases. These assignments served as supplementary local structural evidence rather than as definitive phase identification.

3.3.4 X-ray photoelectron spectroscopy

XPS was used to examine the elemental composition and chemical-state environment within the near-surface region of selected TiO2-Ni-LiH samples. In this study, the Li 1s, N 1s, O 1s, Ti 2p and Ni 2p regions were analysed to assess the surface exposure and chemical environments of Li-, N-, O-, Ti- and Ni-containing species in the as-prepared composite. XPS measurements were conducted using a Thermo Fisher Scientific Nexsa G2 system. The sealed sample container was opened immediately before mounting, and the mounted sample was transferred into the XPS load-lock as quickly as possible. The typical air exposure during mounting and transfer was kept below approximately 30 s at room temperature and approximately 40% relative humidity.

Survey spectra and high-resolution scans were collected for selected core-level regions, including C 1s, Li 1s, N 1s, O 1s, Ti 2p and, where detectable, Ni 2p. Binding energies were charge-corrected using the C 1s signal at 284.8 eV where applicable. Because XPS

probes only the near-surface region, and because LiH-based materials are sensitive to oxygen and moisture, the XPS results were interpreted as near-surface compositional information after rapid transfer rather than as a direct measure of bulk phase composition. Phase identification of Li-N-H species was based primarily on XRD.

3.4 Evaluation of CLAS performance

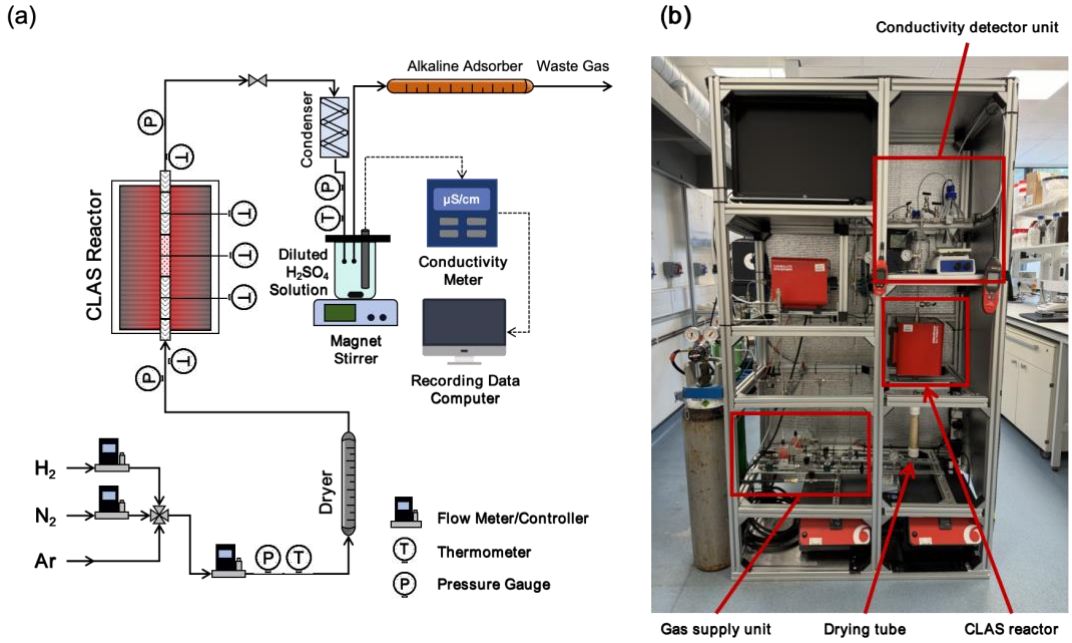


Figure 3.2. Lab-scale CLAS reactor system.
(a) Schematic diagram of the gas supply, fixed-bed reactor, ammonia absorption and conductivity measurement system. **(b)** Photograph of the assembled reactor system.

The CLAS performance of the prepared LiH-based composites was evaluated using a lab-scale fixed-bed CLAS reactor system. The system was designed to expose the solid nitrogen carrier alternately to N_2 and H_2, corresponding to the nitridation and hydrogenation steps of the CLAS cycle. Ammonia produced during the hydrogenation

step was absorbed in dilute sulfuric acid and quantified by conductivity measurement. A schematic diagram and photograph of the reactor system are shown in **Figure 3.2**.

3.4.1 Test rig setup

The CLAS reactor was placed inside a single zone split tube furnace (Carbolite Gero). The furnace has a maximum operating temperature of 1200 ℃, a heated length of 150 mm and a maximum compatible work-tube outer diameter of 60 mm. The reactor tube was a quick-release alumina ceramic tube supplied by Zhengzhou Bangda Ltd., with an inner diameter of 25 mm, an outer diameter of 27 mm, and a length of 500 mm. The quick-release design allowed the sample to be loaded inside the glove box and transferred to the test rig with limited exposure to air.

As shown in **Figure 3.3**, the sample was positioned in the central heated region of the furnace. Fine quartz wool was used to hold the powder in place while allowing gas to pass through the packed bed. Alumina ceramic spacers were placed on both sides of the sample zone to confine the heated region and reduce heat transfer towards the sealing ends of the reactor. After loading, both ends of the reactor were sealed using bonnet needle valves to minimise oxidation or hydrolysis of the hydride-containing samples during transfer and installation.

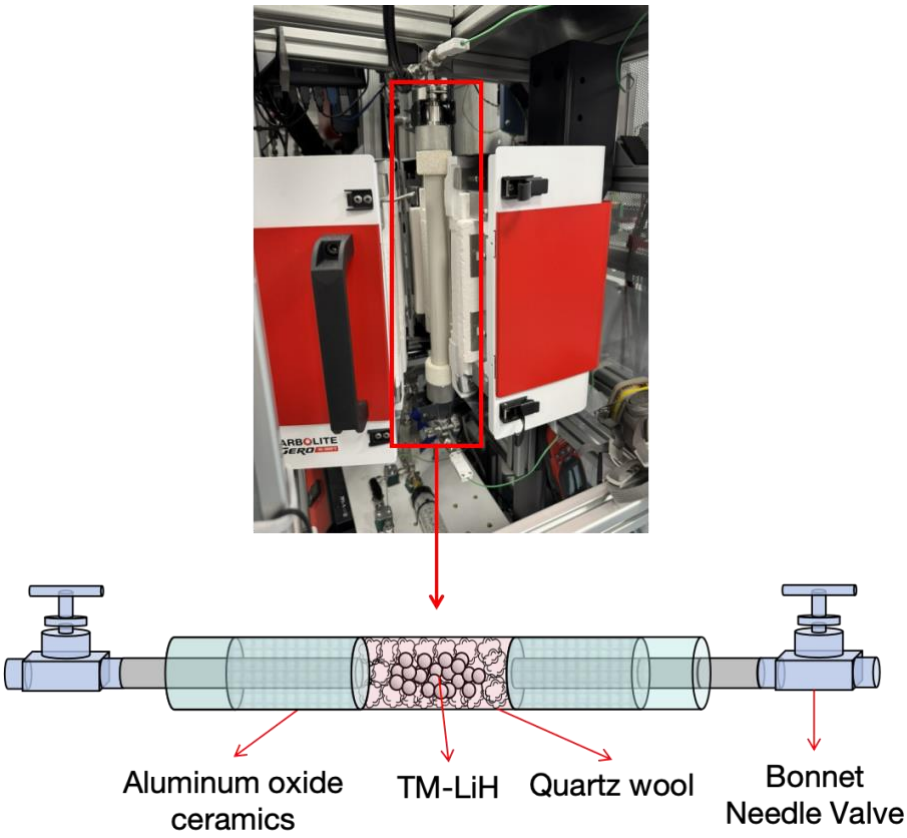


Figure 3.3. Sample loading configuration inside the CLAS reactor.

3.4.2 Gas supply, flow control and temperature monitoring

High-purity N_2 and Ar gases were supplied from BOC cylinders with a stated purity of 99.9%. Hydrogen was supplied by a THALESNano H-Genie hydrogen generator with a stated purity of 99.9%. N_2 was used for the nitridation step, H_2 was used for the hydrogenation step, and Ar was used to purge the reactor and gas lines before heating, between reaction steps and during cooling.

Gas flow rates were controlled using Bronkhorst EL-FLOW mass flow controllers. The N_2 controller had a calibrated flow range of 0.01-2 L min^{-1}, while the H_2 controller had a calibrated flow range of 0.01-2 L min^{-1}. The gas lines were assembled using 1/4 inch

316 stainless steel tubing with Swagelok valves and fittings. Before entering the reactor, the inlet gas passed through a Molecular Sieve 5 Å moisture trap with a volume of 750 cc and 1/4 inch fittings. This drying step was used to reduce water contamination in the inlet gas, because LiH and LiH-based composites are highly sensitive to moisture and oxygen.

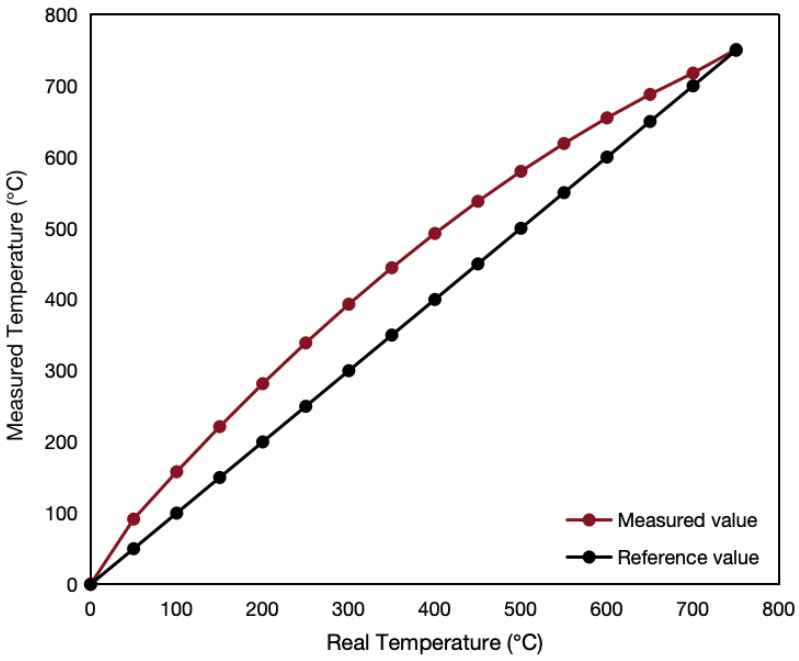


Figure 3.4. Calibration of furnace setpoint against reaction-zone temperature under Ar flow.

Pressure gauges were installed at selected positions in the gas line to monitor the pressure and pressure changes during operation. RS PRO G 1/4 Type pressure gauges with a 0-10 bar range were used for this purpose. The pressure readings were used to identify abnormal pressure changes, which could indicate leakage, flow restriction or blockage within the reactor or downstream absorption system.

Temperature was monitored using mineral-insulated Type K thermocouples (TC Ltd). Thermocouples were positioned at the reactor inlet, reactor outlet, external side of the reactor and close to the sample bed. The thermocouple close to the sample bed was used as the main reference for the reaction-zone temperature. The inlet, outlet and external reactor measurements were used to check temperature gradients across the reactor and to confirm stable heating during CLAS operation.

Before CLAS testing, the temperature profile of the reactor was calibrated under continuous Ar flow. A Type K thermocouple was positioned near the sample bed, and the reactor was incrementally heated to establish a correlation between the furnace setpoint and the actual reaction-zone temperature. The calibration was repeated three times under the same Ar flow conditions. As no chemical reaction occurred during calibration, the measured temperature-setpoint relationships were highly reproducible, and no appreciable difference was observed among the three runs. The values shown in **Figure 3.4** represent the mean of the three measurements.

3.4.3 CLAS testing procedure

For a typical test, 100 mg of LiH-based composite was loaded into the reactor inside the glove box. The sample was held in place using fine quartz wool and positioned between alumina ceramic spacers. After loading, the reactor was sealed with bonnet needle valves, removed from the glove box and connected to the CLAS reactor system.

Before heating, the reactor and gas lines were purged with Ar for 5 min to remove residual air. The reactor was then heated to the target reaction temperature under flowing Ar. The operating temperature was typically varied between 250 ℃ and 400 ℃ depending on the experiment. Once the sample-zone temperature stabilised, the gas was switched to N_2 to start the nitridation step. Unless otherwise stated, N_2 was supplied at 100 mL min^{-1} for 15 min. The reactor was operated at atmospheric pressure, approximately 101 kPa absolute. During this stage, LiH-based materials were anticipated to react with N_2 to form Li_2NH or related nitrogen-containing intermediates.

Following nitridation, the N_2 flow was discontinued and the reactor was purged with Ar. H_2 was then introduced at a flow rate of 100 mL min^{-1} for 15 minutes to perform the hydrogenation step under the same near-atmospheric pressure condition. During hydrogenation, the nitrogen-containing intermediate reacted with H_2 to generate NH_3 and regenerate the hydride phase. In the present composite system, hydrogenation was treated as a promoter-assisted solid-gas reaction. Ni may facilitate H_2 activation and hydrogen transfer at Ni-LiH or Ni-Li-N-H interfaces, while the Li-N-H intermediate participates directly in NH_3 formation and restoration of the hydride phase. The outlet gas was subsequently directed into the downstream absorption system for ammonia quantification.

During each test, pressure and temperature were monitored continuously. Pressure gauges were used to monitor the process pressure and detect abnormal pressure changes,

which could indicate blockages or flow restrictions in the reactor bed or downstream line. Under normal operation, the reactor remained close to atmospheric pressure, with only minor pressure variation arising from the packed bed and downstream absorption system. Thermocouples positioned at the reactor inlet, reactor outlet, reactor exterior and sample-bed region were used to confirm that stable operating conditions were achieved before gas switching.

For selected experiments, reaction temperature, gas flow rate, hydrogenation duration and cycle number were systematically varied to assess their effects on ammonia production. After each test, the reactor was cooled under Ar before disconnection or sample recovery.

3.4.4 Ammonia absorption and conductivity measurement

Ammonia produced during hydrogenation was quantified using acid absorption followed by conductivity measurement [23]. The reactor outlet gas was bubbled through dilute sulfuric acid prepared by diluting 20 mL of 0.1 M H_2SO_4 with 1980 mL of deionised water, giving a final concentration of H_2SO_4 of 1 mmol L^{-1}. The solution was prepared as an absorption solution and used to collect ammonia during CLAS testing. The generated NH_3 was absorbed into the dilute sulfuric acid solution and converted to ammonium ions, leading to a measurable decrease in conductivity. The conductivity was measured using a Chauvin Arnoux P01710020 conductivity meter with a measurement range up to 500 mS cm^{-1} and a resolution of 0.1 μS cm^{-1}. The

absorption bottle was placed on an RS PRO magnetic stirrer to maintain solution mixing during gas bubbling. A second reagent bottle containing 0.1 M NaOH solution was placed downstream as a secondary safety washing bottle to minimise possible carryover from the acid absorption solution.

The conductivity response was calibrated by adding known amounts of diluted ammonia solution to dilute H_2SO_4 at 25 ℃. Since the added ammonia solution also introduced water into the absorption solution, a blank correction was applied to account for dilution effects. For each calibration point, the conductivity change caused by adding the same volume of deionised water was measured separately. The corrected conductivity decrease was calculated using **Eq. 10**:

$$\Delta\kappa_{corr}\ (\mu S\ cm^{-1}) = (\kappa_0 - \kappa_{NH3}) - (\kappa_0 - \kappa_{water}) = \kappa_{water} - \kappa_{NH3} \qquad (10)$$

where $\Delta\kappa_{corr}$ is the dilution-corrected conductivity decrease, κ_0 is the initial conductivity of the H_2SO_4 solution, κ_{NH3} is the conductivity after adding diluted ammonia solution, and κ_{water} is the conductivity after adding the same volume of deionised water. The amount of ammonia was then calculated from the corrected conductivity decrease using **Eq. 11**:

$$n_{NH_3} = 8.0426 \times \Delta\kappa_{corr}\ (\mu S\ cm^{-1}) \qquad (11)$$

where n_{NH3} is the amount of ammonia produced in μmol, and $\Delta\kappa_{corr}$ is the change in conductivity corrected after the measurement during the experiment. The coefficient 8.0426 μmol NH_3 per μS cm^{-1} was obtained from the calibration curve under the same

acid concentration, solution volume and conductivity measurement conditions used for the CLAS experiments, as shown in **Figure 3.5a**.

Because conductivity is temperature-dependent, conductivity values were corrected to a reference temperature of 25 ℃ using **Eq. 12:**

$$\sigma_{\text{displayed}} = \frac{\sigma_T}{1 + \alpha(T - T_{ref})} \tag{12}$$

where $\sigma_{displayed}$ is the temperature-corrected conductivity, σ_T is the measured conductivity at temperature T, α is the temperature correction coefficient, and T_{ref} is the reference temperature of 25 ℃. The temperature-correction equation follows the temperature-compensation approach specified for the conductivity meter, while the correction coefficient used in this thesis was determined experimentally under the present absorption-solution conditions. Conductivity values of the dilute H_2SO_4 absorption solution were measured at different temperatures, and α was determined to be 1.46% $℃^{-1}$ from these calibration measurements. **Figure 3.5b** compares the measured conductivity values with the values corrected to 25 ℃ using this coefficient. The agreement confirms that the correction procedure was appropriate for the acid concentration, solution volume and temperature range used in this work.

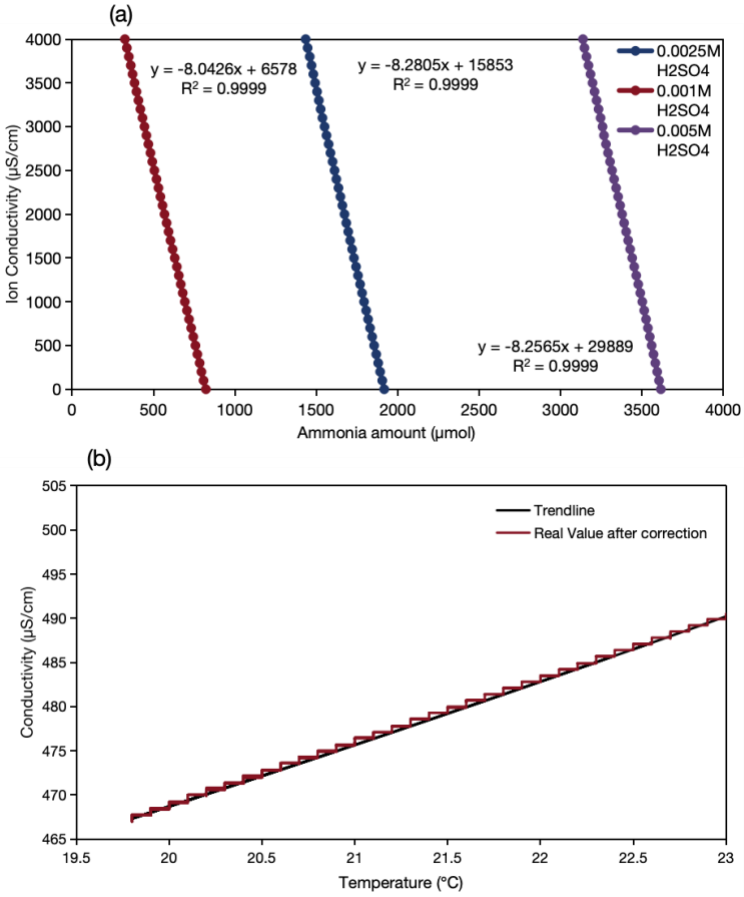


Figure 3.5. Conductivity calibration and temperature correction for NH_3 quantification. **(a)** Calibration curves relating NH_3 amount to the corrected conductivity of dilute H_2SO_4 solutions. **(b)** Temperature correction of conductivity values measured using the dilute H_2SO_4 absorption solution.

The ammonia production rate was calculated using **Eqs. 13-14**:

$$r_{NH_3-m} = \frac{n_{NH_3}}{m \times (t_{\text{nitridation}} + t_{hydrogenation})} \quad (13)$$

$$r_{NH_3-mLiH} = \frac{n_{NH_3}}{m_{LiH} \times (t_{\text{nitridation}} + t_{hydrogenation})} \quad (14)$$

where $r_{NH3\text{-}m}$ is the sample-normalised ammonia production rate in μmol g^{-1} h^{-1}, and $r_{NH3\text{-}mLiH}$ is the LiH-normalised ammonia production rate in μmol g_{LiH}^{-1} h^{-1}. n_{NH3} is the amount of ammonia produced, m is the total mass of the tested sample, and m_{LiH} is the

mass of LiH contained in the tested composite. $t_{nitridation}$ and $t_{hydrogenation}$ are the reaction times for the N_2 and H_2 steps, respectively. Unless otherwise stated, NH_3 production rates reported in **Chapter 4** were normalised to the LiH content. The apparent single-pass gas utilisation was estimated from the amount of NH_3 produced and the amount of gas supplied during each 15 min half-cycle. Because CLAS separates N_2 fixation and H_2 hydrogenation, this value should be interpreted as an apparent gas utilisation rather than a conventional Haber-Bosch single-pass conversion. Assuming a molar gas volume of 24.45 L mol^{-1} at ambient conditions, the apparent N_2 utilisation was calculated as $n_{NH3}/(2n_{N2,in})$, and the apparent H_2 utilisation was calculated as $3n_{NH3}/(2n_{H2,in})$, where n_{NH3} is the amount of ammonia produced, and n_{N2} and n_{H2} are the amount of N_2 used in nitridation step and the H_2 used in hydrogenation step respectively.

3.4.5 Main equipment and operating parameters

Table 3.2. Main equipment and operating parameters used in the CLAS reactor system.

Component	Specification
CLAS reactor	Quick-release alumina ceramic tube, 25 mm inner diameter, 27 mm outer diameter, 500 mm length
Furnace	Carbolite Gero TS1 12/60/150 split tube furnace, 1200 °C maximum temperature, 150 mm heated length
Sample loading	100 mg of LiH-based composite held by quartz wool between alumina ceramic spacers
Temperature measurement	Type K mineral-insulated thermocouples, 0.5 mm diameter
Temperature monitoring positions	Reactor inlet, reactor outlet, external reactor side and close to the sample bed
Pressure monitoring	RS PRO G 1/4 Type G pressure gauges, 63 mm dial, 0-10 bar range
N_2 supply	BOC N_2, 99.9%
Ar supply	BOC Ar, 99.9%
H_2 supply	THALESNano H-Genie hydrogen generator, 99.9%
Flow control	Bronkhorst EL-FLOW Select F-201CV mass flow controllers
Gas drying unit	Molecular Sieve 5Å moisture trap, 750 cc, 1/4 inch fittings
Tubing and fittings	1/4 inch 316 stainless steel tubing with Swagelok valves and fittings
Ammonia absorption solution	1 mmol L^{-1} H_2SO_4, prepared from 20 mL of 0.1 M H_2SO_4 and 1980 mL of deionised water
Secondary absorption bottle	0.1 M NaOH
Conductivity meter	Chauvin Arnoux P01710020 conductivity meter

4. Results and Discussion

This chapter links the structural features of LiH-based composites with their chemical looping ammonia synthesis performance in a fixed-bed reactor. The results are organised to distinguish three related factors: promoter-assisted nitrogen activation, LiH-mediated nitrogen storage and hydrogenation, and gas-solid accessibility in the packed bed. First, the initial morphology of representative ball-milled composites is examined to establish how transition metal and support addition modify the powder structure. The composition-performance relationship is then evaluated by screening transition metal promoters, promoter loading and support materials. After TiO_2-supported Ni-LiH is identified as the most effective supported system, XRD, SEM-EDS, TEM-EDS, HRTEM and XPS are used to examine phase evolution, local elemental distribution and near-surface chemistry. Finally, fixed-bed operating behaviour is analysed by varying reaction temperature, reaction time, gas flow, cycling and sample loading to determine how reactor operation affects the apparent utilisation of the active LiH phase.

Unless otherwise stated, the standard test condition used 100 mg of composite, N_2 and H_2 flow rates of 100 mL min^{-1}, and 15 min for each nitridation and hydrogenation step. Ammonia was quantified by acid absorption and conductivity measurement using the calibration coefficient described in **Section 3.4.4**. Ammonia production rates are

reported on a LiH-normalised basis unless explicitly stated otherwise, because LiH is the hydride component participating in the Li-N-H nitrogen-carrier cycle.

4.1 Initial morphology of LiH-based composites

SEM was used to compare the particle morphology and agglomeration behaviour of LiH, Fe-LiH, 50 wt.% Ni-LiH and 10 wt.% TiO_2-50 wt.% Ni-LiH. Representative images are shown in **Figure 4.1**. This comparison was used to establish how transition metal addition and support addition affect the powder structure before CLAS testing.

Pure LiH showed irregular aggregates with a broad particle-size distribution. At low magnification, the powder consisted of large agglomerated regions mixed with smaller particles. At higher magnification, block-like and plate-like fragments were observed, with fine secondary particles attached to larger LiH domains. This morphology demonstrates that untreated LiH forms non-uniform clustered regions, potentially limiting the hydride surface area accessible to gas-phase N_2 and H_2 during CLAS cycling. Fe-LiH maintained a compact and irregular agglomerated structure following ball milling. Both coarse fragments and fine particles were present, yet the powder continued to exhibit large, clustered regions. These observations indicate that transition metal addition alone does not necessarily yield an open or well-dispersed composite structure.

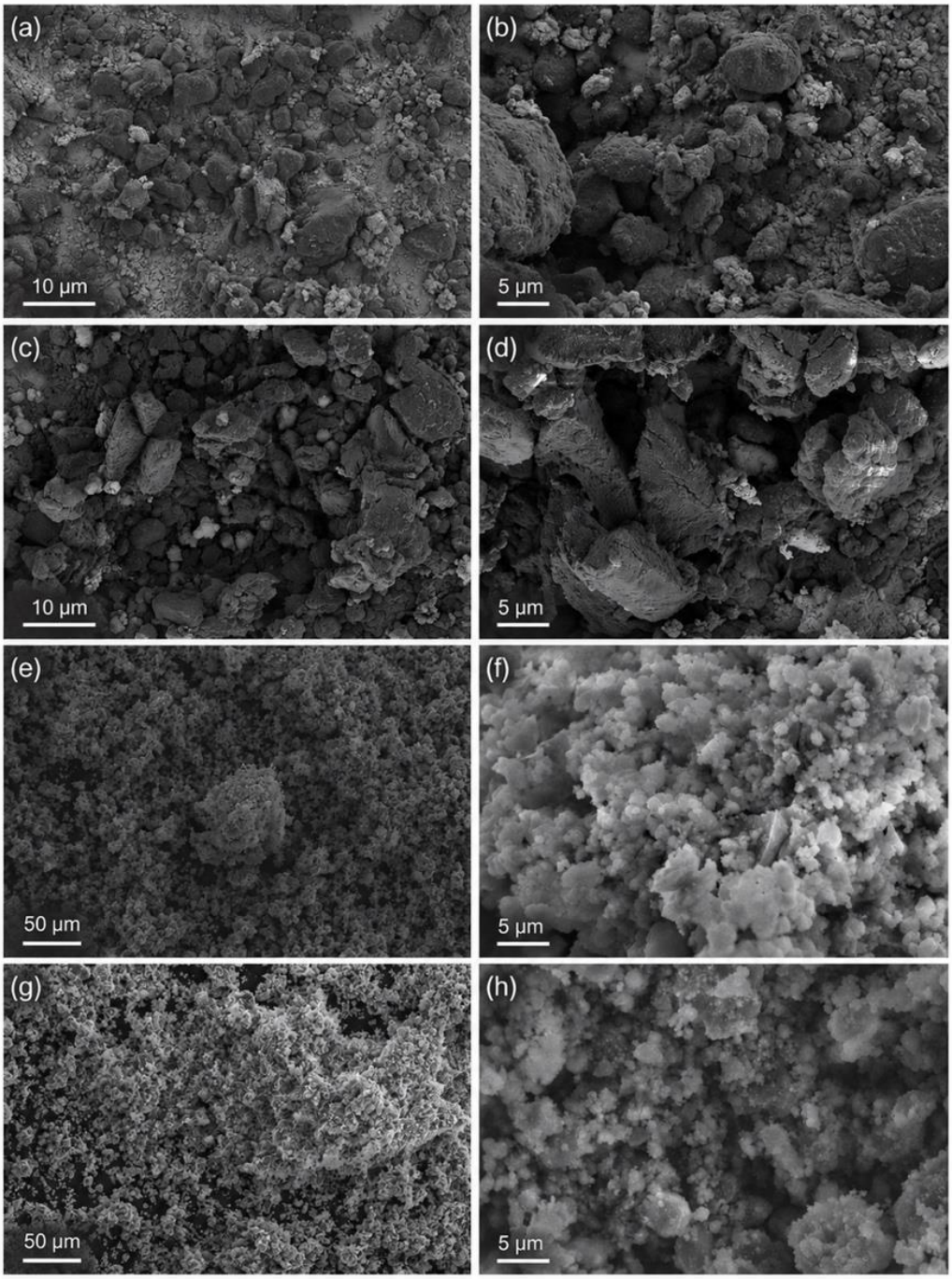


Figure 4.1. SEM images of LiH and LiH-based composites.

(a, b) LiH. **(c, d)** Fe-LiH. **(e, f)** 50 wt.% Ni-LiH. **(g, h)** 10 wt.% TiO_2-50 wt.% Ni-LiH.

The 50 wt.% Ni-LiH composite exhibited finer secondary particles distributed across larger agglomerates. This morphology is consistent with mechanical contact between Ni and LiH produced during ball milling. However, the composite retained compact

agglomerated regions, which may restrict gas access to internal LiH-containing domains. Consequently, even when Ni acts as an effective chemical promoter, the performance of Ni-LiH may remain limited by particle packing and gas-solid accessibility.

In contrast, the 10 wt.% TiO_2-50 wt.% Ni-LiH composite showed a more fragmented and granular morphology. Compared with unsupported Ni-LiH, the TiO_2-supported sample appeared less compact and contained a higher density of small particles surrounding larger fragments. These findings indicate that TiO_2 addition alters the agglomeration state of the ball-milled composite and promotes a more open particulate texture. This structural difference establishes an initial basis for the support-assisted performance improvement discussed later in this chapter.

Overall, the SEM comparison shows that LiH-based CLAS performance cannot be interpreted only by chemical composition. The physical arrangement of LiH, transition metal promoter and support also determine how much of the hydride phase is available to gas-phase N_2 and H_2 during cycling. The support effect therefore begins before reaction: TiO_2 changes the powder architecture of Ni-LiH by reducing dense agglomeration and producing a more fragmented composite texture. This structural change provides a basis for the later performance enhancement, because hydride-imide cycling requires repeated N_2 access, formation of Li-N-H intermediates and subsequent H_2 exposure during hydrogenation.

4.2 Effect of transition metal promoter and loading

This section examines the effect of the identity and loading of transition metal promoters in LiH-based composites. In LiH-mediated ammonia synthesis, the transition metal and LiH are expected to act cooperatively. Transition metals can promote N_2 activation, while LiH participates in nitrogen transfer and hydrogenation through Li-N-H intermediates such as Li_2NH and $LiNH_2$ [128]. This relayed reaction framework motivates the introduction of transition metals into LiH-based CLAS materials.

In this work, Ni, Co, Mn and Fe were selected as representative transition metal promoters. The first part of this section compares 50 wt.% TM-LiH composites to identify the most effective promoter. The second part examines the effect of promoter loading, with particular focus on Ni-LiH because Ni gave the highest NH_3 production rate among the tested materials.

4.2.1 Screening of transition metal promoters

The initial promoter comparison was conducted using 50 wt.% TM-LiH composites, where TM represents Ni, Co, Mn or Fe. A promoter loading of 50 wt.% was selected as the starting composition based on previous hydride-imide CLAS studies, where high transition-metal contents have been shown to provide elevated ammonia production performance [128]. This composition was therefore used to compare promoter effects under the same preparation and testing conditions before further optimisation of promoter loading.

The 50 wt.% TM-LiH composites were prepared by ball milling and tested in the fixed-bed CLAS reactor under alternating N_2 and H_2 flow. The tests were conducted using 100 mg of composite sample, atmospheric pressure, N_2 and H_2 flow rates of 100 mL min^{-1}, and 15 min for each nitridation and hydrogenation step. **Figure 4.2** compares the NH_3 production rates of pure LiH and 50 wt.% TM-LiH composites at 275 and 300 °C.

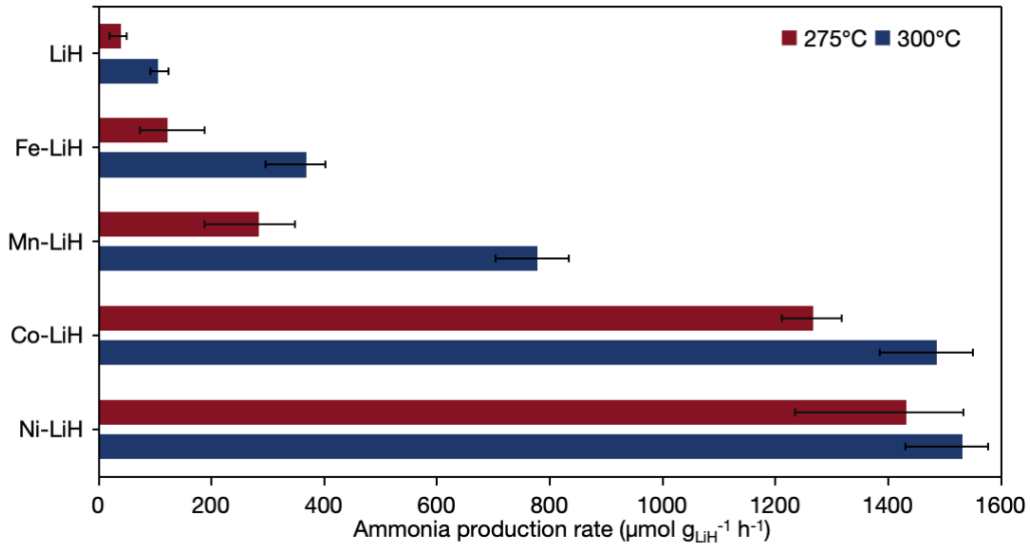


Figure 4.2. NH_3 production rates of pure LiH and 50 wt.% TM-LiH composites under ambient pressure CLAS processes.

Pure LiH showed limited NH_3 production under the tested conditions, indicating that LiH alone had low reactivity in the present low-pressure cycling configuration. The introduction of transition metals substantially increased the NH_3 production rate, demonstrating the importance of metal-assisted promotion in LiH-based CLAS. Among the tested composites, Ni-LiH and Co-LiH showed the highest NH_3 production rates, while Mn-LiH and Fe-LiH gave lower values. At 300 °C, the 50 wt.% Ni-LiH composite reached approximately 1531 μmol g_{LiH}^{-1} h^{-1}, which is comparable to the

performance reported for Ni-promoted hydride-imide CLAS systems in the literature [23].

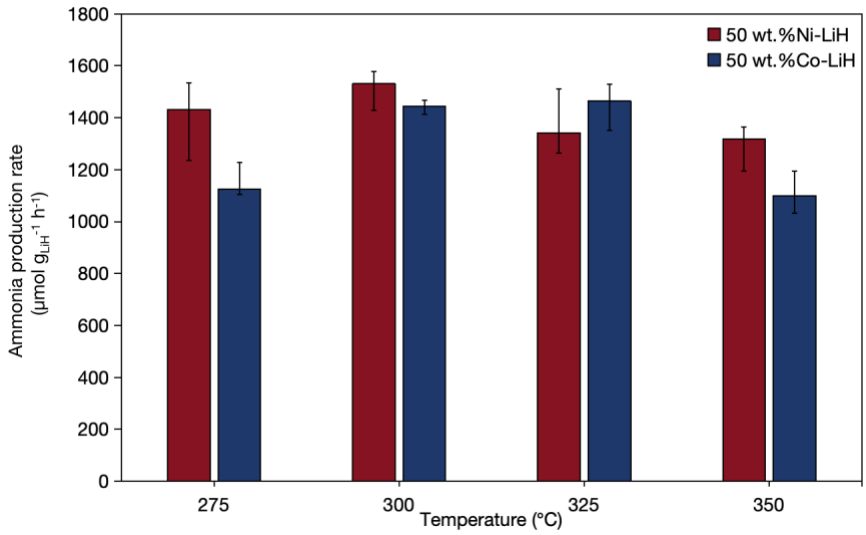


Figure 4.3. Comparison of the NH_3 production rates of 50 wt.% Ni-LiH and 50 wt.% Co-LiH at different reaction temperatures under ambient-pressure CLAS conditions.

The promoter-dependent trend indicates that effective LiH-mediated CLAS requires coupling between transition-metal-assisted N_2 activation and LiH-mediated nitrogen transfer and hydrogenation. Previous studies of TM-LiH systems proposed that transition metals activate N_2, while LiH accepts activated nitrogen and participates in subsequent hydrogenation through Li-N-H intermediates. An effective promoter must therefore provide N_2 activation while maintaining productive contact with the hydride phase. The strong performance of Ni-LiH and Co-LiH indicates that both metals provide effective promoter-hydride coupling under the tested conditions.

The comparison in **Figure 4.2** identified Ni-LiH and Co-LiH as the two most active promoted composites. Their performance was therefore compared over a wider temperature range from 275 to 350 ℃, as shown in **Figure 4.3**. Each value represents the mean of three independent experiments, and error bars indicate one standard deviation.

Ni-LiH showed higher mean NH_3 production rates than Co-LiH at 275, 300 and 350 ℃, whereas Co-LiH gave a slightly higher mean rate at 325 ℃. Ni-LiH achieved the highest overall rate at 300 ℃ and maintained stronger performance across most of the investigated temperature range. The comparison also shows that the relative performance of Ni and Co depends on reaction temperature rather than following a fixed promoter ranking. Based on its higher maximum rate and stronger overall performance, Ni was selected for subsequent promoter-loading optimisation.

4.2.2 Effect of promoter loading

Following the promoter screening and the direct comparison with Co-LiH, the influence of Ni loading was examined. **Figure 4.4** shows the NH_3 production rates of Ni-LiH composites with different Ni contents at 300 ℃. This temperature was selected for the loading comparison because Ni-LiH showed a strong and reproducible response under this condition in the initial promoter comparison.

Introducing Ni into LiH markedly increased the NH_3 production rate. The rate increased rapidly as the Ni content was raised from 10 to 30 wt.%, followed by a slower increase

between 30 and 50 wt.%. The highest NH_3 production rate was obtained at 50 wt.% Ni. Further increasing the Ni fraction to 60-90 wt.% led to a gradual decrease in the measured rate. This non-linear dependence shows that Ni loading controls the balance between promoter-assisted nitrogen activation and the amount of LiH available for nitrogen transfer and hydrogenation.

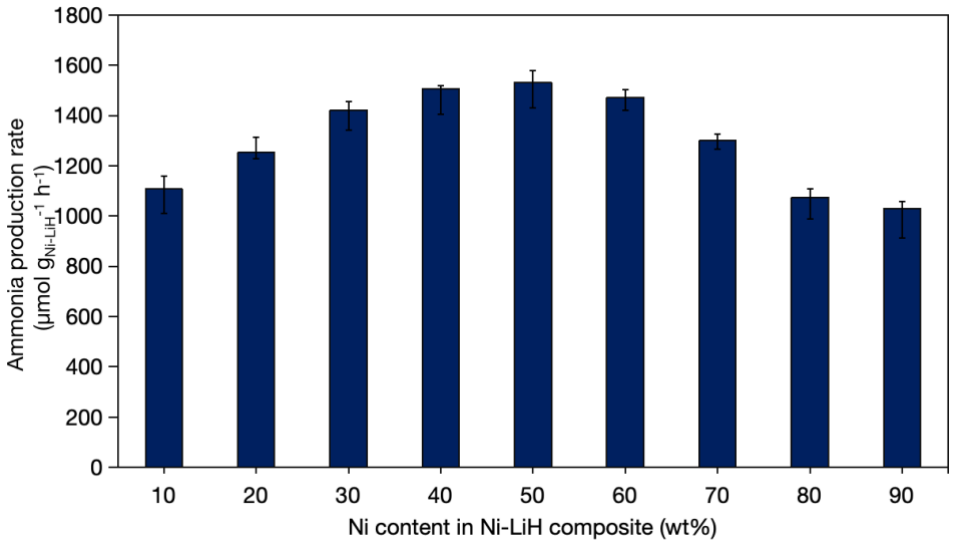


Figure 4.4. Effect of Ni loading on NH_3 production rate over Ni-LiH composites at 300 °C.

The Ni loading dependence shows that ammonia production is controlled by an interfacial balance rather than by Ni content alone. At low Ni loading, the number of Ni-LiH contact regions is limited, restricting the extent of Ni-assisted N_2 activation and subsequent nitrogen transfer to the hydride phase. Increasing the Ni content increases the probability of forming productive metal-hydride contact during ball milling, which explains the increase in ammonia production from low to intermediate Ni loading.

At high Ni loading, however, the rate decreases even though more metal is present. Because the rates are normalised to LiH content, this decrease should not be assigned simply to dilution of LiH by Ni. Instead, it indicates a decrease in the effective utilisation of the remaining LiH. Excessive Ni may generate metal-rich regions that are not well coupled to LiH, reduce the continuity of LiH-containing domains, or produce denser particle packing that limits gas access to internal hydride regions. The optimum around 50 wt.% Ni therefore reflects a balance between sufficient Ni-assisted nitrogen activation and accessible LiH-mediated nitrogen storage and hydrogenation.

To further examine whether this loading dependence was specific to 300 ℃ or reflected a broader compositional trend, the NH_3 production rates were compared across both Ni loading and reaction temperature, as shown in **Figure 4.5**. The temperature-loading matrix shows that the highest performance region is centred around 40-60 wt.% Ni and 275-325 ℃, with the maximum value obtained at 50 wt.% Ni and 300 ℃. This indicates that the optimum Ni content is not an isolated result from a single temperature test but arises from the combined effect of promoter loading and reaction temperature. At lower temperatures, increasing Ni loading improves the reaction rate by enhancing metal-hydride contact, whereas at higher Ni contents the reduced LiH fraction limits further improvement. This two-parameter trend supports the selection of 50 wt.% Ni-LiH as the representative composition for the subsequent process-parameter studies.

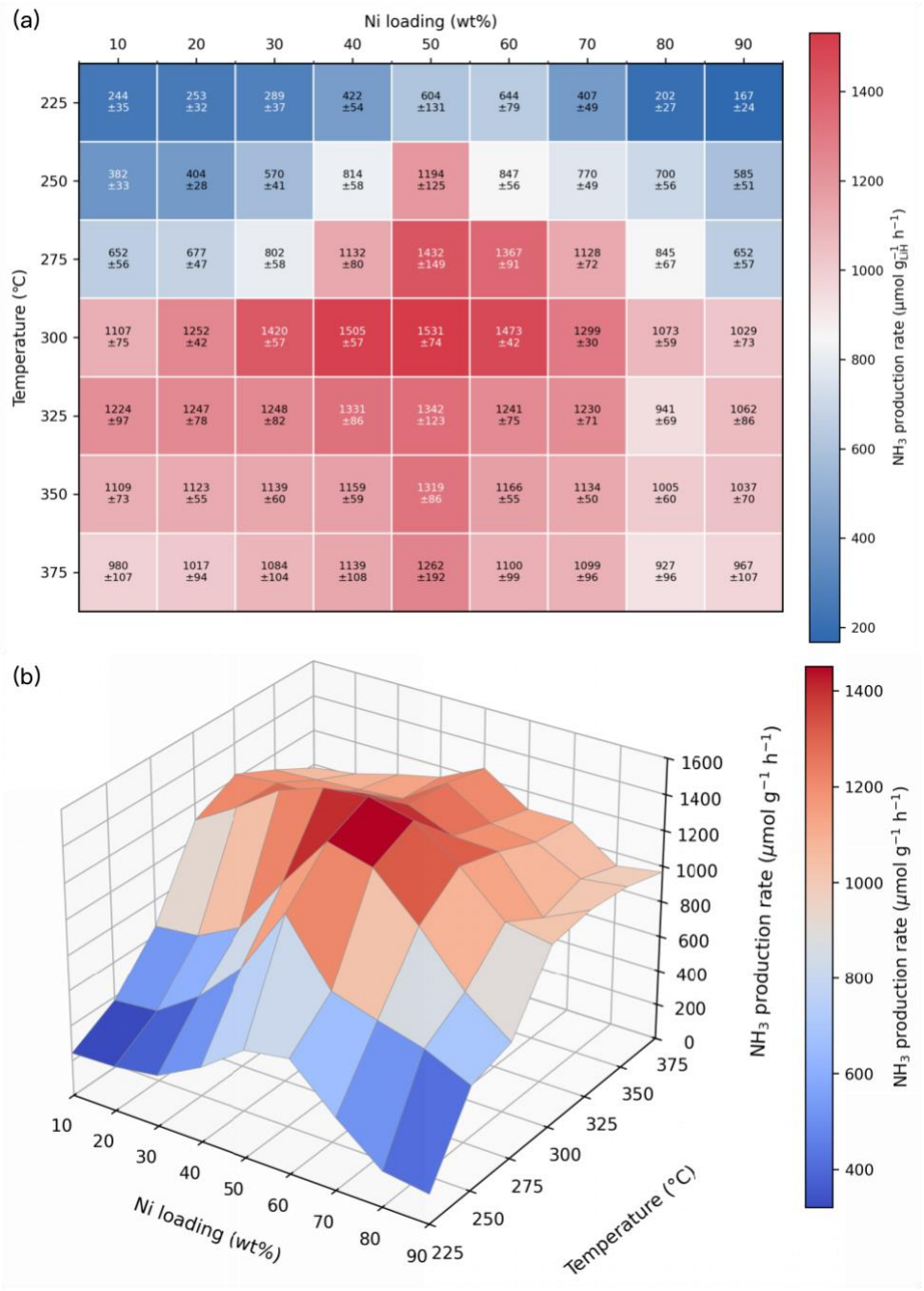


Figure 4.5. Combined effect of Ni loading and reaction temperature on NH_3 production over Ni-LiH composites.

(a) Temperature-loading matrix showing NH_3 production rates at different Ni loadings and reaction temperatures. **(b)** Three-dimensional surface representation of the same dataset.

This loading dependence is consistent with previous work on Ni-promoted hydride-imide systems. In Ni-BaH_2 based CLAS, NH_3 production also increased with Ni content up to an optimum near 50 wt.% before decreasing at higher Ni fractions [23, 131]. The similar trend suggests that the performance of metal-promoted hydride systems is governed by a common balance: sufficient transition metal is required to promote N_2 activation, but excessive metal can reduce the effective utilisation of LiH by changing particle packing, promoting aggregation, or decreasing the accessibility of reactive metal-hydride interfaces. The agreement between the Ni-LiH results and reported Ni-BaH_2 behaviour supports the selection of 50 wt.% Ni as the representative promoter loading for subsequent process-parameter studies [23].

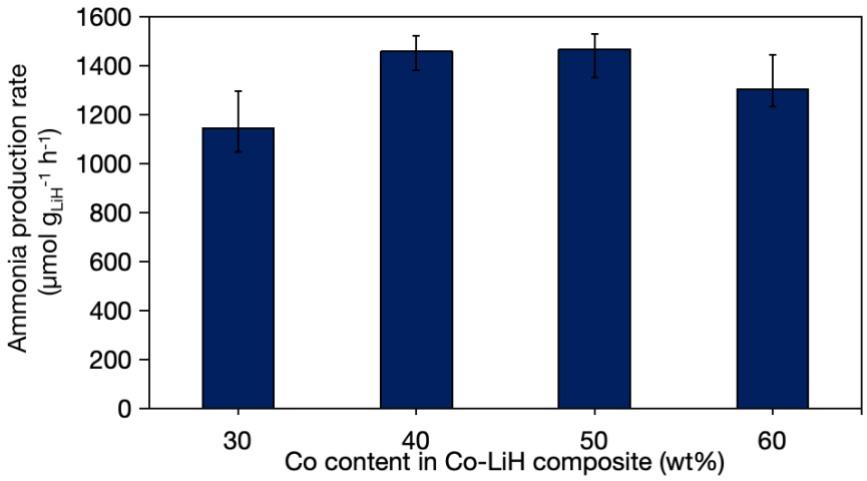


Figure 4.6. Effect of Co loading on NH_3 production rate over Co-LiH composites at 300 °C.

The Co loading study supports this interpretation. As shown in **Figure 4.6**, Co-LiH composites displayed a similar non-linear trend, with NH_3 production increasing at low

to intermediate Co contents before decreasing at higher Co fractions. This indicates that the balance between promoter-hydride contact and hydride availability is not unique to Ni. However, Ni-LiH achieved the higher maximum rate and showed stronger performance across most of the directly compared temperatures, indicating that both promoter loading and promoter identity determine the overall performance. Increasing the metal fraction can increase the number of promoter-hydride contact regions, but the effectiveness of those regions depends on the specific metal-LiH combination.

Overall, the results in this section show that transition metal promotion substantially enhances the CLAS performance of LiH-based composites. Among the tested promoters, Ni and Co produced the strongest enhancements, with Ni achieving the highest overall NH_3 production rate and showing stronger performance across most of the directly compared temperatures. The promoter and loading dependences together indicate that efficient ammonia production requires effective coupling between metal-assisted nitrogen activation and LiH-mediated nitrogen transfer and hydrogenation. Based on these results, 50 wt.% Ni-LiH was selected as the representative promoted composition for subsequent support-assisted optimisation and fixed-bed operating studies.

4.3 Support-assisted optimisation of Ni-LiH composites

Although Ni promotion substantially enhanced the CLAS performance of LiH, the results in the previous sections also show that the measured activity is sensitive to gas-

solid accessibility, particle packing and effective material utilisation. Support-assisted modification was therefore examined as a further strategy to improve the structure of Ni-LiH composites. The aim was not only to disperse the active components, but also to create a more accessible composite structure in which Ni-assisted nitrogen activation and LiH-mediated nitrogen transfer could proceed more effectively.

Five support materials were compared within the Ni-LiH system: TiO_2 and SiO_2 as oxide supports, expanded graphite (EG) and graphene nanoplatelets (GNP) as carbon-based supports, and diatomaceous earth (DE) as a porous mineral support. These materials were selected to compare support classes with different surface chemistry, particle structure and potential effects on gas-solid accessibility.

4.3.1 Screening of support materials

Figure 4.7 compares the temperature-dependent NH_3 production rates of unsupported Ni-LiH and 10 wt.% supported Ni-LiH composites. Unsupported Ni-LiH was used as the reference material for evaluating the effect of support addition.

Among the tested supports, TiO_2 produced the largest and most consistent enhancement. TiO_2-Ni-LiH showed the highest NH_3 production rate across the whole temperature range and reached its maximum at 275 °C. More importantly, the TiO_2-supported sample remained more active than unsupported Ni-LiH not only at the optimum temperature, but also at both lower and higher temperatures. This indicates that TiO_2

did not simply shift the optimum temperature; it improved the operating window of the Ni-LiH composite.

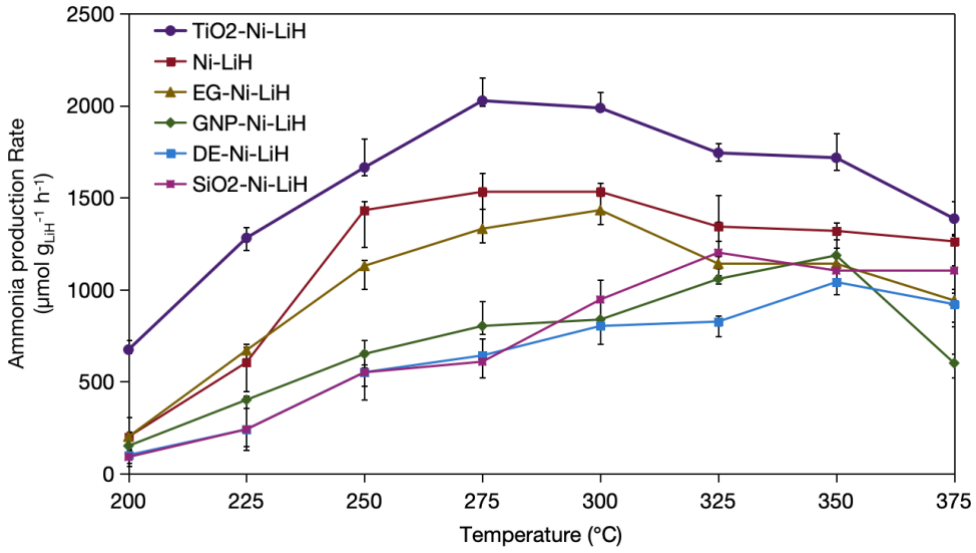


Figure 4.7. Effect of 10 wt.% support material on the NH_3 production rate of Ni-LiH composites under low-pressure CLAS conditions.

In contrast, the other support materials did not provide a clear enhancement over unsupported Ni-LiH. The carbon-based supports, EG and GNP, gave activities that were generally comparable to or lower than unsupported Ni-LiH over the main operating temperature range. Although EG approached the unsupported Ni-LiH performance at selected temperatures, the difference was small and was not sufficient to demonstrate an effective support-assisted improvement. GNP-Ni-LiH also did not show a consistent activity advantage. These results indicate that adding a high-surface-area carbon phase alone does not necessarily improve the effective utilisation of Ni-LiH in this CLAS system. The comparison shows that the improvement observed for

TiO_2 cannot be attributed simply to dilution, physical spacing or the addition of an inert solid phase. Instead, the support must maintain favourable contact with the Ni-LiH active fraction while preserving gas access to LiH-containing regions. Therefore, TiO_2 was the only support that produced a consistent and meaningful improvement in this study. The superior performance of TiO_2-Ni-LiH can be rationalised by a combination of structural and interfacial effects. TiO_2 addition may reduce compact agglomeration and produce a more fragmented composite structure during ball milling, thereby preserving more accessible gas-solid interfaces during cycling. This interpretation is supported by the SEM comparison in **Figure 4.1**, where TiO_2-Ni-LiH showed a less compact and more granular morphology than unsupported Ni-LiH. In LiH-based CLAS, this is particularly important because the reaction requires repeated formation and hydrogenation of Li-N-H intermediates. A support that suppresses agglomeration and maintains exposed reactive interfaces can therefore increase the fraction of LiH that participates effectively in the cycle. This observation is consistent with previous studies in which scaffold or confinement effects can improve LiH nitrogenation by limiting agglomeration and maintaining nanoscale reactive domains [132].

In addition to this structural role, TiO_2 may provide a more favourable oxide-metal-hydride interfacial environment than the other supports tested here. Previous studies on defective TiO_2-supported catalytic systems have shown that TiO_{2-x} species and oxygen vacancies can influence metal dispersion and interfacial electronic structure [133].

Although this effect was not directly verified in the present LiH-based system, it provides a possible basis for considering interfacial contributions in TiO_2-Ni-LiH.

Compared with the carbon-based and silica-based supports, TiO_2 provided a more effective support environment for the Ni-LiH composite. This interpretation is corroborated by the morphological and elemental distribution results presented in **Sections 4.1**, **4.4.2**, and **4.4.3**. As shown in **Figure 4.1**, TiO_2 addition changed the compact agglomerated morphology of unsupported Ni-LiH into a more fragmented, granular, and less compact particulate structure. SEM-EDS and TEM-EDS analyses further reveal local spatial associations among Ni-rich, Ti/O-rich, and N-containing regions within the composite. These structural characteristics suggest enhanced accessibility of the Ni-LiH active fraction to N_2 and H_2 during the nitridation-hydrogenation cycle, thereby supporting the observed increase in NH_3 production rate and the broader operating window of TiO_2-Ni-LiH.

Overall, the support screening results indicate that TiO_2 is the most effective support for Ni-LiH composites. In comparison to unsupported Ni-LiH and other supported samples, TiO_2-Ni-LiH exhibits both higher activity and a broader effective temperature window. The support screening included two oxide supports, TiO_2 and SiO_2; two carbon-based supports, expanded graphite and graphene nanoplatelets; and the porous mineral support diatomaceous earth. Among these materials, only TiO_2 produced a clear and consistent enhancement relative to unsupported Ni-LiH across the tested

temperature range. SiO_2 and diatomaceous earth did not provide a comparable improvement, while the carbon-based supports gave activities that were generally similar to or lower than those of unsupported Ni-LiH. The superior performance of TiO_2 therefore indicated that support effectiveness was not determined by high surface area, porosity or physical dilution alone. On this basis, TiO_2 was selected for further loading optimisation to determine the support content required to maximise NH_3 production while maintaining effective Ni-LiH contact and gas-solid accessibility.

4.3.2 Effect of TiO_2 loading

Following the support screening, TiO_2 was selected for loading optimisation because it was the only tested support that consistently increased NH_3 production relative to unsupported Ni-LiH across the investigated temperature range. The TiO_2 loading was therefore systematically varied to determine the support content that provided the most favourable balance among structural modification, Ni-LiH contact and effective LiH utilisation. **Figure 4.8** shows the NH_3 production rate as a function of TiO_2 loading and reaction temperature. The 0 wt.% TiO_2 sample represents unsupported Ni-LiH.

The incorporation of TiO_2 significantly influenced the performance of the Ni-LiH composite. A low TiO_2 loading of 5 wt.% did not consistently enhance NH_3 production, suggesting that this support content was insufficient to substantially alter the composite structure. In contrast, TiO_2 loadings of 10 to 15 wt.% resulted in clear performance improvements across the main operating temperature range. The highest NH_3

production rate was observed at 15 wt.% TiO_2 and 300 °C, reaching approximately 2050 μmol g_{LiH}^{-1} h^{-1}, while 10 wt.% TiO_2 gave consistently high rates across 275-350 °C.

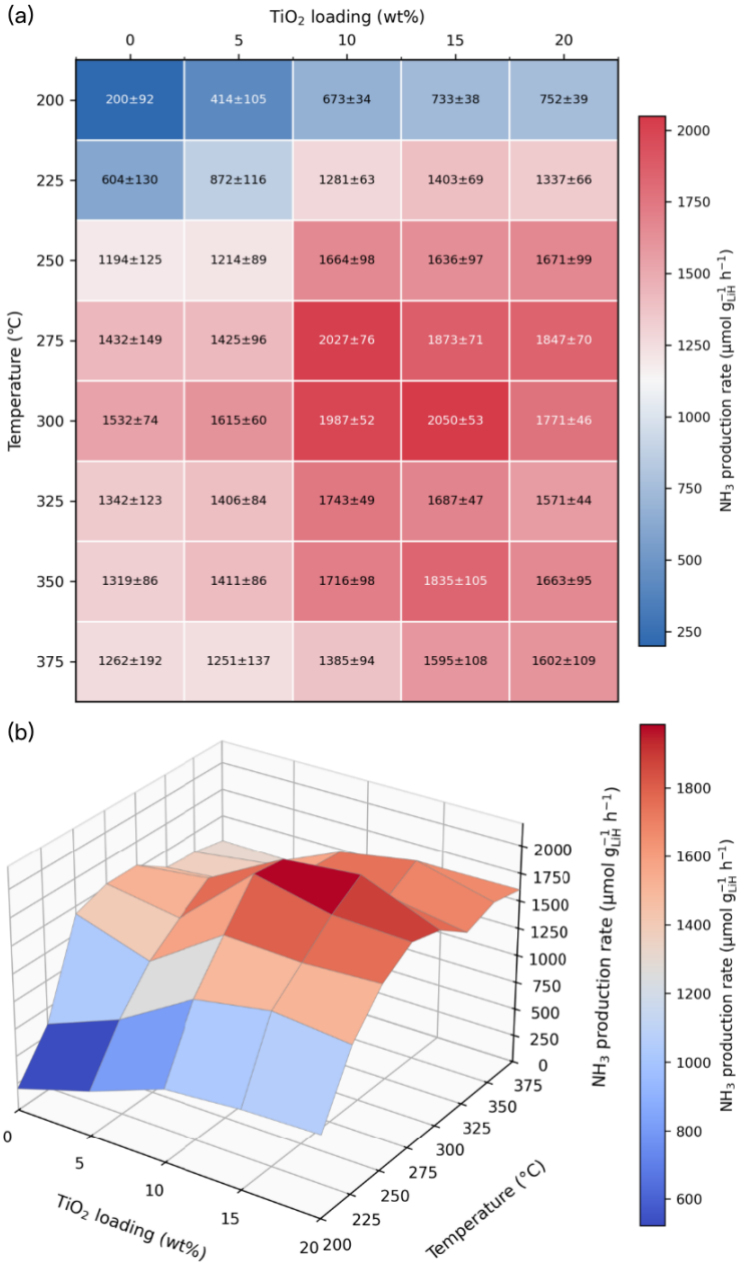


Figure 4.8. Effect of TiO_2 loading on the NH_3 production rate of TiO_2-Ni-LiH composites.

(a) Temperature-loading matrix showing NH_3 production rates at different TiO_2 loadings and reaction temperatures. **(b)** Three-dimensional surface representation of the same dataset.

The observed improvement at intermediate TiO_2 loadings suggests that support addition enhances the effective utilisation of LiH by modifying the composite structure while maintaining the proximity of active components. At an optimal loading, TiO_2 modifies the agglomeration state of the composite and promotes a more fragmented particulate structure, while maintaining local association between Ni-containing and LiH-derived reaction regions. This structural modification maintains accessible gas-solid interfaces and enhances the coupling between Ni-assisted N_2 activation, nitrogen transfer to LiH, and subsequent hydrogenation of Li-N-H intermediates. This structural modification facilitates the coupling between Ni-assisted N_2 activation, nitrogen transfer to LiH and subsequent hydrogenation of Li-N-H intermediates.

At 20 wt.% TiO_2, the activity did not improve further. Because the rates are expressed per gram of LiH, this decrease cannot be explained simply by LiH dilution. More likely, excessive TiO_2 separates Ni and LiH domains, reduces the continuity of metal-hydride contact, or places part of the LiH away from active interfacial regions. In this case, improved dispersion is offset by weaker coupling between Ni and LiH.

The temperature dependence also shows that TiO_2 loading changes the operating window of the composite. Unsupported Ni-LiH gave its best performance around 275-300 °C, whereas TiO_2-supported samples maintained high activity across a broader region from 250 to 350 °C. The best-performing compositions, especially 10 and 15 wt.% TiO_2, showed high rates in this region without the sharp loss of activity observed

for some other supported systems. This indicates that TiO_2 loading controls not only the peak rate, but also the robustness of the composite across the tested temperature range.

Overall, the TiO_2 loading study shows, as expected, that support addition has an optimum range rather than a monotonic effect. Low TiO_2 loading provides limited structural modification, while excessive TiO_2 does not further improve the performance. The most favourable region was observed at 10-15 wt.% TiO_2. In this region, 10 wt.% TiO_2 gave consistently high NH_3 production rates across the main operating temperature range, while 15 wt.% TiO_2 produced the highest single rate at 300 °C. Therefore, moderate TiO_2 loading provides the best balance between structural dispersion, accessible Ni-LiH contact and effective LiH utilisation.

4.4 Phase evolution, local structure and surface state

The performance results identified TiO_2-supported Ni-LiH as the most effective supported system among the materials tested. To understand the structural basis of this behaviour, selected TiO_2-Ni-LiH samples were analysed across several length scales. XRD was used as the primary method to identify crystalline Li-N phase evolution during nitridation. SEM-EDS and TEM-EDS were used to examine whether N-containing regions were spatially associated with Ni- and Ti/O-containing domains. HRTEM was used to provide local lattice-fringe evidence, while XPS was used to examine the near-surface composition of the as-prepared composite. These

characterisation results are interpreted together because no single technique can fully describe the air- and moisture-sensitive LiH/Li-N-H system.

4.4.1 XRD phase evolution during nitridation

XRD was used to analyse the phase evolution of 10 wt.% TiO_2-50 wt.% Ni-LiH during N_2 exposure. The samples were treated under N_2 at 300 ℃ with a flow rate of 100 mL min^{-1}. The selected nitridation times were 0, 10, 15 and 30 min. The 15 min condition corresponds to the experimental nitridation duration used in the CLAS performance tests, while 10 and 30 min represent shorter and extended N_2 exposure conditions.

Figure 4.9 shows the XRD patterns of 10 wt.% TiO_2-50 wt.% Ni-LiH after different nitridation times. In the fresh state, the crystalline pattern was dominated by LiH and metallic Ni, with Li_2O present only as a minor oxygenated crystalline phase. TiO_2-related reflections were weak, despite the nominal 10 wt.% TiO_2 loading, which is consistent with support dispersion, partial disordering after high-energy ball milling and the relatively weak diffraction contribution of the support phase. After nitridation, additional reflections associated with Li-N-containing phases appeared. The principal nitrogen-containing crystalline phase detected after N_2 exposure was Li_2NH. Li_3N was not detected after 10 min of nitridation, but appeared as a minor phase after 15 min and increased after 30 min of N_2 exposure. This phase evolution indicates that Li_2NH was the dominant crystalline nitrogen-containing product under the standard nitridation period, whereas extended N_2 exposure increased the formation of the more nitrogen-

rich Li_3N phase. $LiNH_2$ was not identified as a significant crystalline phase under these conditions. No independent reflections attributable to metallic Ti, crystalline TiN or lower titanium oxide phases were observed. Therefore, the main XRD-visible reaction-state change is the partial conversion of LiH into Li-N-containing phases, rather than an XRD-detectable transformation of TiO_2 into a new crystalline Ti-containing product.

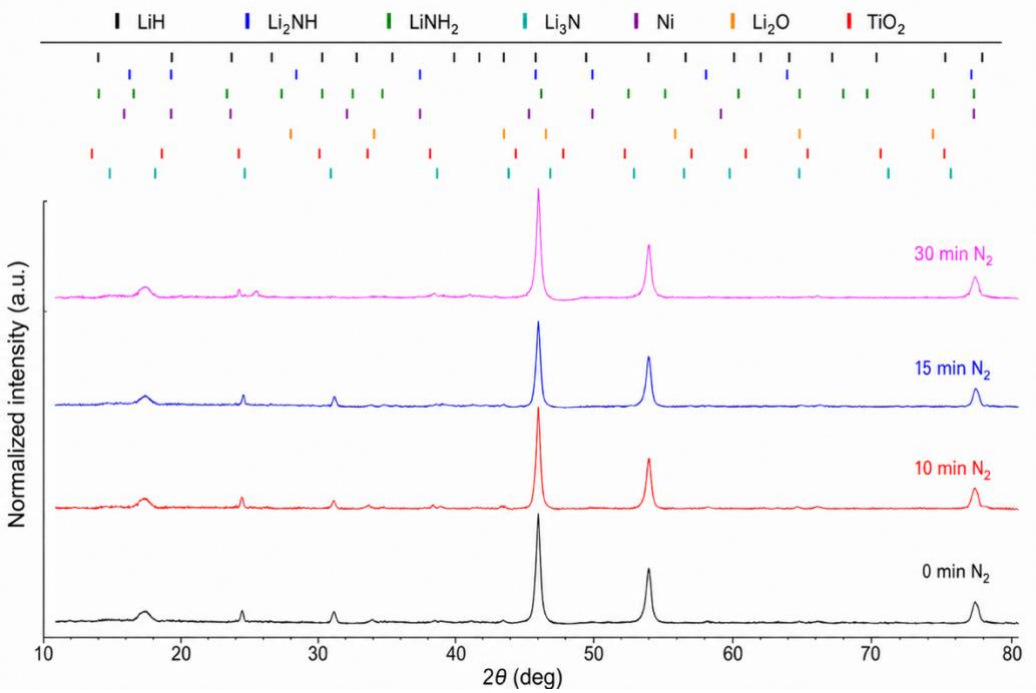


Figure 4.9. XRD patterns of 10 wt.% TiO_2-50 wt.% Ni-LiH after different N_2 exposure times during nitridation at 300 °C.

Table 4.1 summarises the crystalline phase fractions estimated from the XRD patterns. These values facilitate comparison of relative crystalline phase evolution during nitridation and are considered semi-quantitative. They do not represent the nominal composition of the ball-milled composite. In the nominal formulation, 10 wt.% TiO_2 was introduced as the support, with the remaining fraction comprising 50 wt.% Ni-LiH.

The weak TiO_2-related contribution observed in the refinement is attributed to the combined effects of low support loading, support dispersion, partial disordering during ball milling, particle-size effects, preferred orientation, and sampling heterogeneity. Consequently, the table is used to discuss the evolution of crystalline Li-containing phases rather than to determine the exact bulk composition of the composite.

Table 4.1. XRD-estimated crystalline phase fractions of 10 wt.% TiO_2-50 wt.% Ni-LiH after different N_2 exposure times.

N_2 exposure time (min)	LiH (wt.%)	Ni (wt.%)	Li_2NH (wt.%)	$LiNH_2$ (wt.%)	Li_3N (wt.%)	Li_2O (wt.%)	TiO_2 (wt.%)	Total Li-N phases (wt.%)
0	71.33	27.31	0	0	0	1.30	0.05	0
10	64.55	25.22	6.78	0	0	3.45	0	6.78
15	68.04	18.98	9.49	0	0.61	2.88	0	10.10
30	63.50	23.90	6.60	0	2.60	3.40	0	9.20

The phase fractions indicate that Li_2NH was the predominant crystalline nitrogen-containing phase detected after nitridation. $LiNH_2$ was not resolved as a significant crystalline phase, whereas Li_3N appeared as a minor phase in selected nitrided samples. The total crystalline Li-N phase fraction was approximately 7-10 wt.% after N_2 exposure, demonstrating that nitrogen was incorporated into the LiH-based solid phase during nitridation. This observation aligns with the hydride-imide reaction pathway anticipated for LiH-mediated CLAS.

The change in Li-N phase speciation provides more insight than the total Li-N fraction alone. When Li_2O is considered a minor oxygenated impurity and excluded from the phase balance, the apparent total Li-N phase fraction increases from approximately 7.02

wt.% after 10 minutes of N_2 exposure to 10.40 wt.% after 15 minutes, then decreases slightly to 9.52 wt.% after 30 minutes. Notably, the 15-minute nitrided sample remains strongly Li_2NH-rich, with Li_2NH accounting for approximately 9.77 wt.% and Li_3N for approximately 0.63 wt.% after Li_2O exclusion. After 30 minutes of N_2 exposure, the Li_2NH fraction decreases to approximately 6.83 wt.%, while the Li_3N fraction increases to approximately 2.69 wt.%. These results indicate that extended N_2 exposure does not simply increase the useful crystalline nitrogen inventory. Instead, prolonged nitridation shifts part of the LiH-derived phase from an imide-rich state toward deeper nitridation.

This phase evolution is significant for short-cycle CLAS operation. When the relative Li-N phase distribution is expressed as $Li_2NH/(Li_2NH + Li_3N)$, the apparent Li_2NH-rich fraction decreases from approximately 0.94 after 15 min N_2 exposure to 0.72 after 30 min. Conversely, the relative Li_3N-containing fraction increases from approximately 0.06 to 0.28. These values should not be interpreted as absolute selectivity, since the XRD phase fractions are semi-quantitative and do not account for amorphous or poorly crystalline Li-N-H species. Nevertheless, the data reveal a clear trend: 15 minutes of N_2 exposure favours an imide-rich crystalline state, while prolonged nitridation promotes additional Li_3N formation.

Based on the XRD-estimated phase fractions and the nitrogen mass fractions in Li_2NH and Li_3N, the XRD-visible crystalline nitrogen contribution was approximately 3.29 wt.% after 10 min N_2 exposure. This value increased to approximately 4.85 wt.% after

15 min, showing that additional N_2 exposure promoted the formation of crystalline Li-N-containing phases. When the nitridation time was extended further to 30 min, the XRD-visible crystalline nitrogen contribution decreased to approximately 4.25 wt.%. Therefore, prolonged nitridation did not lead to a monotonic increase in the XRD-detectable crystalline nitrogen inventory. Instead, the additional nitrogen fixed during extended N_2 exposure may have been distributed partly in poorly crystalline, interfacial or locally disordered Li-N-H environments, which were not fully captured by XRD.

LiH remained the dominant lithium-containing crystalline phase after nitridation, indicating that only part of the available LiH was converted within the short N_2 exposure time. The formation of Li_2NH and minor Li_3N nevertheless provides phase evidence that LiH participates directly in nitrogen fixation during the first half-cycle of CLAS. The XRD results should therefore be interpreted as evidence for crystalline Li-N phase formation, rather than as a complete quantitative measure of all fixed nitrogen.

Apparent coherent domain size analysis further supports this phase-evolution interpretation. For the 15 min nitrided sample, residual LiH gave an apparent coherent domain size of approximately 45.6 nm, while Li_2NH and Li_3N gave values of approximately 35 nm and 31.4 nm, respectively. Ni domains remained finer, with an apparent coherent domain size of approximately 22.4 nm as estimated from the Ni (200) reflection. These results suggest that nitridation produces nanoscale Li-N crystalline domains within LiH-derived regions, rather than forming large, segregated nitrogen-

rich crystalline particles. The finer Ni domains align with a distributed promoter phase, whereas TiO_2 remains weakly diffracting and is locally retained as a support-derived domain.

In summary, the XRD results demonstrate that exposure to N_2 at 300 ℃ induces a partial transformation from LiH to Li-N phases in 10 wt.% TiO_2-50 wt.% Ni-LiH. The optimal nitridation window corresponds to the formation of Li_2NH-rich phases, whereas prolonged N_2 exposure leads to increased Li_3N formation. This distinction is significant because Li_2NH-rich intermediates are more directly involved in subsequent hydrogenation to NH_3, while excessive Li_3N formation may indicate deeper nitridation that is less advantageous for short-cycle hydride-imide operation.

4.4.2 SEM-EDS mapping of fresh, nitrided and hydrogenated TiO_2-Ni-LiH

To complement the XRD phase analysis, SEM-EDS mapping was used to compare the mesoscale distribution and local spatial association of Ni-, Ti/O- and N-containing regions in TiO_2-Ni-LiH in the fresh, nitrided and hydrogenated states, as shown in **Figure 4.10**.

The fresh sample showed weak and scattered N signal, while Ni and Ti signals were distributed across the mapped particle region. After nitridation, the N signal became more evident within the composite region. This change is consistent with nitrogen incorporation during N_2 exposure, although the N map should be interpreted

qualitatively because nitrogen EDS signals are weak and can be affected by sample geometry, background subtraction and surface contamination.

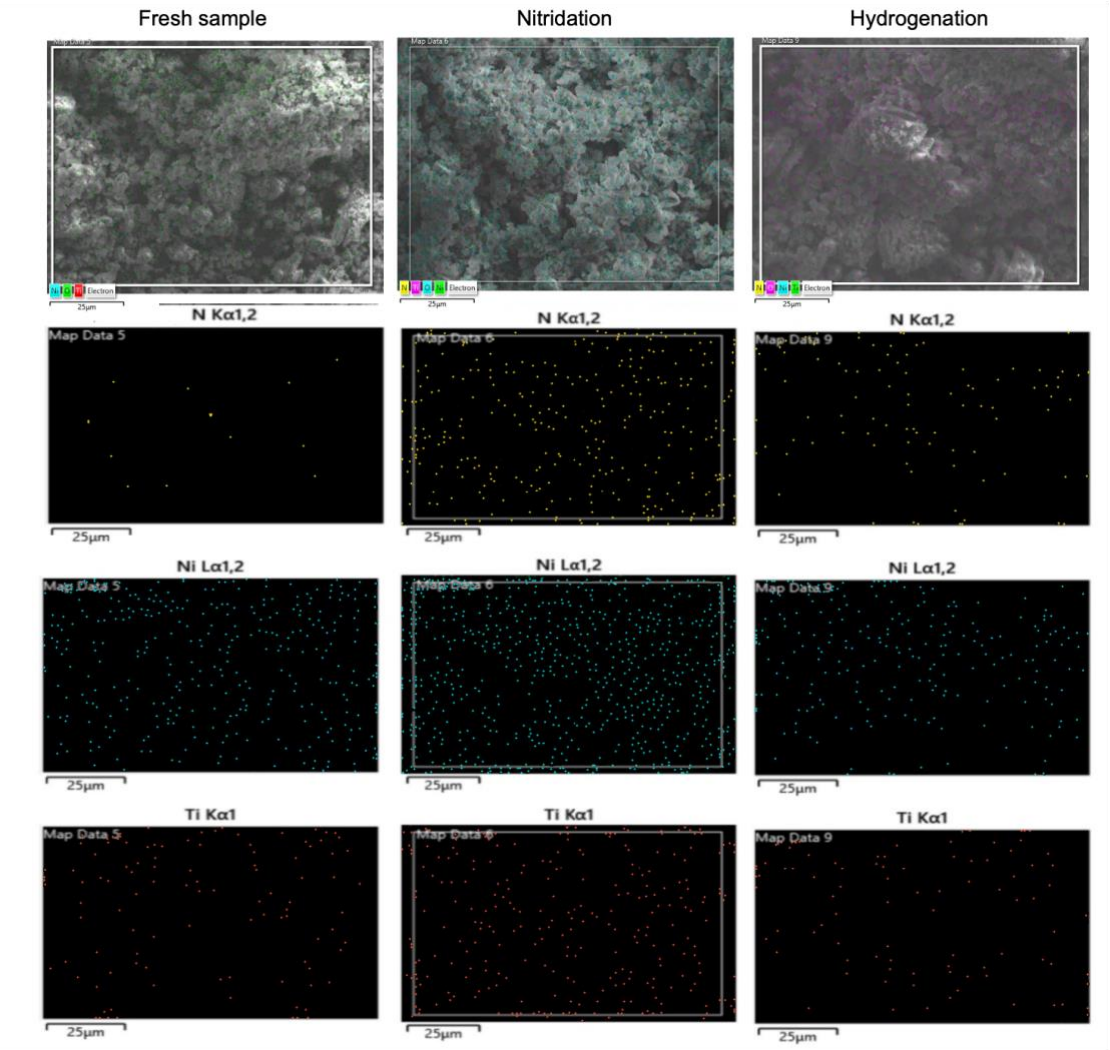


Figure 4.10. SEM-EDS maps of representative fresh, nitrided and hydrogenated TiO2-Ni-LiH samples.

After hydrogenation, the N signal became weaker and less continuous than in the nitrided sample. This trend is consistent with partial removal of nitrogen-containing intermediates during H_2 exposure and NH_3 formation. However, SEM-EDS alone cannot quantify the fixed nitrogen inventory or distinguish Li_2NH, Li_3N and other Li-

N-H environments. The role of SEM-EDS is therefore to provide reaction-state elemental evidence, while phase assignment is based primarily on XRD and ammonia release is confirmed by conductivity-based NH_3 quantification.

The Ni and Ti maps show that the N-containing regions are not completely separated from the promoter and support components. Instead, the nitrided sample contains N signal within a composite region where Ni- and Ti-containing domains are also present. This supports the interpretation that nitridation occurs within a mixed TiO_2-Ni-LiH architecture rather than only within isolated hydride-rich particles. Therefore, the SEM-EDS results provide mesoscale evidence for local spatial association among the support-rich, promoter-rich and N-containing regions within the composite.

4.4.3 TEM-EDS and HRTEM analysis of local structure

TEM, HAADF-STEM and EDS were used to examine the local structure and elemental distribution of 10 wt.% TiO_2-50 wt.% Ni-LiH after 30 min N_2 exposure at 300 ℃. This nitridation condition was selected because the time-dependent NH_3 release results showed that extending the N_2 step from 15 to 30 min increased both the NH_3 release rate and the final NH_3 amount during subsequent hydrogenation.

Figure 4.11 shows the HAADF-STEM image and EDS elemental maps of the nitrided 10 wt.% TiO_2-50 wt.% Ni-LiH composite. The HAADF image shows an agglomerated particle containing many bright nanoscale domains distributed within a lower-contrast matrix. In HAADF-STEM, bright regions are generally associated with heavier-

element-rich or thicker regions. For this composite, the bright domains are therefore attributed mainly to Ni- and Ti-containing regions within the agglomerated particle.

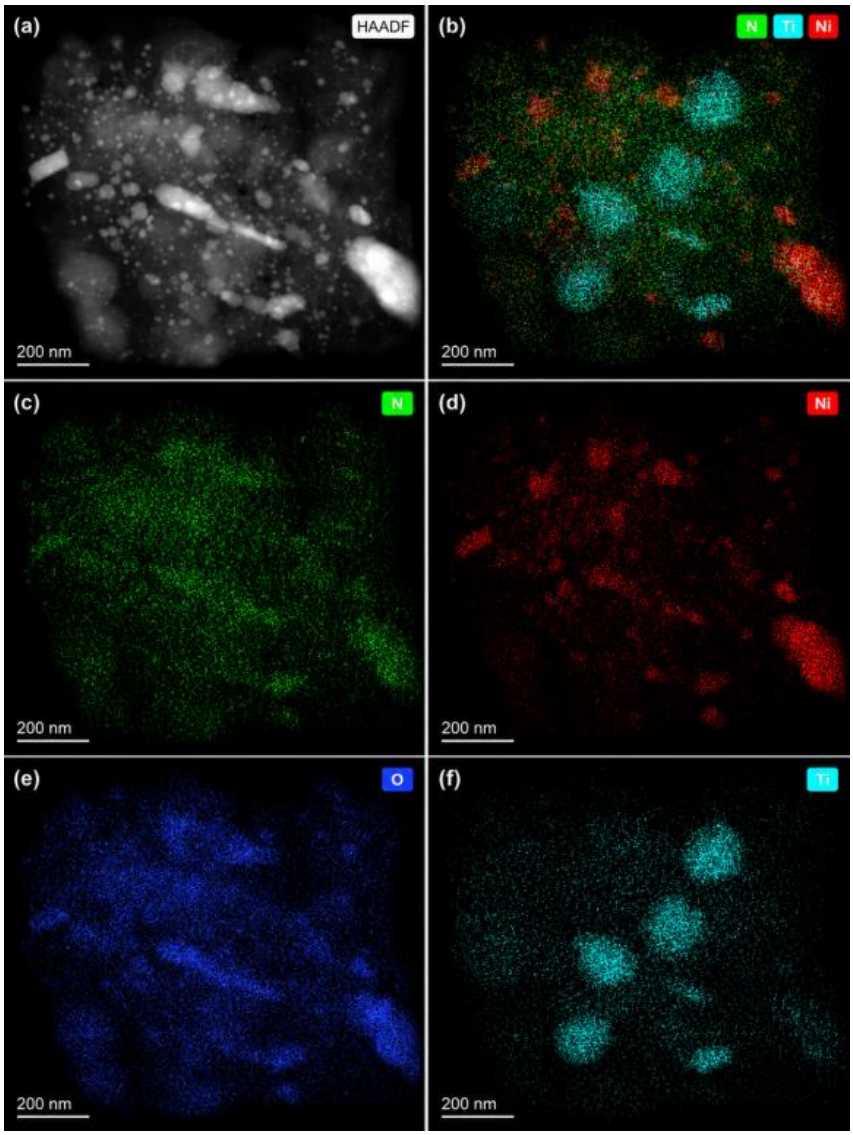


Figure 4.11. HAADF-STEM image and EDS elemental maps of 10 wt.% TiO_2-50 wt.% Ni-LiH after 30 min N_2 exposure at 300 °C.

(a) HAADF-STEM image of the nitrided composite. **(b)** Overlay map of N, Ti and Ni. **(c)** N map. **(d)** Ni map. **(e)** O map. **(f)** Ti map.

The HAADF image shows a high density of bright nanoscale domains distributed within the agglomerated particle. These domains are not isolated as large segregated

particles but are closely distributed within the lower-contrast matrix. Combined with TEM-EDS, this supports the presence of locally enriched Ni- and Ti-containing domains embedded within a LiH-derived reaction particle. The EDS elemental maps show that N, Ni, O and Ti were detected within the same analysed agglomerate. Ni appeared as locally enriched domains, while Ti and O appeared as discrete Ti/O-rich regions assigned to TiO_2-derived support domains. The N signal extended across the agglomerate and partly overlapped with regions containing Ni and Ti/O. Because Li and H cannot be reliably detected by conventional EDS, the assignment of Li_2NH and Li_3N is provided by XRD rather than by EDS. The role of TEM-EDS is therefore to show that N-containing regions form within the same local architecture as the promoter and support domains.

This local arrangement connects directly with the XRD phase evolution. XRD shows that Li_2NH and Li_3N form during nitridation, while HAADF-STEM and TEM-EDS show that Ni-rich and Ti/O-rich domains are distributed within the same nitrided agglomerate. Nitridation therefore appears to proceed through local conversion of LiH-derived regions inside a mixed Ni-LiH-TiO_2 architecture, rather than through complete macroscopic separation of the support, promoter and hydride phases. The relevant structural descriptor is therefore not simply the amount of Ni or TiO_2, but the spatial coupling between Ni-rich promoter domains, TiO_2-derived support domains and Li-N-forming hydride regions.

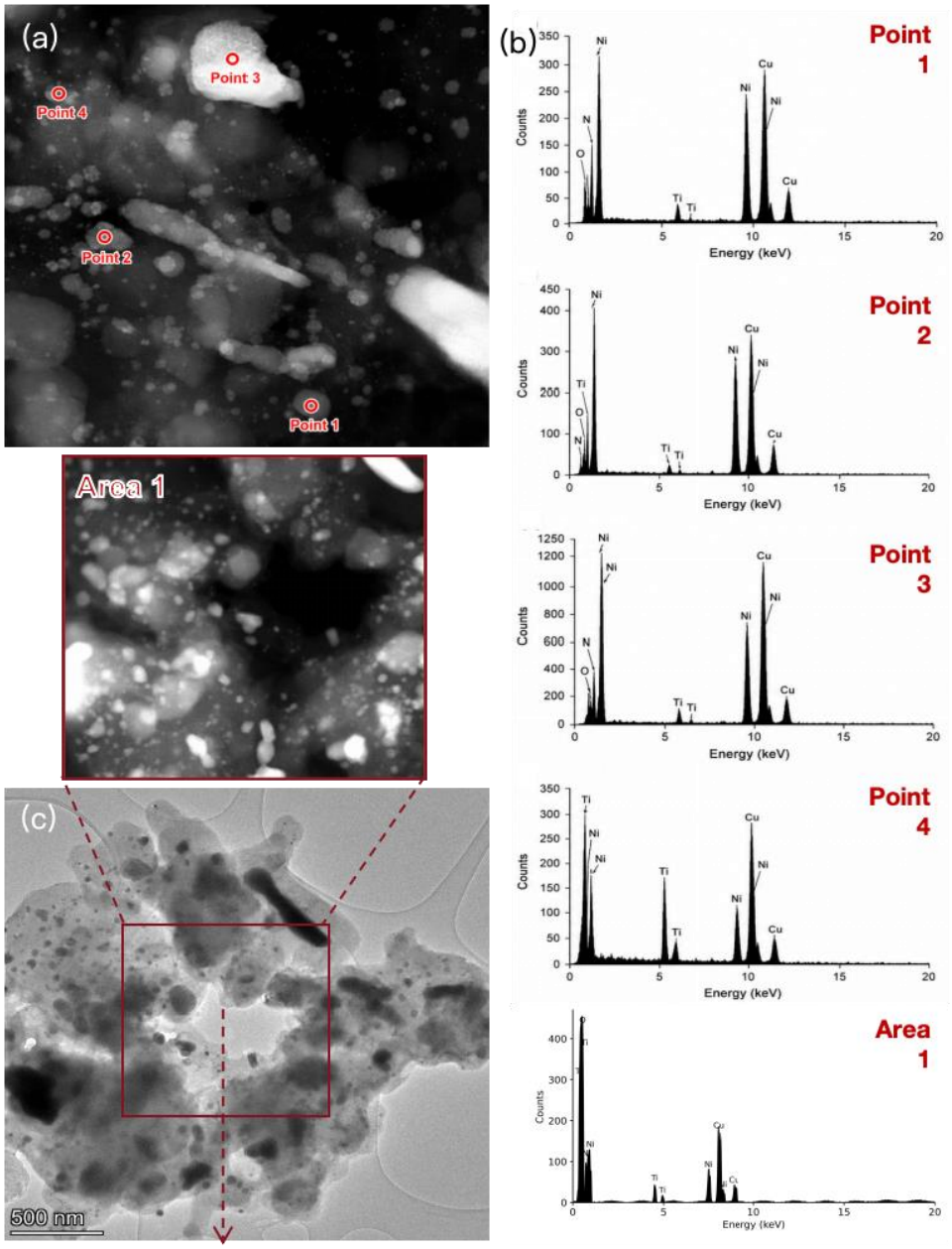


Figure 4.12. Local EDS point analysis of 10 wt.% TiO_2-50 wt.% Ni-LiH after 30 min N_2 exposure at 300 °C.

(a) HAADF-STEM image showing the selected EDS analysis points. **(b)** EDS spectra collected from Points 1-4. **(c)** TEM image showing the selected particle region used for HRTEM analysis

Figure 4.12 shows local EDS point analysis from selected regions of the same nitrided composite. The spectra collected from Points 1-4 show Ni, Ti, O and N signals, with

Cu arising mainly from the TEM grid. The relative intensities varied between the selected points, confirming local compositional heterogeneity within the agglomerated particle. Points with stronger Ni signals correspond to Ni-rich regions, whereas the point with stronger Ti signal indicates a Ti/O-containing region associated with the TiO_2-derived support. This point analysis agrees with the elemental maps in **Figure 4.11** and supports a multi-domain structure in which promoter-rich, support-rich and N-containing regions coexist within the same nitrided agglomerate.

This heterogeneous but spatially coupled distribution is important for the enhanced CLAS performance of the supported composite. The coexistence of N-containing regions, Ni-rich domains and Ti/O-rich support-related regions indicates that TiO_2 addition does not simply dilute the Ni-LiH composite but helps organise the reactive components into a more accessible local structure. Combined with the XRD evidence for Li_2NH and minor Li_3N formation, the EDS maps support the partial conversion of LiH into Li-N-containing species during nitridation. The close spatial association between N, Ni and Ti/O-rich regions is consistent with the higher NH_3 production of TiO_2-supported Ni-LiH, where Ni provides reactive sites for N_2 activation, and TiO_2 improves the dispersion and accessibility of Ni-LiH regions.

Overall, the TEM-EDS results show that nitridation of 10 wt.% TiO_2-50 wt.% Ni-LiH produces a heterogeneous composite structure in which Li-N-containing regions are locally associated with both Ni-rich and TiO_2-derived domains. This local arrangement

provides structural support for the improved performance observed in **Section 4.3** and indicates that the enhanced activity arises from coupled effects of Ni promotion, TiO_2-assisted dispersion and accessible LiH/Li-N reaction domains.

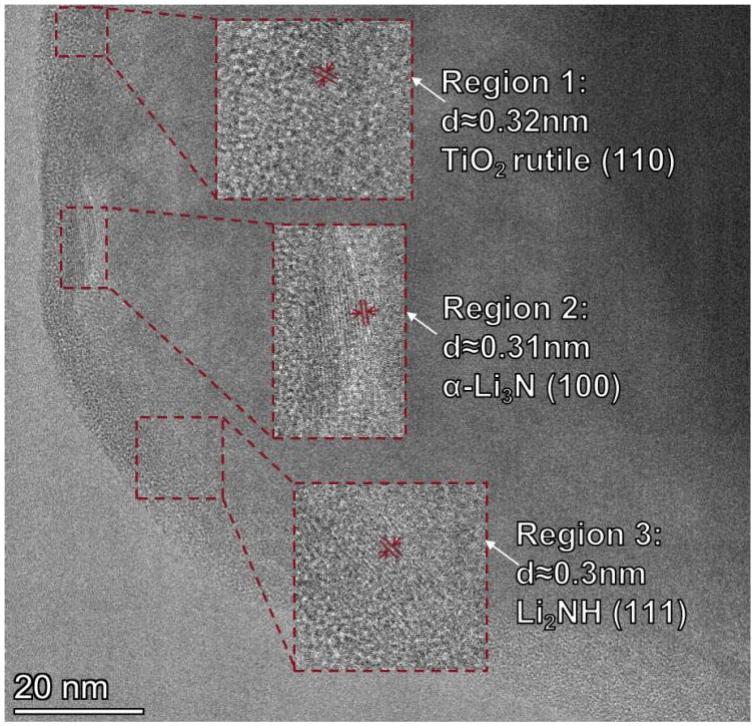


Figure 4.13. HRTEM lattice-fringe analysis of 10 wt.% TiO_2-50 wt.% Ni-LiH after 30 min N_2 exposure at 300 °C.

HRTEM was further used to examine crystalline domains in the nitrided composite. **Figure 4.13** shows representative lattice-fringe regions and their assigned spacings. Region 1 showed a lattice spacing of approximately 0.32 nm, which is consistent with rutile TiO_2 (110)-related domains. Region 2 showed a spacing of approximately 0.31 nm, consistent with α-Li_3N (100)-related domains. Region 3 showed a spacing of approximately 0.30 nm, consistent with Li_2NH-related domains. These assignments are

consistent with the XRD results in **Section 4.4.1**, where TiO_2 remained as the support phase and Li_2NH with minor Li_3N was detected after nitridation.

The HRTEM results provide a lattice-level view of the same nitrided architecture. The region with d ≈ 0.32 nm is consistent with rutile TiO_2 (110), indicating that locally ordered TiO_2-derived domains remain after N_2 exposure. The regions with d ≈ 0.31 nm and d ≈ 0.30 nm are consistent with α-Li_3N- and Li_2NH-related domains, respectively. The significance of these assignments is not only crystallographic, but also spatial: TiO_2-related and Li-N-containing lattice domains are observed within the same nitrided particle. This supports the interpretation that LiH-derived regions form Li_2NH-rich intermediates during nitridation and can locally convert further towards Li_3N under extended N_2 exposure.

Overall, TEM-EDS and HRTEM show that 30 min nitridation produces a heterogeneous TiO_2-Ni-LiH composite containing N-containing regions, Ni-rich domains and Ti/O-rich support-related domains. The local lattice-fringe analysis supports the presence of TiO_2-, Li_2NH- and Li_3N-related crystalline domains, although the phase assignments are interpreted together with XRD because several relevant phases can have similar lattice spacings. These observations are consistent with the XRD phase evolution and support the role of TiO_2 in maintaining local association between support-derived domains, Ni-rich promoter regions and LiH-derived Li-N-containing regions during nitridation.

4.4.4 XPS analysis of surface states

XPS was used to analyse the near-surface chemical states of the as-prepared 10 wt.% TiO_2-50 wt.% Ni-LiH composite before nitridation. The purpose of this analysis was to define the surface chemical environment of the supported composite after ball milling and sample transfer. This is complementary to the XRD and TEM-EDS results because XPS probes the outermost surface of the powder rather than the bulk crystalline phase composition.

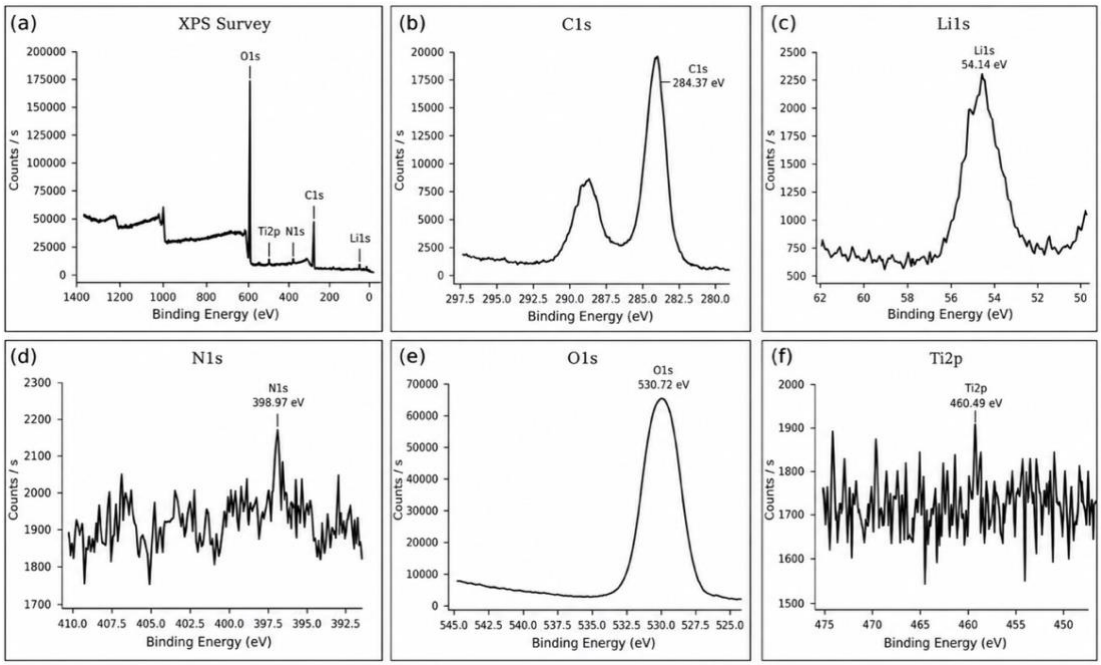


Figure 4.14. XPS analysis of as-prepared 10 wt.% TiO_2-50 wt.% Ni-LiH before nitridation.

(a) XPS survey spectrum and high-resolution spectra of **(b)** C 1s, **(c)** Li 1s, **(d)** N 1s, **(e)** O 1s and **(f)** Ti 2p.

Figure 4.14 shows the XPS survey spectrum and high-resolution spectra of C 1s, Li 1s, N 1s, O 1s and Ti 2p. The survey spectrum shows clear C, Li and O signals, together

with weak N and Ti contributions. No resolved Ni 2p signal was identified from the exported peak table. The surface atomic composition estimated from XPS is summarised in **Table 4.2**. The surface was dominated by Li, O and C, while Ti and N were present only at low surface concentrations.

The Li 1s peak at 54.14 eV indicates a Li-containing surface environment. In this region, LiH, Li_2O, LiOH and lithium carbonate-related species can contribute overlapping signals, so the Li 1s peak is treated as evidence of Li-containing surface species rather than a unique LiH assignment. The C 1s peak at 284.37 eV is assigned mainly to adventitious carbon or carbonaceous surface species introduced during sample transfer and exposure. The O 1s peak at 530.72 eV indicates an oxygen-rich surface. This oxygen signal is attributed to contributions from TiO_2 support domains and lithium-containing oxygenated species, such as Li_2O, LiOH or carbonate-related surface species. The high O content is consistent with partial surface oxidation or hydrolysis of the air- and moisture-sensitive LiH-based composite during handling and transfer. The Ti 2p region showed only a weak feature at 460.49 eV, consistent with 0.22 at.%. This indicates that Ti-containing species were present at the XPS-visible surface, but only weakly exposed. The weak Ti signal is consistent with TiO_2 being locally dispersed within the composite and partly covered by Li/O/C-rich surface species.

Table 4.2. XPS-estimated surface atomic composition of as-prepared 10 wt.% TiO_2-50 wt.% Ni-LiH.

Element (core level)	**Peak Binding Energy (eV)**	**Surface atomic percentage (at.%)**	**Main assignment**	**Interpretation**
C 1s	284.37	30.94	Adventitious carbon / carbonaceous surface species	Surface exposure and transfer contribution
Li 1s	54.14	31.01	Li-containing surface species	Li-rich surface; LiH and oxidised Li species may overlap
N 1s	398.97	0.62	Trace nitrogen-containing surface contribution	Not assigned to nitridation products because the sample was not exposed to N_2
O 1s	530.72	37.21	TiO_2 and Li-O-containing surface species	Oxygen-rich surface from TiO_2 and lithium oxygenated species
Ti 2p	460.49	0.22	TiO_2-derived surface contribution	Weak Ti exposure at the XPS-visible surface
Ni 2p	Not resolved	Not quantified	Ni-containing domains not resolved by XPS	Ni presence supported by formulation and TEM-EDS

A weak N 1s feature was detected at 398.97 eV, consistent with 0.62 at.%. Since this XPS sample was analysed before nitridation, this signal is assigned to a trace nitrogen-containing surface contribution rather than to Li-N nitridation products. The absence of a resolved Ni 2p peak does not conflict with the material composition or the TEM-EDS results. Ni is present in the composite by formulation and was locally detected by TEM-EDS. In XPS, the Ni signal is likely weak because Ni-rich domains are not strongly exposed at the outermost surface or are attenuated by the Li/O/C-rich surface layer.

Overall, XPS shows that the as-prepared 10 wt.% TiO_2-50 wt.% Ni-LiH composite has a Li/O/C-rich outer surface with weak Ti and trace N signals, while Ni was not resolved at the XPS-visible surface. This does not indicate the absence of Ni from the composite, because Ni was introduced by formulation and detected locally by TEM-EDS. Instead, the XPS result indicates that the outermost surface is not a uniform Ni-rich or Ni-coated layer. A more consistent interpretation is that Ni exists as local domains embedded within a Li-rich composite, while the outer surface is influenced by lithium-containing oxygenated species formed during handling and transfer. This surface state should therefore be treated as a boundary condition for interpreting reactivity, rather than as a complete description of the bulk composite structure.

Taken together, the XRD, SEM-EDS, TEM-EDS, HRTEM and XPS results establish a consistent structure-function picture for TiO_2-supported Ni-LiH. TiO_2 modifies the Ni-LiH powder architecture at the micrometre scale, remains as locally distributed Ti/O-

rich support domains after nitridation, and helps maintain spatial association between support-derived regions, Ni-rich promoter domains and LiH-derived nitrogen-containing domains. XRD shows that the useful nitridation window is associated with Li_2NH-rich phase formation, while prolonged N_2 exposure promotes additional Li_3N formation. The microscopy results show that this phase evolution occurs within heterogeneous multi-domain agglomerates rather than through large-scale phase separation. Therefore, the improved performance of TiO_2-Ni-LiH is attributed to a coupled structural and chemical effect: TiO_2 improves the local organisation of the Ni-LiH composite, while N_2 exposure time determines whether the LiH-derived nitrogen inventory remains mainly imide-rich or shifts towards deeper nitridation.

4.5 Fixed-bed operating behaviour of Ni-LiH composites

After identifying Ni as the most effective promoter and TiO_2 as the most effective support, the operating behaviour of the representative Ni-LiH system was examined. These tests were designed to determine how reaction temperature, reaction time, gas flow, repeated cycling and fixed-bed loading affect the measured CLAS performance under ambient pressure. This section therefore connects intrinsic material reactivity with the practical question of how much of the active LiH phase can be utilised in a fixed-bed reactor.

4.5.1 Temperature effects in single- and two-temperature CLAS operation

Reaction temperature is a key operating parameter in LiH-based CLAS because it affects both N_2 fixation and the subsequent hydrogenation of Li-N-H intermediates. In the first set of tests, nitridation and hydrogenation were conducted at the same temperature to identify the general operating window for 50 wt.% Ni-LiH. The tests were performed using 100 mg of sample under ambient pressure, N_2 and H_2 flow rates of 100 mL min^{-1}, and 15 min for each nitridation and hydrogenation step.

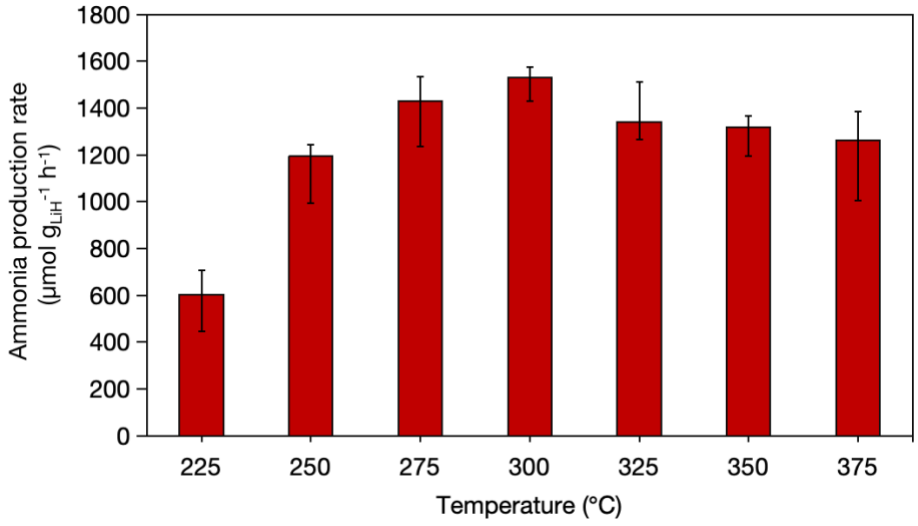


Figure 4.15. Effect of reaction temperature on NH_3 production rate over 50 wt.% Ni-LiH under single-temperature CLAS operation.

Figure 4.15 shows the NH_3 production rate of 50 wt.% Ni-LiH under single-temperature operation. The NH_3 production rate increased as the reaction temperature was raised from 225 ℃ to 300 ℃, indicating that higher temperature promoted the nitridation-hydrogenation sequence within this range. This increase is consistent with enhanced N_2 activation, faster formation of Li-N-H intermediates and more effective hydrogenation of nitrogen-containing species. The highest NH_3 production rate under

single-temperature operation was obtained at 300 °C, reaching 1531 μmol g_{LiH}^{-1} h^{-1}. Further increasing the reaction temperature above 300 °C led to a decrease in NH_3 production, showing that the Ni-LiH system operates within a defined temperature window rather than following a monotonic temperature dependence.

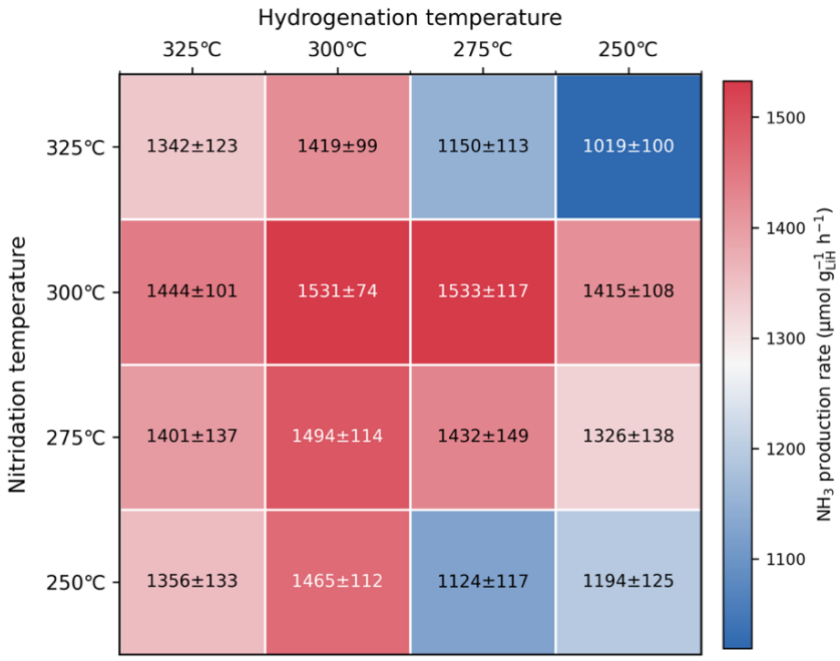


Figure 4.16. NH_3 production over 50 wt.% Ni-LiH under separate temperature control of nitridation and hydrogenation.

The observed temperature maximum reflects the combined thermal requirements of the two CLAS half-cycles. Temperature influences both Ni-assisted N_2 activation and nitrogen transfer during nitridation, as well as the subsequent hydrogenation and NH_3 release of Li-N-H intermediates. The optimum whole-cycle temperature therefore represents a balance between the formation of hydrogenation-accessible nitrogen species and their conversion to NH_3. Because the two steps may have different thermal

requirements, the nitridation and hydrogenation temperatures were subsequently controlled separately to assess their individual contributions to the overall CLAS performance. **Figure 4.16** summarises the NH_3 production rates of 50 wt.% Ni-LiH as a temperature-combination matrix, where the row represents the nitridation temperature and the column represents the hydrogenation temperature.

The temperature-combination matrix shows that NH_3 production was strongly influenced by the nitridation temperature. When nitridation was conducted at 300 ℃, high NH_3 production rates were obtained across the tested hydrogenation temperatures. The highest value, 1533 μmol g_{LiH}^{-1} h^{-1}, was obtained at 300 ℃ nitridation and 275 ℃ hydrogenation, while 300 ℃ nitridation and 300 ℃ hydrogenation gave a nearly identical value of 1531 μmol g_{LiH}^{-1} h^{-1}. This indicates that the best performance lies within a relatively narrow operating window centred around 300 ℃ nitridation and 275-300 ℃ hydrogenation.

By contrast, when the nitridation temperature was increased to 325 ℃, NH_3 production decreased across all hydrogenation temperatures, with values ranging from 1019 to 1419 μmol g_{LiH}^{-1} h^{-1}. Lower nitridation temperatures also gave lower performance than the 300 ℃ nitridation condition. These results indicate that the nitridation step imposes a strong control on the overall CLAS performance of Ni-LiH. The hydrogenation temperature also affected NH_3 production, but its optimum range was broader, with high NH_3 production rates obtained at 275-300 ℃ when nitridation was fixed at 300 ℃.

The close agreement between the best single-temperature result and the best two-temperature result is important. Single-temperature operation at 300 °C gave 1531 μmol g_{LiH}^{-1} h^{-1}, while separate temperature control gave a maximum of 1533 μmol g_{LiH}^{-1} h^{-1}. Therefore, separating the two temperatures did not substantially increase the maximum rate under the present conditions. Instead, it clarified the thermal requirements of the two half-cycles. The data show that 300 °C provides sufficient thermal driving for nitridation while also maintaining favourable conditions for hydrogenation. Lowering the hydrogenation temperature slightly to 275 °C maintained high NH_3 production, whereas increasing the nitridation temperature to 325 °C reduced the performance.

The separate-temperature results show that nitridation temperature primarily controls the quantity of nitrogen-containing intermediates available for the subsequent H_2 step. At insufficient nitridation temperature, slower N_2 activation and nitrogen transfer limit the nitrogen inventory formed within the fixed reaction time, and increasing the hydrogenation temperature cannot fully compensate for this limitation. In contrast, nitridation at approximately 300 °C generates a larger hydrogenation-accessible nitrogen inventory, which can be converted to NH_3 over a broader hydrogenation-temperature range. The hydrogenation temperature therefore mainly controls the rate and completeness of NH_3 release from the nitrogen-containing intermediates formed during the preceding N_2 step.

This behaviour is consistent with the thermodynamic and kinetic characteristics expected for imide-mediated H_2-CLAS [108]. Thermodynamic analyses of metal-imide cycles indicate that hydrogenation of metal imides to produce NH_3 becomes more favourable as temperature decreases, whereas hydride nitridation remains dependent on sufficient kinetic activation. The present results reflect this balance: nitridation required a temperature close to 300 ℃ to generate a substantial hydrogenation-accessible nitrogen inventory, while hydrogenation remained effective over the slightly broader range of 275-300 ℃. Increasing the nitridation temperature to 325 ℃ reduced the subsequent NH_3 production, indicating that higher temperature did not improve the overall formation and utilisation of the reactive nitrogen-containing intermediates. Therefore, the optimum whole-cycle performance near 300 ℃ arises from matching effective N_2 fixation with favourable NH_3-forming hydrogenation.

4.5.2 Effect of nitridation and hydrogenation time

The duration of nitridation and hydrogenation directly determines the nitrogen inventory formed in the solid phase and the extent to which this fixed nitrogen is released as NH_3 during the subsequent H_2 step. In this section, 50 wt.% Ni-LiH was selected as the representative material, and time-dependent tests were conducted at 300 ℃ under atmospheric pressure. The nitridation time was set to either 15 or 30 min, followed by hydrogenation while monitoring the cumulative NH_3 production amount.

Figure 4.17a compares the NH_3 release profiles during hydrogenation after 15 and 30 min of nitridation. After 15 min nitridation, the NH_3 amount reached 37 μmol after 15 min of hydrogenation and increased to 56 μmol after 30 min. This indicates that the 15 min H_2 step released a substantial fraction of the fixed nitrogen, while additional NH_3 was still released during the extended hydrogenation period. The decreasing slope after 15 min suggests that the readily accessible Li-N-H species were converted first, followed by a slower release from less accessible or more slowly hydrogenated regions of the solid bed.

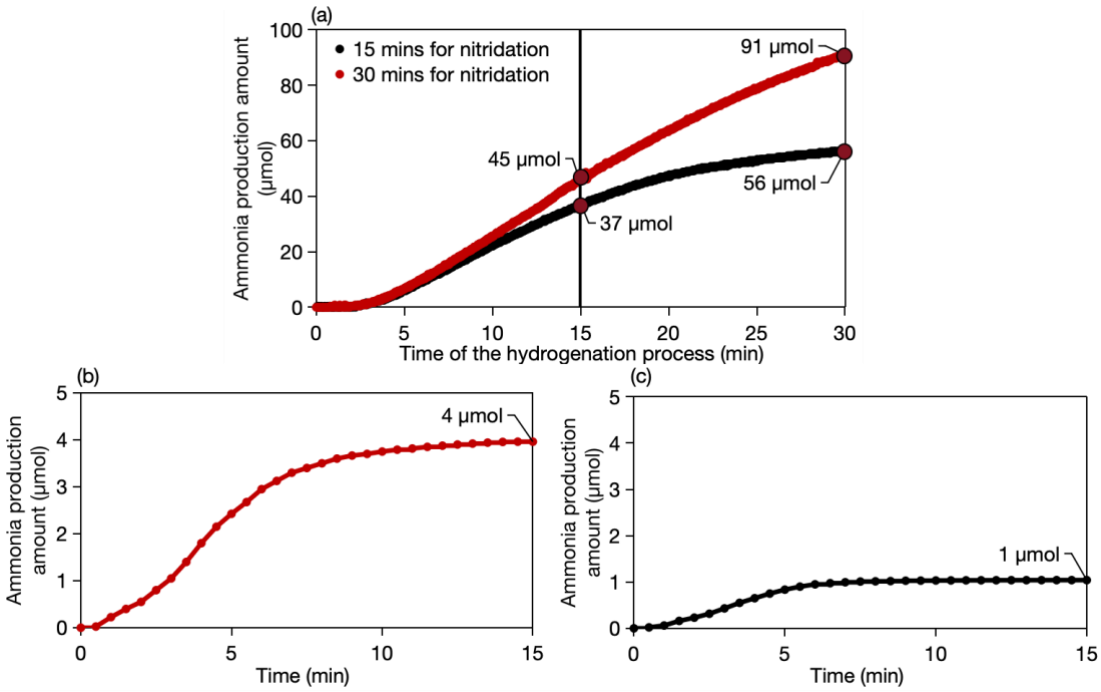


Figure 4.17. Effect of nitridation and hydrogenation time on NH_3 release over 50 wt.% Ni-LiH at 300 ℃.

(a) Cumulative NH_3 production amount during hydrogenation after 15 and 30 min nitridation. **(b)** Residual NH_3 detected during the subsequent N_2 step after 30 min nitridation followed by 30 min hydrogenation. **(c)** Residual NH_3 detected during the subsequent N_2 step after 15 min nitridation followed by 30 min hydrogenation.

Extending the nitridation time from 15 to 30 min increased NH_3 production throughout the subsequent hydrogenation step. After 30 min nitridation, the NH_3 produced reached 45 μmol after 15 min hydrogenation and 91 μmol after 30 min hydrogenation. Compared with the 15 min nitridation case, the larger quantity of NH_3 produced indicates that longer N_2 exposure increased the hydrogenation-accessible nitrogen inventory in the Ni-LiH composite. However, the continued increase between 15 and 30 min hydrogenation also shows that the higher N_2 loading generated during the longer nitridation step was not fully released within the first 15 min of H_2 exposure. This indicates that increasing the nitridation time increases the amount of nitrogen that can be released as NH_3 during the following H_2 step, but also requires a longer hydrogenation period for this nitrogen to be converted and removed as NH_3.

The subsequent N_2 step was used to examine whether residual NH_3 release remained after the 30 min hydrogenation period. **Figure 4.17b** shows the NH_3 detected during the following N_2 step after 30 min nitridation and 30 min hydrogenation. A small but measurable NH_3 amount was still detected, reaching 4 μmol, which indicates that extended nitridation generated a larger quantity of nitrogen-containing species, a small fraction of which was not fully released within the 30 min H_2 period. In contrast, after 15 min nitridation followed by 30 min hydrogenation, the subsequent N_2 step produced only 1 μmol of residual NH_3, as shown in **Figure 4.17c**. Therefore, for the 15 min

nitridation condition, 30 min hydrogenation was sufficient to release almost all of the hydrogenation-accessible nitrogen species formed during the N_2 step.

These results show that nitridation and hydrogenation times are coupled operating parameters. Extending the nitridation step increases the N_2 loading of the solid carrier and can increase the single-cycle NH_3 yield, but the additional nitrogen must also be converted and released during the following H_2 step. A 15 min nitridation step followed by 30 min hydrogenation resulted in almost complete NH_3 release under the tested conditions, whereas 30 min nitridation produced a larger NH_3 amount but still gave a small residual release during the following N_2 step. Therefore, the optimum CLAS cycle should balance N_2 uptake, hydrogenation conversion, NH_3 removal and total cycle duration. This balance could be further quantified by mathematical modelling of the nitridation and hydrogenation steps, using time, flow rate, pressure and temperature as optimisation variables to maximise NH_3 productivity.

4.5.3 Effect of gas flow rate

The gas flow rate was varied to assess the impact of mass transfer on the CLAS performance of 50 wt.% Ni-LiH. Both nitridation (N_2) and hydrogenation (H_2) steps used identical flow rates of 50, 100, 150, or 300 mL min^{-1}. Reaction temperature, sample mass, and reaction time remained constant.

Figure 4.18 shows the cumulative NH_3 production during hydrogenation at various gas flow rates. After 15 minutes, NH_3 output increased from 14 μmol at 50 mL min^{-1} to

approximately 35, 46, and 88 μmol at 100, 150, and 300 mL min^{-1}, respectively. Higher flow rates also resulted in steeper release profiles, especially after the initial stage of hydrogenation.

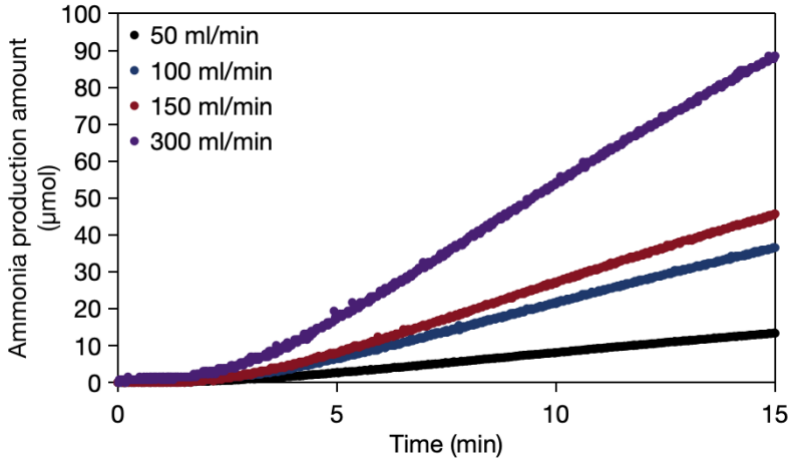


Figure 4.18. Effect of gas flow on NH_3 production amount over 50 wt.% Ni-LiH. The same flow rate was used for the N_2 nitridation step and the H_2 hydrogenation step.

The dependence on flow rate indicates that NH_3 output is influenced by both gas transport and the intrinsic chemistry of Ni-LiH. Increased N_2 flow enhances gas-solid contact during nitridation, while higher H_2 flow improves hydrogen delivery and facilitates NH_3 removal from the reactor. At lower flow rates, slower gas exchange and product removal can limit NH_3 production within the set reaction time.

At flow rates of 50, 100, 150 and 300 mL min^{-1}, the apparent N_2 utilisation values were approximately 0.023%, 0.029%, 0.025% and 0.024%, respectively, while the corresponding apparent H_2 utilisation values were approximately 0.069%, 0.086%, 0.075% and 0.072%. These low values show that both N_2 and H_2 were supplied in large excess under the present screening conditions. Therefore, the increase in NH_3

production at higher flow rate is mainly attributed to improved gas delivery and product removal rather than high single-pass gas conversion.

The results show that gas flow rate is an important operating parameter in the fixed-bed CLAS system. A material with high intrinsic reactivity may still show a low apparent rate if gas access to the active regions is restricted. Conversely, improved powder dispersion or support-assisted morphology may increase the apparent rate by increasing the fraction of LiH that is contacted by N_2 and H_2 within the fixed reaction time. Therefore, flow-rate effects support the broader conclusion that LiH-based CLAS is governed by material-reactor coupling. For material comparison, the flow rate must be fixed so that transport effects are not mistaken for differences in intrinsic activity.

4.5.4 Cycling behaviour of Ni-LiH composites

The cycling stability of 50 wt.% Ni-LiH was evaluated under repeated CLAS operation at 300 ℃ and atmospheric pressure. Each cycle consisted of 15 min nitridation followed by 15 min hydrogenation, with both N_2 and H_2 supplied at 100 mL min^{-1}. The NH_3 production amount was recorded for each cycle to assess the activation behaviour and short-term stability of the Ni-promoted LiH composite.

Figure 4.19a shows the NH_3 production amount over 12 consecutive cycles. The first cycle produced a lower NH_3 amount of approximately 28 μmol, whereas the second cycle increased to 34 μmol. From the second cycle onward, the NH_3 production amount

remained within a relatively narrow range, mostly between approximately 34 and 37 μmol.

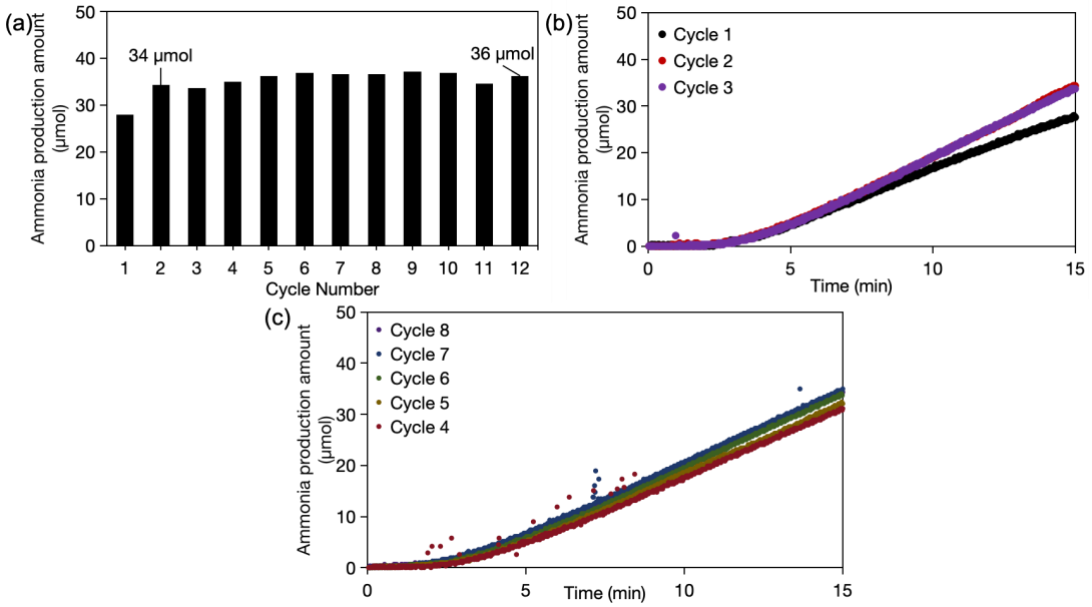


Figure 4.19. Cycling stability of 50 wt.% Ni-LiH under standard CLAS operation. **(a)** NH_3 production amount over 12 consecutive cycles. **(b)** Cumulative NH_3 production profiles during hydrogenation for the first three cycles, showing the activation behaviour. **(c)** Cumulative NH_3 production profiles of representative activated cycles.

The twelfth cycle produced 36 μmol, showing that the material retained stable NH_3 production after the initial cycle. The lower first-cycle output indicates a start-up behaviour during the early nitridation-hydrogenation process, which may include both material activation and a delayed NH_3 transport or hold-up effect in the reactor and downstream absorption system. From the material side, this behaviour may be associated with the formation of reactive Ni-LiH interfacial regions, initial conversion of LiH into Li-N-H intermediates and restructuring of surface species during the first

cycle. From the system side, a small amount of NH_3 may also remain temporarily in the reactor volume, outlet line or absorption pathway before being fully swept into the acid trap. After this initial start-up period, subsequent cycles showed more reproducible NH_3 production, suggesting that both the material state and gas-transfer/collection behaviour became more stable under repeated operation.

Figure 4.19b shows the cumulative NH_3 production profiles during hydrogenation for the first three cycles. Cycle 1 showed a lower cumulative NH_3 amount throughout the hydrogenation step, whereas Cycles 2 and 3 reached higher and closely overlapping final amounts. This agrees with the cycle-by-cycle production data in **Figure 4.19a**, where the main increase in activity occurred between the first and second cycles. After activation, the cumulative NH_3 production profiles became more reproducible. **Figure 4.19c** compares representative activated cycles within the 15 min hydrogenation period. The profiles show similar accumulation behaviour, with only minor differences in the final NH_3 amount. This indicates that the activated 50 wt.% Ni-LiH composite maintained stable hydrogenation behaviour over repeated CLAS cycles.

To further examine whether the performance enhancement from TiO_2 addition could be maintained during repeated operation, the cycling behaviour of the TiO_2-supported Ni-LiH composite was compared with that of unsupported Ni-LiH over ten consecutive CLAS cycles, as shown in **Figure 4.20**. Under the same cycling conditions, 10 wt.% TiO_2-50 wt.% Ni-LiH consistently showed higher NH_3 production rates than

unsupported Ni-LiH throughout the tested cycles. The unsupported Ni-LiH sample remained mostly in the range of approximately 1400-1600 μmol g_{LiH}^{-1} h^{-1}, whereas the TiO_2-supported composite maintained rates close to 1900-2000 μmol g_{LiH}^{-1} h^{-1} for most cycles. This indicates that the improvement caused by TiO_2 addition was not limited to a single optimised test but was retained during repeated nitridation-hydrogenation operation. In contrast, unsupported Ni-LiH showed lower rates, which is consistent with the SEM observation that Ni-LiH retains compact agglomerated regions that may restrict gas access to internal hydride domains.

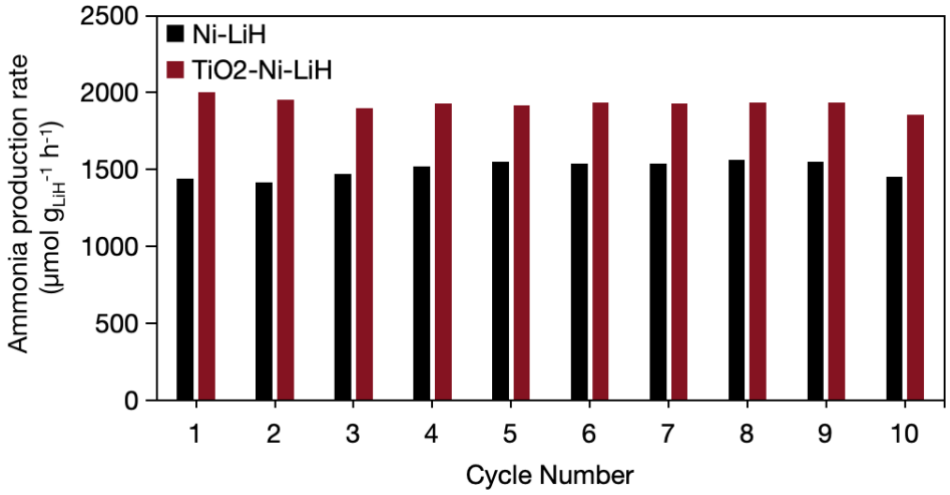


Figure 4.20. Cycling comparison of unsupported Ni-LiH and TiO_2-Ni-LiH composites under repeated CLAS operation after activation.

Overall, the cycling results show that 50 wt.% Ni-LiH undergoes an initial activation cycle before reaching a stable operating state. The comparison with TiO_2-Ni-LiH further shows that support-assisted structural modification maintains a higher NH_3 production rate during short-term cycling. This supports the interpretation that TiO_2

improves the effective utilisation of LiH by modifying particle morphology and gas-solid access. Nevertheless, longer-term cycling is still required to assess whether the supported structure remains stable over extended operation.

4.5.5 Effect of fixed-bed loading

After confirming the cycling stability of 50 wt.% Ni-LiH under the standard 0.1 g loading condition, the effect of fixed-bed loading was examined by varying the amount of material placed in the reactor. This experiment was used to assess whether increasing the quantity of Ni-LiH in the fixed-bed led to proportional utilisation of the material. The tested sample masses were 0.05, 0.1, 0.2, 0.5 and 1.0 g.

Figure 4.21a shows the temperature-dependent NH_3 production rates for different fixed-bed loadings. The lowest loading of 0.05 g gave the highest rate across most of the temperature range, reaching more than 2067 μmol g_{LiH}^{-1} h^{-1} at 325-350 ℃. The 0.1 g sample also showed high activity, with the maximum rate obtained around 300 ℃. However, when the sample loading increased to 0.2, 0.5 and 1.0 g, the measured rate decreased substantially across the whole temperature range. The 0.5 and 1.0 g samples showed much lower rates than the lower-loading cases, even though the same material composition was used.

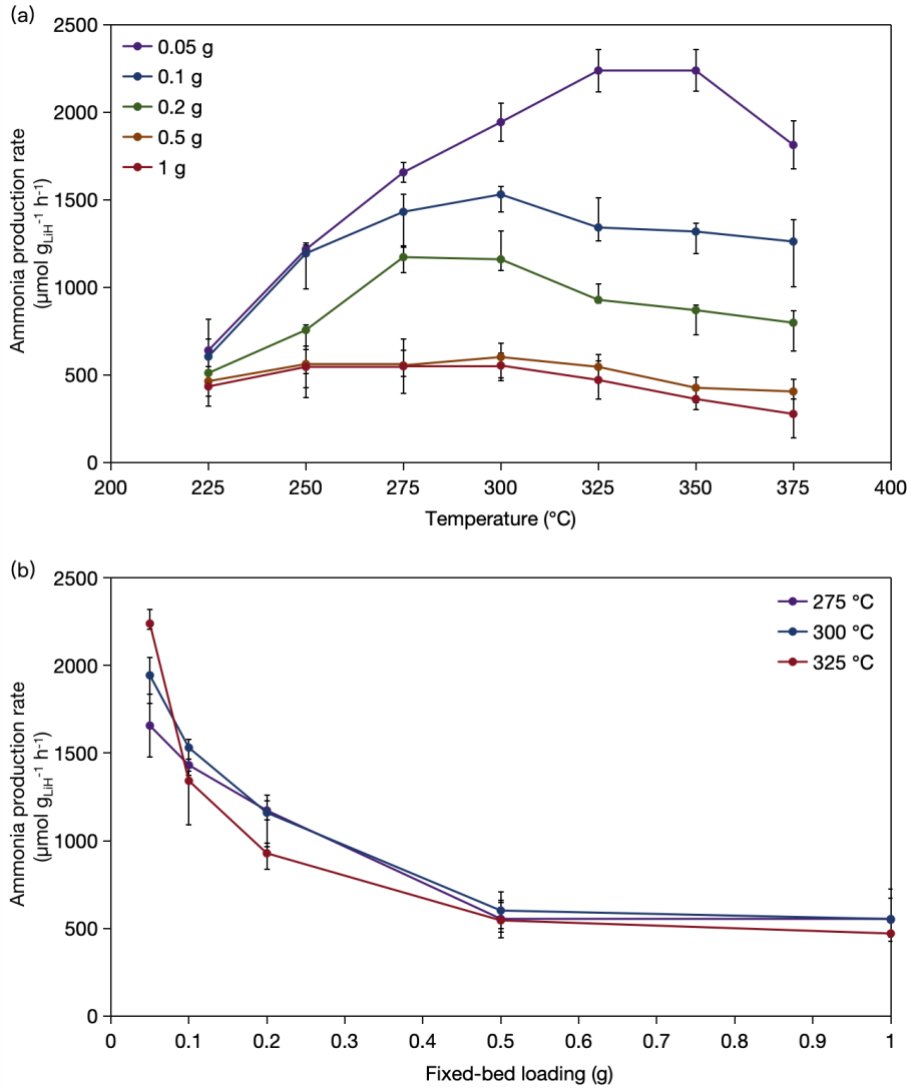


Figure 4.21. Effect of fixed-bed loading on the NH_3 production rate of 50 wt.% Ni-LiH.

(a) temperature-dependent performance at different loadings, **(b)** loading-dependent performance at selected temperatures.

To show the loading dependence more clearly, the rates at 275, 300 and 325 °C are replotted as a function of fixed-bed loading in **Figure 4.21b**. At all three temperatures, the ammonia production rate decreased sharply as the loading increased from 0.05 to 0.5 g. The change became smaller between 0.5 and 1.0 g, indicating that the system

approached a utilisation-limited regime at higher loadings. This behaviour shows that the additional material introduced at higher loading was not proportionally involved in the nitridation-hydrogenation cycle within the fixed reaction time.

This loading effect provides direct evidence that the apparent CLAS performance depends strongly on effective material utilisation in the fixed bed. At low loading, the powder bed is thinner, and gas can contact a larger fraction of the Ni-LiH particles during both N_2 exposure and H_2 exposure. This gives higher NH_3 production rates. At higher loading, the powder region becomes denser and thicker within a similar reactor configuration. Denser packing reduces interparticle void space and limits uniform gas penetration through the bed. At increased loading, the powder region becomes thicker and more densely packed within the same reactor configuration. This reduces effective bed porosity, decreases interparticle void space, and increases the diffusion distance required for N_2 and H_2 to access internal regions of the bed. Non-uniform packing or partial bed compaction can also result in suboptimal gas distribution or the formation of preferential flow pathways, which may leave certain Ni-LiH regions insufficiently contacted during the fixed reaction period. As a result, part of the Ni-LiH material is not effectively contacted by N_2 during nitridation or by H_2 during hydrogenation within the selected reaction time. The lower apparent activity at higher loading therefore reflects reduced effective utilisation of the packed powder rather than a change in the intrinsic chemistry of Ni-LiH.

The loading effect is also consistent with the flow-rate dependence discussed in **Section 4.5.3**. Higher gas flow increased the measured NH_3 output, indicating that gas delivery and NH_3 removal influence both the apparent CLAS performance and the apparent single-pass gas utilisation. In this chemical looping system, the apparent N_2 and H_2 utilisation can be estimated from the amount of NH_3 produced relative to the amount of gas supplied during each half-cycle. However, because N_2 and H_2 were supplied in large excess, these values mainly reflect gas-solid contacting and NH_3 removal efficiency rather than true reactant-limited conversion. The temperature dependence also changed with sample loading. For 0.05 g, the highest rate occurred at 325-350 ℃, whereas 0.1 g showed its maximum around 300 ℃. Larger loadings exhibited lower rates and weaker temperature responsiveness. This suggests that increasing temperature alone cannot fully compensate for the transport and utilisation limitations introduced by larger fixed-beds. At higher loading, only part of the material may participate effectively within the fixed nitridation-hydrogenation window, so the NH_3 production rate expressed per gram of LiH decreases even though more material is present in the reactor.

The temperature dependence further supports this observation. For the 0.05 g sample, increasing temperature enhanced the rate up to 325-350 ℃. At larger loadings, the peak became weaker or shifted, and high-temperature performance declined more strongly. This suggests that higher temperature can promote the intrinsic nitridation-hydrogenation chemistry, but it can also intensify packing-related limitations, particle

agglomeration or local restructuring in denser powder beds. Therefore, the optimum temperature depends not only on the reaction chemistry of Ni-LiH, but also on how effectively the packed bed maintains gas access and interfacial contact during cycling.

These results show that fixed-bed loading is a key reactor parameter for LiH-based CLAS. While increasing material quantity raises the nitrogen-carrier inventory, excessive loading leads to incomplete utilisation due to bed densification. In the current reactor setup, lower loadings achieved better gas-solid contact and higher reaction rates, whereas loadings reduced gas penetration and decreased the fraction of reactive material effectively involved in each cycle. This phenomenon is directly relevant to reactor scale-up, as increasing the material inventory does not yield a proportional increase in ammonia output unless bed porosity, gas distribution, and transport pathways are preserved. Consequently, a loading of 0.1 g was selected as the standard sample loading for comparative tests to minimize fixed-bed transport effects and to provide a consistent basis for evaluating material performance.

4.6 Summary

The results in this chapter show that LiH-based CLAS performance depends on both chemical and structural factors. Pure LiH exhibited limited activity under current low-pressure cycling, while transition metal promotion significantly increased NH_3 production. Among the promoters tested, Ni delivered the highest activity. This

suggests that optimal performance requires not just the presence of a transition metal, but effective contact between the promoter and LiH.

The promoter-loading results confirm this interpretation. Low Ni loading results in insufficient Ni-LiH contact, while high Ni loading reduces LiH utilisation, likely due to disrupted hydride accessibility or formation of metal-rich domains. The optimum at 50 wt.% Ni reflects a balance between Ni-assisted N_2 activation and LiH-mediated nitrogen storage and hydrogenation. Similar non-monotonic behaviour for Co-LiH suggests this balance is a general feature of metal-promoted hydride composites, with Ni providing the most effective promoter-hydride coupling among those tested.

Adding supports further influences the structure-performance relationship. Among the tested supports, TiO_2 provided the most consistent improvement. TiO_2-supported Ni-LiH composites produced higher NH_3 yields across a broader temperature range than unsupported Ni-LiH. However, the effect was not monotonic: 10-15 wt.% TiO_2 improved performance, while higher amounts offered no additional benefit. This indicates that TiO_2 enhances performance by improving dispersion and accessibility without separating Ni and LiH from productive contact.

The structural characterisation supports this interpretation. SEM showed that TiO_2 addition produced a more fragmented and granular morphology than unsupported Ni-LiH, suggesting improved gas-solid accessibility. XRD showed that N_2 exposure partially converted LiH into Li-N-containing phases, mainly Li_2NH with minor Li_3N in

selected nitrided samples. TEM-EDS showed that N-containing regions were locally associated with Ni-rich and Ti/O-rich domains after nitridation. HRTEM further showed lattice spacings consistent with TiO_2-, Li_2NH- and Li_3N-related crystalline domains. Together, these results indicate that nitridation occurs within a heterogeneous composite structure in which Ni, TiO_2-derived domains and LiH/Li-N-containing regions are spatially coupled.

The reactor studies show that this local structure of catalysts must also remain accessible to the reactants under fixed-bed operation. Temperature, reaction time, gas flow rate and bed loading all affected the measured NH_3 output. Longer nitridation increased the hydrogenation-accessible nitrogen inventory but also increased the hydrogenation demand. Higher gas flow improved the apparent NH_3 release, showing that gas delivery and product removal influence the measured rate. Increasing fixed-bed loading decreased the NH_3 production rate, demonstrating that dense powder packing reduces effective material utilisation. Therefore, high intrinsic reactivity is not sufficient for practical CLAS performance; the powder bed must maintain gas pathways and accessible reactive interfaces.

The overall working model is therefore as follows. Ni provides the main promotion for N_2 activation. LiH acts as the nitrogen carrier through Li-N-H intermediates. TiO_2 improves the spatial distribution and accessibility of Ni-LiH regions, increasing the fraction of LiH that participates effectively in the nitridation-hydrogenation cycle. The

improved performance of TiO_2-supported Ni-LiH is therefore attributed to coupled effects of promoter chemistry, support-assisted structural modification and fixed-bed gas-solid transport.

This interpretation remains a structure-performance correlation rather than a fully resolved reaction mechanism. XRD provides phase evidence for crystalline Li-N-containing products, but it does not quantify disordered or interfacial nitrogen species. TEM-EDS supports spatial association between Ni-, Ti/O- and N-containing regions, but Li and H cannot be directly mapped by conventional EDS. XPS provides information on the as-prepared surface state, but not on the surface after nitridation and hydrogenation. Therefore, isotope labelling, operando XRD, air-free post-reaction XPS and quantitative kinetic analysis would be required to confirm the detailed nitrogen-transfer pathway.

Overall, the results show that effective LiH-based CLAS requires more than selecting an active promoter. The composite must maintain productive Ni-LiH contact, sufficient LiH inventory, support-assisted structural accessibility and favourable gas-solid transport during repeated nitridation-hydrogenation cycling. This provides the structure-engineering basis for further development of supported hydride-imide nitrogen carriers for low-pressure ammonia synthesis.

5. Conclusions and Outlook

This thesis investigated transition-metal-promoted and supported LiH-based composites for low-pressure chemical looping ammonia synthesis. The work focused on three linked questions: whether transition metal promotion can improve the reactivity of LiH, how operating parameters influence ammonia production in a fixed-bed CLAS reactor, and whether support-assisted structural modification can further enhance the effective utilisation of LiH-based nitrogen carriers.

The results show that LiH-based CLAS performance is controlled by both chemical and structural factors. Transition metal promotion improves nitrogen activation, while support addition modifies particle morphology, local component distribution and gas-solid accessibility. Among the systems examined, TiO_2-supported Ni-LiH showed the most favourable combination of activity, operating-temperature range and structural characteristics. The findings provide a material-level basis for further development of supported hydride-imide nitrogen carriers for low-pressure ammonia synthesis.

5.1 Main conclusions

The main conclusions of this thesis are summarised as follows.

1. **An ambient-pressure fixed-bed CLAS platform was established for LiH-based nitrogen carriers.**

This thesis demonstrates that LiH-based hydride-imide CLAS can be operated in an ambient-pressure fixed-bed reactor under alternating N_2 and H_2 flow. The reactor, gas-

switching, temperature-calibration, acid-absorption and conductivity-quantification procedures provided a consistent platform for comparing nitrogen carriers under defined cycling conditions.

2. Transition-metal promotion is required to make LiH an effective low-pressure CLAS carrier.

Pure LiH produced only limited NH_3 under the present conditions, whereas transition-metal-promoted LiH composites gave substantially higher rates. Among Ni, Co, Mn and Fe, Ni produced the strongest enhancement. The optimum composition was 50 wt.% Ni-LiH, reaching approximately 1531 μmol NH_3 g_{LiH}^{-1} h^{-1} at 300 ℃. This shows that LiH-based CLAS performance is controlled by a promoter-hydride balance: sufficient Ni is required for N_2 activation, while sufficient LiH-containing regions must remain available for nitrogen storage and hydrogenation.

3. TiO_2 support provided the main structure-engineering improvement.

Among the supports examined, TiO_2 gave the clearest enhancement over unsupported Ni-LiH and broadened the effective operating window. The optimum TiO_2 range was 10-15 wt.%, with 15 wt.% TiO_2 giving the highest NH_3 production rate of approximately 2050 μmol NH_3 g_{LiH}^{-1} $h^{-}1$ at 300 ℃. The non-monotonic dependence on TiO_2 loading shows that the support effect is not caused by simple dilution or increasing support content alone. Instead, moderate TiO_2 addition improves the effective use of

the Ni-LiH active fraction, while excessive support can weaken promoter-hydride contact.

4. Structural characterisation supports a TiO_2-assisted hydride-imide reaction framework.

XRD showed that N_2 exposure partially converted LiH into Li-N-containing crystalline phases, mainly Li_2NH with minor Li_3N in selected nitrided samples, supporting the hydride-imide CLAS pathway. SEM showed that TiO_2 changed compact Ni-LiH agglomerates into a more fragmented granular morphology. TEM-EDS and HRTEM indicated that N-containing regions, Ni-rich domains and Ti/O-rich regions were present within the same local composite structure after nitridation. XPS showed a Li/O/C-rich outer surface, confirming that the outermost surface of these air- and moisture-sensitive powders differs from the nominal bulk formulation. Overall, TiO_2 improves particle dispersion in the Ni-LiH composite and promotes better gas-solid contact during cycling, helping Ni and LiH-derived Li-N-H phases remain available for the nitridation-hydrogenation sequence.

5. Reactor operation and fixed-bed utilisation strongly affect the measured CLAS performance.

The reactor studies show that the measured CLAS performance is strongly affected by temperature, gas flow, reaction time and powder-bed loading. A reaction temperature around 300 °C gave the best compromise between nitridation and hydrogenation, while

separate temperature control did not substantially improve the maximum rate. Longer nitridation increased the amount of nitrogen that could be released as NH_3 during the following H_2 step but also required a longer hydrogenation period. Higher gas flow increased NH_3 production by improving gas supply and product removal. Increasing the material amount from thin-bed conditions to larger beds reduced the LiH-normalised rate because the additional powder was not proportionally contacted by N_2 and H_2. Therefore, future CLAS optimisation should consider cycle time, flow rate, pressure, bed geometry and material loading together, rather than treating carrier activity as an isolated material property.

Overall, this work establishes a structure-engineered LiH-based carrier design principle for low-pressure CLAS. Effective performance requires a matched combination of Ni-assisted N_2 activation, LiH-based hydride-imide nitrogen storage, TiO_2-assisted powder structuring and fixed-bed gas-solid transport. The TiO_2-Ni-LiH system therefore provides a practical model for developing supported hydride-imide nitrogen carriers, while also showing that scale-up will require both material optimisation and reactor-bed design.

5.2 Scope and limitations

This study investigated transition-metal-promoted and supported LiH-based composites for low-pressure chemical looping ammonia synthesis. The work established the effects of promoter identity, promoter loading, reaction temperature,

reaction time, gas flow rate, fixed-bed loading and support addition on ammonia production. It also examined phase evolution and local structure using XRD, SEM, TEM-EDS, HRTEM and XPS. The results provide a material-level understanding of how Ni promotion and TiO_2-assisted structural modification improve the effective utilisation of LiH-based nitrogen carriers. However, the scope of these findings should be clearly defined.

First, ammonia quantification in this work was based on acid absorption followed by conductivity measurement. This method allowed consistent comparison between samples under the same reactor and absorption conditions, and was suitable for identifying trends in promoter identity, support addition and operating parameters. However, conductivity-based quantification remains an indirect method. The present work did not include independent validation using ion chromatography, indophenol blue analysis, nuclear magnetic resonance or mass spectrometry [39]. In addition, isotope experiments using $^{15}N_2$ were not performed [20]. Therefore, although the observed NH_3 production trends are internally consistent and supported by XRD evidence of Li-N phase formation, future studies should include independent NH_3 quantification and isotope labelling to exclude potential contributions from trace contamination and confirm the nitrogen source.

Second, the XRD analysis provided the main evidence for LiH-to-Li-N phase transformation during nitridation, but the phase fractions should be treated as semi-

quantitative. LiH, Li_2NH, Li_3N and related Li-N-H species are air- and moisture-sensitive, and some nitrogen-containing species may be poorly crystalline, disordered or located at interfacial regions. This is particularly important because the XRD-estimated crystalline Li-N fraction did not increase monotonically from 15 to 30 min nitridation, whereas the subsequent hydrogenation data showed higher NH_3 release after 30 min N_2 exposure. This indicates that crystalline phase quantification alone does not fully describe the hydrogenation-accessible nitrogen inventory. XRD should therefore be interpreted together with NH_3 release behaviour and microscopy-based evidence.

Third, TEM-EDS and HRTEM provided local information on elemental distribution and crystalline domains, but these techniques probe selected regions rather than the full powder bed. The TEM-EDS results showed that N-containing regions were spatially associated with Ni-rich and Ti/O-rich domains after nitridation, supporting the proposed heterogeneous Ni-LiH-TiO_2 structure. However, conventional EDS cannot reliably detect Li or H, and N mapping is qualitative rather than fully quantitative. HRTEM lattice fringes require caution because several phases exhibit similar interplanar spacings. Therefore, TEM-EDS and HRTEM were employed to support local structural interpretation, while phase identification of LiH, Li_2NH, and Li_3N relied primarily on XRD.

Fourth, XPS was performed on the as-prepared TiO_2-Ni-LiH composite before nitridation. It therefore describes the initial near-surface chemical state rather than the surface state after N_2/H_2 cycling. The XPS results showed a Li/O/C-rich outer surface, weak Ti signal and no resolved Ni 2p signal. This does not contradict the nominal composition or TEM-EDS observation of Ni and Ti-containing domains; instead, it shows that the outermost surface of the powder differs from the bulk/local particle structure. Because LiH-based materials are highly sensitive to oxygen and moisture, the XPS-visible surface is likely influenced by lithium-containing oxygenated species formed during sample handling and transfer. Post-reaction, air-free XPS would be required to directly follow surface evolution during CLAS.

Fifth, the present reactor experiments were conducted in a lab-scale fixed-bed configuration. The loading study showed that increasing the quantity of Ni-LiH in the reactor did not lead to proportional material utilisation. Higher powder loadings gave lower NH_3 production rates per gram of LiH, indicating that gas penetration, bed packing and access to internal LiH-containing regions become limiting under denser fixed-bed conditions. Therefore, the activity measured using small powder loadings should not be directly extrapolated to larger-scale beds without considering reactor geometry, gas distribution, heat transfer and mechanical stability of the composite.

The porosity, pore volume, and pore-size distribution of the LiH-based composites were not measured in this study. These properties can influence gas transport, accessible

reactive surface area, and the interaction between N_2 or H_2 and internal carrier regions during gas-solid cycling. The SEM observations provide qualitative insights into particle morphology and agglomeration, but do not quantify internal porosity or pore connectivity. Therefore, the improved performance of TiO_2-supported Ni-LiH cannot be attributed to changes in specific surface area or pore structure. Porosity characterisation is technically challenging for these materials because LiH and the resulting Li-N-H phases are highly reactive with moisture and oxygen, and exposure during sample transfer or degassing may alter the original pore structure and surface composition.

Finally, although TiO_2 was identified as the most effective support in this study, the detailed chemical role of TiO_2 was not fully investigated. The results support a structural role, including improved particle dispersion, reduced agglomeration and stronger spatial coupling between Ni-, Ti/O- and N-containing regions. However, whether TiO_2 also contributes through defect chemistry, Ti^{3+}/Ti^{4+} redox behaviour, oxygen vacancies or electronic metal-support interaction remains unresolved [133]. This distinction is important because TiO_2-related literature shows that defective TiO_{2-x} can affect metal dispersion and interfacial electronic structure, but those effects require dedicated characterisation beyond the scope of the present work.

5.3 Future research

Future work should first strengthen ammonia quantification and nitrogen-source validation. Conductivity-based NH_3 measurement should be cross-checked using an independent analytical method such as ion chromatography, indophenol blue colorimetry, nuclear magnetic resonance or online mass spectrometry. More importantly, $^{15}N_2$ isotope experiments should be performed under representative CLAS conditions to confirm that the detected NH_3 originates from N_2 fixation rather than background nitrogen or trace contamination. This is essential for establishing the reliability of LiH-based CLAS performance data.

Long-term cycling of TiO_2-supported Ni-LiH should be prioritised. The present study demonstrated stable cycling behaviour for 50 wt.% Ni-LiH after activation, but the optimised TiO_2-supported composite was not subjected to extended cycling. Since support addition changes particle morphology, local distribution and surface chemistry, the long-term stability of TiO_2-Ni-LiH needs to be tested over tens to hundreds of nitridation-hydrogenation cycles. Post-cycling XRD, SEM, TEM-EDS and XPS should be used to determine whether performance loss arises from LiH consumption, Li_2O formation, Ni agglomeration, TiO_2 restructuring, loss of Ni-LiH contact or changes in the packed-bed structure.

Further support optimisation is also required. This work identified TiO_2 as the most effective support among the tested materials, but the influence of TiO_2 polymorph and defect chemistry remains unresolved. Future studies should compare rutile, anatase and

mixed-phase TiO_2, as well as pre-reduced or defect-engineered TiO_{2-x}. These samples should be characterised using O 1s/Ti 2p XPS, electron paramagnetic resonance (EPR), Raman spectroscopy and possibly ultraviolet-visible (UV-vis) diffuse reflectance to determine whether oxygen vacancies or Ti^{3+} species contribute to improved Ni-LiH performance. Such work would clarify whether TiO_2 acts only as a structural modifier or whether it also provides an electronically active oxide-hydride-metal interface.

The promoter-support interface should be studied more systematically. In the present work, Ni was identified as the most effective transition metal promoter and TiO_2 as the most effective support, but the structure of the Ni-LiH-TiO_2 interface was not directly controlled. Future material preparation should vary the order of mixing, milling energy, milling time and support particle size to determine how these parameters affect Ni dispersion, LiH accessibility and TiO_2-Ni contact. Alternative loading strategies, including wet impregnation, deposition-precipitation and pre-reduction of Ni precursors on TiO_2, should also be explored because such methods can generate more controlled metal-support interfaces than direct powder mixing. Pre-depositing Ni onto TiO_2 before mixing with LiH, or preparing TiO_2-supported Ni nanoparticles followed by controlled LiH incorporation, may therefore provide better-defined interfaces for separating the effects of Ni dispersion, TiO_2 support chemistry and LiH accessibility [23, 124].

Composite structure should be improved to overcome fixed-bed utilisation limitations. The sample-loading study showed that dense powder packing reduces the effective utilisation of Ni-LiH. Future work should therefore move beyond loose powders and explore structured forms such as porous pellets, granulated composites, supported beds, inert scaffold dilution or mechanically stable monolith-like structures. The goal should be to maintain close Ni-LiH contact while preserving open gas pathways for repeated N_2 and H_2 access. This is especially important for scale-up, because a material with high intrinsic activity can still perform poorly if the reactor bed restricts gas-solid contact.

Future work should include quantitative characterisation of specific surface area, pore volume, and pore-size distribution using air-free sample handling. Nitrogen or argon adsorption-desorption measurements can determine Brunauer Emmett teller (BET) surface area and pore-size distributions, while complementary techniques such as mercury intrusion porosimetry or X-ray computed tomography can assess larger pores and interconnected void structures. Samples must be transferred from the glovebox in sealed holders and degassed under controlled conditions to minimize oxidation, hydrolysis, or hydride decomposition. Comparative analysis of LiH, Ni-LiH, and TiO_2-Ni-LiH before and after cycling will clarify the effects of support addition and reaction cycling on pore structure and gas-solid accessibility. Operando and in situ characterisation would provide stronger mechanistic insight into the nitridation-

hydrogenation sequence. In situ XRD under alternating N_2 and H_2 would allow direct observation of LiH, Li_2NH, Li_3N and Li_2O evolution during cycling. Thermogravimetric analysis (TGA) coupled with mass spectrometry could quantify N_2 uptake and NH_3 release in real time. Temperature-programmed nitridation and hydrogenation experiments could separate kinetic effects from fixed-bed transport limitations. Air-free or quasi-in situ XPS would be useful for tracking surface chemistry after nitridation and after hydrogenation, while electron energy-loss spectroscopy (EELS) could provide more reliable light-element information than conventional EDS.

The reaction mechanism should also be examined through isotope and transient experiments. $^{15}N_2$ nitridation followed by H_2 hydrogenation would determine whether ammonia formation proceeds from lattice or interfacial nitrogen incorporated during the N_2 step. Switching experiments using $^{14}N_2/^{15}N_2$ could help distinguish nitrogen activation, nitrogen transfer and hydrogenation steps. These experiments would allow the proposed sequence of Ni-assisted N_2 activation, nitrogen transfer to LiH and hydrogenation of Li-N-containing intermediates to be tested more directly [23].

Future studies should compare TiO_2-supported Ni-LiH with other reducible and non-reducible oxide supports. The present results showed that SiO_2 and diatomaceous earth were less effective, while TiO_2 gave the largest enhancement. This indicates that support chemistry, rather than physical dispersion alone, is an important factor in determining CLAS performance. Supports such as CeO_2, Al_2O_3, MgO and selected

perovskite oxides should be investigated to determine how reducibility, oxygen-vacancy formation, acid-base properties and metal-support interactions influence CLAS performance. Such comparisons would help place TiO_2-Ni-LiH within a broader support-design framework for hydride-imide nitrogen carriers [23, 131, 133, 134].

Finally, reactor-level studies are needed to connect material activity with practical CLAS operation. The present work was conducted at atmospheric pressure, so the effect of operating pressure remains to be quantified. Future experiments should therefore examine how N_2 pressure affects nitrogen fixation, and how H_2 pressure affects hydrogenation, NH_3 release and product removal. These pressure effects should be studied together with reaction temperature, nitridation time, hydrogenation time, gas flow rate, purge duration, carrier loading and bed geometry, because these variables are strongly coupled and may produce non-linear interactions within a fixed-bed CLAS cycle.

The heat-map analyses conducted in this study yield valuable insights into pairwise interactions among operating variables; however, they do not comprehensively address the behavior of the entire multivariable system. Consequently, future reactor optimization efforts should progress beyond empirical and pairwise parameter screening by implementing an integrated multivariable framework. A mechanistic reactor model should integrate nitridation and hydrogenation kinetics, gas residence time, operating pressure, gas flow rate, heat and mass transfer, carrier loading, bed

porosity, and bed geometry. This model would provide a basis for describing the combined effects of material reactivity, gas-solid transport, and fixed-bed structure on the complete CLAS cycle.

The mechanistic model could be combined with machine-learning-assisted surrogate modelling to analyse larger, multi-dimensional operating spaces at reduced computational and experimental cost [135]. Experimental data and validated model outputs could be used to train surrogate models that relate operating variables to NH_3 productivity, gas utilisation, cycle time, and material utilisation. These models could then be coupled with global optimisation methods, such as Genetic Algorithms, to identify favourable operating regions across temperature, pressure, gas flow rate, nitridation and hydrogenation duration, purge time, carrier loading, and bed geometry [136, 137].

Since high NH_3 productivity, high gas utilisation, short cycle time, and practical reactor operation are unlikely to be achieved simultaneously, future optimisation should employ a multi-objective framework. Instead of identifying a single optimum based solely on NH_3 production rate, the analysis should determine Pareto-optimal operating conditions that balance productivity, gas utilisation, cycle duration, operating pressure, carrier inventory, and reactor-bed accessibility [138]. Monte Carlo-based sensitivity and uncertainty analysis can be applied to identify the most influential variables, quantify the effects of experimental and model uncertainty, and assess the robustness

of the predicted operating window [139]. This framework would also clarify whether performance losses at higher loading are primarily attributable to intrinsic kinetics, gas penetration, NH_3 removal, heat transfer, or bed-packing limitations.

Once material stability and reactor utilisation have been improved, preliminary techno-economic and energy analyses should be carried out using experimentally validated operating parameters. These analyses should include carrier lifetime, LiH utilisation, replacement frequency, operating pressure, gas-flow demand, cycle time, reactor size and heat-management requirements. This would provide a more realistic assessment of whether supported LiH-based CLAS can be developed into a low-pressure and modular ammonia synthesis route.

Overall, the next stage of this work should shift from material screening to mechanism validation, pressure-dependent reactor optimisation, mathematical modelling and long-term stability testing. The most important question is no longer whether Ni and TiO_2 can improve LiH-based CLAS performance, but how the Ni-LiH-TiO_2 material and the fixed-bed reactor should be co-optimised to maximise NH_3 productivity under scalable operating conditions.

Data availability statement

Data supporting the findings of this thesis will be retained in accordance with the University of Oxford research data management policy. The processed data underlying the figures and tables are available from the author and supervisors upon reasonable request.

References

1. Dresselhaus, M.S. and I.L. Thomas, *Alternative energy technologies.* Nature, 2001. **414**(6861): p. 332-337.
2. Chatterjee, S., R.K. Parsapur, and K.W. Huang, *Limitations of Ammonia as a Hydrogen Energy Carrier for the Transportation Sector.* ACS Energy Letters, 2021. **6**(12): p. 4390-4394.
3. Bockris, J.O., *Will lack of energy lead to the demise of high-technology countries in this century?* International Journal of Hydrogen Energy, 2007. **32**(2): p. 153-158.
4. Züttel, A., et al., *Hydrogen: the future energy carrier.* Philosophical Transactions of the Royal Society a-Mathematical Physical and Engineering Sciences, 2010. **368**(1923): p. 3329-3342.
5. Lan, R., J.T.S. Irvine, and S.W. Tao, *Ammonia and related chemicals as potential indirect hydrogen storage materials.* International Journal of Hydrogen Energy, 2012. **37**(2): p. 1482-1494.
6. Kusoglu, A., *(Re)Defining Clean Hydrogen: From Colors to Emissions.* Electrochemical Society Interface, 2022. **31**(4): p. 47-51.
7. Kouchaki-Penchah, H., et al., *The role of hydrogen in a net-zero emission economy under alternative policy scenarios.* International Journal of Hydrogen Energy, 2024. **49**: p. 173-187.
8. Petitpas, G., *Simulation of boil-off losses during transfer at a LH_2 based hydrogen refueling station.* International Journal of Hydrogen Energy, 2018. **43**(46): p. 21451-21463.
9. Wijayanta, A.T., et al., *Liquid hydrogen, methylcyclohexane, and ammonia as potential hydrogen storage: Comparison review.* International Journal of Hydrogen Energy, 2019. **44**(29): p. 15026-15044.
10. Zheng, J., et al., *Current research progress and perspectives on liquid hydrogen rich molecules in sustainable hydrogen storage.* Energy Storage Materials, 2021. **35**: p. 695-722.
11. Lamb, K.E., M.D. Dolan, and D.F. Kennedy, *Ammonia for hydrogen storage; A review of catalytic ammonia decomposition and hydrogen separation and purification.* International Journal of Hydrogen Energy, 2019. **44**(7): p. 3580-3593.
12. Wan, Z.J., et al., *Ammonia as an effective hydrogen carrier and a clean fuel for solid oxide fuel cells.* Energy Conversion and Management, 2021. **228**.
13. Makepeace, J.W., et al., *Reversible ammonia-based and liquid organic hydrogen carriers for high-density hydrogen storage: Recent progress.* International Journal of Hydrogen Energy, 2019. **44**(15): p. 7746-7767.

14. Smith, C. and L. Torrente-Murciano, *Cost efficiency versus energy utilization in green ammonia production from intermittent renewable energy.* Nature Chemical Engineering, 2025. **2**(4): p. 261-272.
15. Portarapillo, M., et al., *Ammonia as a Hydrogen Carrier: Energetic Assessment of Processes Integrated with Fuel Cells for Power Generation.* Energy & Fuels, 2025. **39**(5): p. 2843-2853.
16. Chen, J.G., et al., *Beyond fossil fuel-driven nitrogen transformations.* Science, 2018. **360**(6391).
17. Juangsa, F.B., A.R. Irhamna, and M. Aziz, *Production of ammonia as potential hydrogen carrier: Review on thermochemical and electrochemical processes.* International Journal of Hydrogen Energy, 2021. **46**(27): p. 14455-14477.
18. Wang, M., et al., *Can sustainable ammonia synthesis pathways compete with fossil-fuel based Haber-Bosch processes?* Energy & Environmental Science, 2021. **14**(5): p. 2535-2548.
19. Smith, C., A.K. Hill, and L. Torrente-Murciano, *Current and future role of Haber-Bosch ammonia in a carbon-free energy landscape.* Energy & Environmental Science, 2020. **13**(2): p. 331-344.
20. Zhang, X.H., et al., *Towards green and efficient chemical looping ammonia synthesis: design principles and advanced redox catalysts.* Energy & Environmental Science, 2024. **17**(7): p. 2381-2405.
21. Guo, H.Z., et al., *Chemical looping based Low-pressure ammonia synthesis.* Chemical Engineering Journal, 2024. **500**.
22. Chen, P., et al., *Interaction of hydrogen with metal nitrides and imides.* Nature, 2002. **420**(6913): p. 302-304.
23. Gao, W.B., et al., *Production of ammonia via a chemical looping process based on metal imides as nitrogen carriers.* Nature Energy, 2018. **3**(12): p. 1067-1075.
24. Wang, P.K., et al., *The Formation of Surface Lithium–Iron Ternary Hydride and its Function on Catalytic Ammonia Synthesis at Low Temperatures.* Angewandte Chemie-International Edition, 2017. **56**(30): p. 8716-8720.
25. Feng, S., et al., *A multi-functional composite nitrogen carrier for ammonia production via a chemical looping route.* Journal of Materials Chemistry A, 2021. **9**(2): p. 1039-1047.
26. Kojima, Y. and M. Yamaguchi, *Ammonia as a hydrogen energy carrier.* International Journal of Hydrogen Energy, 2022. **47**(54): p. 22832-22839.
27. Spatolisano, E. and L.A. Pellegrini, *Haber-Bosch process intensification: A first step towards small-scale distributed ammonia production.* Chemical Engineering Research & Design, 2023. **195**: p. 651-661.

28. Osorio-Tejada, J., N.N. Tran, and V. Hessel, *Techno-environmental assessment of small-scale Haber-Bosch and plasma-assisted ammonia supply chains.* Science of the Total Environment, 2022. **826**.
29. Huang, P.W. and M.C. Hatzell, *Prospects and good experimental practices for photocatalytic ammonia synthesis.* Nature Communications, 2022. **13**(1).
30. Li, J.Y., et al., *Recent Advances in Ammonia Synthesis: From Haber-Bosch Process to External Field Driven Strategies.* Chemsuschem, 2024. **17**(15).
31. Wang, X.S., et al., *A techno-economic study of photovoltaic-solid oxide electrolysis cell coupled magnesium hydride-based hydrogen storage and transportation toward large-scale applications of green hydrogen.* Energy & Environmental Science, 2024. **17**(22): p. 8429-8456.
32. Salehabadi, A., et al., *Emerging perovskite-based catalysts for sustainable and green ammonia production: A promising hydrogen energy carrier.* International Journal of Hydrogen Energy, 2025. **106**: p. 243-260.
33. Wang, X.S., et al., *Challenges and opportunities in hydrogen storage and transportation: A comprehensive review.* Renewable & Sustainable Energy Reviews, 2025. **219**.
34. Osman, O., S. Sgouridis, and A. Sleptchenko, *Scaling the production of renewable ammonia: A techno-economic optimization applied in regions with high insolation.* Journal of Cleaner Production, 2020. **271**.
35. Tian, F.Y., et al., *Innovative progress of thermal ammonia synthesis under mild conditions.* International Journal of Hydrogen Energy, 2024. **78**: p. 92-122.
36. Liu, H.Z., *Ammonia synthesis catalyst 100 years: Practice, enlightenment and challenge.* Chinese Journal of Catalysis, 2014. **35**(10): p. 1619-1640.
37. Gharahshiran, V.S. and Y. Zheng, *Sustainable ammonia synthesis: An in-depth review of non-thermal plasma technologies.* Journal of Energy Chemistry, 2024. **96**: p. 1-38.
38. Guerra, C.F., et al., *Technical-economic analysis for a green ammonia production plant in Chile and its subsequent transport to Japan.* Renewable Energy, 2020. **157**: p. 404-414.
39. Wang, Q.R., J.P. Guo, and P. Chen, *Recent progress towards mild-condition ammonia synthesis.* Journal of Energy Chemistry, 2019. **36**: p. 25-36.
40. Bai, Y.K., et al., *Hydrogen-Assisted Dissociation of N_2: Prevalence and Consequences for Ammonia Synthesis on Supported Ru Catalysts.* ACS Catalysis, 2025. **15**(3): p. 1455-1466.
41. Kammert, J., et al., *Nature of Reactive Hydrogen for Ammonia Synthesis over a Ru/C12A7 Electride Catalyst.* Journal of the American Chemical Society, 2020. **142**(16): p. 7655-7667.

42. Kitano, M., et al., *Electride support boosts nitrogen dissociation over ruthenium catalyst and shifts the bottleneck in ammonia synthesis.* Nature Communications, 2015. **6**.
43. Malmali, M., et al., *Ammonia Synthesis at Reduced Pressure via Reactive Separation.* Industrial & Engineering Chemistry Research, 2016. **55**(33): p. 8922-8932.
44. Smith, C. and L. Torrente-Murciano, *Guidance for targeted development of ammonia synthesis catalysts from a holistic process approach.* Chem Catalysis, 2021. **1**(6): p. 1163-1172.
45. Smith, C. and L. Torrente-Murciano, *Exceeding Single-Pass Equilibrium with Integrated Absorption Separation for Ammonia Synthesis Using Renewable Energy-Redefining the Haber-Bosch Loop.* Advanced Energy Materials, 2021. **11**(13).
46. Smith, C., A.V. McCormick, and E.L. Cussler, *Optimizing the Conditions for Ammonia Production Using Absorption.* ACS Sustainable Chemistry & Engineering, 2019. **7**(4): p. 4019-4029.
47. Jiang, M.H., et al., *Effective N_2 activation strategies for electrochemical ammonia synthesis.* Chem, 2025. **11**(4).
48. Yang, X., et al., *Mechanistic Insights into Electrochemical Nitrogen Reduction Reaction on Vanadium Nitride Nanoparticles.* Journal of the American Chemical Society, 2018. **140**(41): p. 13387-13391.
49. Mukherjee, S., et al., *Metal-organic framework-derived nitrogen-doped highly disordered carbon for electrochemical ammonia synthesis using N_2 and H_2O in alkaline electrolytes.* Nano Energy, 2018. **48**: p. 217-226.
50. Xue, X.L., et al., *Review on photocatalytic and electrocatalytic artificial nitrogen fixation for ammonia synthesis at mild conditions: Advances, challenges and perspectives.* Nano Research, 2019. **12**(6): p. 1229-1249.
51. Zhang, R., et al., *High-Efficiency Electrosynthesis of Ammonia with High Selectivity under Ambient Conditions Enabled by VN Nanosheet Array.* ACS Sustainable Chemistry & Engineering, 2018. **6**(8): p. 9545-9549.
52. Chen, H.Y., et al., *Sulfur dots-graphene nanohybrid: a metal-free electrocatalyst for efficient N_2-to-NH_3 fixation under ambient conditions.* Chemical Communications, 2019. **55**(21): p. 3152-3155.
53. Tao, H.C., et al., *Nitrogen Fixation by Ru Single-Atom Electrocatalytic Reduction.* Chem, 2019. **5**(1): p. 204-214.
54. Liu, T.C., M.R. Gau, and N.C. Tomson, *Mimicking the Constrained Geometry of a Nitrogen-Fixation Intermediate.* Journal of the American Chemical Society, 2020. **142**(18): p. 8142-8146.
55. Erdosy, D.P., et al., *Microporous water with high gas solubilities.* Nature, 2022. **608**(7924): p. 712-+.

56. Koh, C.S.L., et al., *Turning Water from a Hindrance to the Promotor of Preferential Electrochemical Nitrogen Reduction.* Chemistry of Materials, 2020. **32**(4): p. 1674-1683.
57. Shen, H.D., et al., *Electrochemical ammonia synthesis: Mechanistic understanding and catalyst design.* Chem, 2021. **7**(7): p. 1708-1754.
58. McPherson, I. and J. Zhang, *Can Electrification of Ammonia Synthesis Decrease Its Carbon Footprint?* Joule, 2020. **4**(1): p. 12-14.
59. Han, Q., et al., *Progress and challenges in photocatalytic ammonia synthesis.* Materials Advances, 2021. **2**(2).
60. Zhang, S., et al., *Photocatalytic ammonia synthesis: Recent progress and future.* Energychem, 2019. **1**(2).
61. Chen, X. and S.S. Mao, *Titanium dioxide nanomaterials: Synthesis, properties, modifications, and applications.* Chemical Reviews, 2007. **107**(7): p. 2891-2959.
62. Zhang, Q., et al., *Preparation of g-C_3N_4/ZnMoCdS hybrid heterojunction catalyst with outstanding nitrogen photofixation performance under visible light via hydrothermal post-treatment.* Dalton Transactions, 2016. **45**(8): p. 3497-3505.
63. Zhao, Y.X., et al., *Tuning Oxygen Vacancies in Ultrathin TiO_2 Nanosheets to Boost Photocatalytic Nitrogen Fixation up to 700 nm.* Advanced Materials, 2019. **31**(16).
64. Hirakawa, H., et al., *Photocatalytic Conversion of Nitrogen to Ammonia with Water on Surface Oxygen Vacancies of Titanium Dioxide.* Journal of the American Chemical Society, 2017. **139**(31): p. 10929-10936.
65. Vesali-Kermani, E., et al., *Nitrogen photofixation ability of g-C_3N_4 nanosheets/Bi_2MoO_6 heterojunction photocatalyst under visible-light illumination.* Journal of Colloid and Interface Science, 2020. **563**: p. 81-91.
66. Zhang, J., et al., *Non-thermal plasma-assisted ammonia production: A review.* Energy Conversion and Management, 2023. **293**.
67. Peng, P., et al., *A review on the non-thermal plasma-assisted ammonia synthesis technologies.* Journal of Cleaner Production, 2018. **177**: p. 597-609.
68. Sun, J., et al., *A hybrid plasma electrocatalytic process for sustainable ammonia production.* Energy & Environmental Science, 2021. **14**(2): p. 865-872.
69. Rouwenhorst, K.H.R., et al., *Plasma-driven catalysis: green ammonia synthesis with intermittent electricity.* Green Chemistry, 2020. **22**(19): p. 6258-6287.
70. Wang, H.Q., et al., *A novel hybrid Bi_2MoO_6-MnO_2 catalysts with the superior plasma induced pseudo photocatalytic-catalytic performance for ethyl acetate degradation.* Applied Catalysis B-Environmental, 2019. **254**: p. 339-350.

71. Lamichhane, P., et al., *Sustainable nitrogen fixation from synergistic effect of photo-electrochemical water splitting and atmospheric pressure N_2 plasma.* Plasma Sources Science & Technology, 2020. **29**(4).
72. Lai, Q.H., et al., *Chemical looping based ammonia production-A promising pathway for production of the noncarbon fuel.* Science Bulletin, 2022. **67**(20): p. 2124-2138.
73. Ye, T.N., et al., *Contribution of Nitrogen Vacancies to Ammonia Synthesis over Metal Nitride Catalysts.* Journal of the American Chemical Society, 2020. **142**(33): p. 14374-14383.
74. Guo, J.P. and P. Chen, *Catalyst: NH_3 as an Energy Carrier.* Chem, 2017. **3**(5): p. 709-712.
75. Chang, F., et al., *Alkali and Alkaline Earth Hydrides-Driven N_2 Activation and Transformation over Mn Nitride Catalyst.* Journal of the American Chemical Society, 2018. **140**(44): p. 14799-14806.
76. Luo, Q., et al., *A review on the synthesis of transition metal nitride nanostructures and their energy related applications.* Green Energy & Environment, 2023. **8**(2): p. 406-437.
77. Michalsky, R. and P.H. Pfromm, *An Ionicity Rationale to Design Solid phase Metal Nitride Reactants for Solar Ammonia Production.* Journal of Physical Chemistry C, 2012. **116**(44): p. 23243-23251.
78. Michalsky, R., P.H. Pfromm, and A. Steinfeld, *Rational design of metal nitride redox materials for solar-driven ammonia synthesis.* Interface Focus, 2015. **5**(3).
79. Wu, Y., et al., *Fe_2O_3, a cost effective and environmentally friendly catalyst for the generation of NH_3 - a future fuel - using a new Al_2O_3-looping based technology.* Chemical Communications, 2017. **53**(77): p. 10664-10667.
80. Gálvez, M.E., M. Halmann, and A. Steinfeld, *Ammonia production via a two-step Al_2O_3/AlN thermochemical cycle. 1. Thermodynamic, environmental, and economic analyses.* Industrial & Engineering Chemistry Research, 2007. **46**(7): p. 2042-2046.
81. Gálvez, M.E., et al., *Ammonia production via a two-step Al_2O_3/AlN thermochemical cycle. 2. Kinetic analysis.* Industrial & Engineering Chemistry Research, 2007. **46**(7): p. 2047-2053.
82. Gálvez, M.E., et al., *Ammonia Production via a Two-Step Al_2O_3/AlN Thermochemical Cycle. 3. Influence of the Carbon Reducing Agent and Cyclability.* Industrial & Engineering Chemistry Research, 2008. **47**(7): p. 2231-2237.
83. Wang, B.Y., et al., *N-Sorption Capability of Al_2O_3-Supported Mn-/Fe-Based Nitrogen Carriers during Chemical Looping Ammonia Synthesis Technology.* Energy & Fuels, 2020. **34**(8): p. 10247-10255.

84. Wang, X.Y., M.Z. Su, and H.B. Zhao, *Process design and exergy cost analysis of a chemical looping ammonia generation system using AlN/Al_2O_3 as a nitrogen carrier.* Energy, 2021. **230**.
85. Lyngfelt, A., *Chemical-looping combustion of solid fuels - Status of development.* Applied Energy, 2014. **113**: p. 1869-1873.
86. Mckay, D., et al., *Towards nitrogen transfer catalysis: reactive lattice nitrogen in cobalt molybdenum nitride.* Chemical Communications, 2007(29): p. 3051-3053.
87. Al Sobhi, S., et al., *The reactivity of lattice nitrogen within the Ni_2Mo_3N and $NiCoMo_3N$ phases.* Materials Research Bulletin, 2019. **118**.
88. Bion, N., et al., *The role of preparation route upon the ambient pressure ammonia synthesis activity of Ni_2Mo_3N.* Applied Catalysis a-General, 2015. **504**: p. 44-50.
89. Alexander, A.M., J.S.J. Hargreaves, and C. Mitchell, *The Reduction of Various Nitrides under Hydrogen: Ni_3N, Cu_3N, Zn_3N_2 and Ta_3N_5.* Topics in Catalysis, 2012. **55**(14-15): p. 1046-1053.
90. Alexander, A.M., J.S.J. Hargreaves, and C. Mitchell, *The Denitridation of Nitrides of Iron, Cobalt and Rhenium Under Hydrogen.* Topics in Catalysis, 2013. **56**(18-20): p. 1963-1969.
91. Michalsky, R., et al., *Chemical looping of metal nitride catalysts: low-pressure ammonia synthesis for energy storage.* Chemical Science, 2015. **6**(7): p. 3965-3974.
92. Hua, J.L., et al., *Feasibility of Fe-based nitrogen carrier for chemical looping ammonia synthesis: thermodynamics.* Journal of Thermal Analysis and Calorimetry, 2021. **146**(2): p. 673-680.
93. Yang, S., et al., *Molybdenum-based nitrogen carrier for ammonia production via a chemical looping route.* Applied Catalysis B-Environmental, 2022. **312**.
94. Hargreaves, J.S.J. and D. McKay, *A comparison of the reactivity of lattice nitrogen in Co_3Mo_3N and Ni_3Mo_3N catalysts.* Journal of Molecular Catalysis a-Chemical, 2009. **305**(1-2): p. 125-129.
95. McEnaney, J.M., et al., *Ammonia synthesis from N_2 and H_2O using a lithium cycling electrification strategy at atmospheric pressure.* Energy & Environmental Science, 2017. **10**(7): p. 1621-1630.
96. Ghasem, N., *Chapter nine - Production of ammonia via chemical looping process based on metal imides as nitrogen carriers*, in *Progresses in Ammonia: Science, Technology and Membranes*, A. Basile and M.R. Rahimpour, Editors. 2024, Elsevier. p. 205-219.
97. Fu, E.K., et al., *Chemical Looping Technology in Mild-Condition Ammonia Production: A Comprehensive Review and Analysis.* Small, 2024. **20**(1).
98. Wang, Q.R., et al., *Hydrides mediate nitrogen fixation.* Cell Reports Physical Science, 2022. **3**(3).

99. Ravi, M. and J.W. Makepeace, *Facilitating green ammonia manufacture under milder conditions: what do heterogeneous catalyst formulations have to offer?* Chemical Science, 2022. **13**(4): p. 890-908.
100. Ravi, M. and J.W. Makepeace, *Lithium-nitrogen-hydrogen systems for ammonia synthesis: exploring a more efficient pathway using lithium nitride-hydride.* Chemical Communications, 2022. **58**(41): p. 6076-6079.
101. Tagawa, K., et al., *Improvement of Kinetics of Ammonia Synthesis at Ambient Pressure by the Chemical Looping Process of Lithium Hydride.* Journal of Physical Chemistry C, 2022. **126**(5): p. 2403-2409.
102. Hu, Y.H. and E. Ruckenstein, *Ultrafast reaction between Li_3N and $LiNH_2$ to prepare the effective hydrogen storage material Li_2NH.* Industrial & Engineering Chemistry Research, 2006. **45**(14): p. 4993-4998.
103. Gao, W.B., et al., *Barium hydride activates Ni for ammonia synthesis catalysis.* Faraday Discussions, 2023. **243**(0): p. 27-37.
104. Guan, Y.Q., et al., *Transition-Metal-Free Barium Hydride Mediates Dinitrogen Fixation and Ammonia Synthesis.* Angewandte Chemie-International Edition, 2022. **61**(39).
105. Jepsen, L.H., et al., *Thermal decomposition of sodium amide, $NaNH_2$, and sodium amide hydroxide composites, $NaNH_2$ - NaOH.* Physical Chemistry Chemical Physics, 2016. **18**(36): p. 25257-25264.
106. Hino, S., et al., *Hydrogen desorption properties of the Ca-N-H system.* Journal of Alloys and Compounds, 2005. **398**(1-2): p. 62-66.
107. Nakamori, Y., G. Kitahara, and S. Orimo, *Synthesis and dehydriding studies of Mg-N-H systems.* Journal of Power Sources, 2004. **138**(1-2): p. 309-312.
108. Gao, W., et al., *Thermodynamic and kinetic considerations of nitrogen carriers for chemical looping ammonia synthesis.* Discover Chemical Engineering, 2023. **3**(1): p. 1.
109. Jafari, A., A. Ebadi, and S. Sahebdelfar, *Effect of iron oxide precursor on the properties and ammonia synthesis activity of fused iron catalysts.* Reaction Kinetics Mechanisms and Catalysis, 2019. **126**(1): p. 307-325.
110. Fan, H., et al., *In-Situ Formation of Fe Nanoparticles from FeOOH Nanosheets on γ-Al_2O_3 as Efficient Catalysts for Ammonia Synthesis.* ACS Sustainable Chemistry & Engineering, 2017. **5**(11): p. 10900-10909.
111. Sato, K., et al., *A low-crystalline ruthenium nano-layer supported on praseodymium oxide as an active catalyst for ammonia synthesis.* Chemical Science, 2017. **8**(1): p. 674-679.
112. Javaid, R., H. Matsumoto, and T. Nanba, *Influence of Reaction Conditions and Promoting Role of Ammonia Produced at Higher Temperature Conditions in Its Synthesis Process over Cs-Ru/MgO Catalyst.* Chemistryselect, 2019. **4**(7): p. 2218-2224.

113. Xiong, C.H., et al., *High thermal stability Si-Al based N-carrier for efficient and stable chemical looping ammonia generation.* Applied Energy, 2022. **323**.
114. Wu, Y., et al., *Promising zirconia-mixed Al-based nitrogen carriers for chemical looping of NH_3: Reduced NH_3 decomposition and improved NH_3 yield.* Fuel, 2020. **264**.
115. Heidlage, M.G., et al., *Thermochemical Synthesis of Ammonia and Syngas from Natural Gas at Atmospheric Pressure.* Industrial & Engineering Chemistry Research, 2017. **56**(47): p. 14014-14024.
116. Sun, Z., et al., *Ammonia synthesis via chromium-based nitrogen carrier looping.* Chemical Engineering Journal, 2023. **476**.
117. Kim, K., et al., *Electrochemical Synthesis of Ammonia from Water and Nitrogen: A Lithium-Mediated Approach Using Lithium-Ion Conducting Glass Ceramics.* Chemsuschem, 2018. **11**(1): p. 120-124.
118. Swearer, D.F., et al., *Light-Driven Chemical Looping for Ammonia Synthesis.* ACS Energy Letters, 2019. **4**(7): p. 1505-1512.
119. Laassiri, S., et al., *The potential of manganese nitride based materials as nitrogen transfer reagents for nitrogen chemical looping.* Applied Catalysis B-Environmental, 2018. **223**: p. 60-66.
120. Xiong, Z.T., et al., *Investigations into the interaction between hydrogen and calcium nitride.* Journal of Materials Chemistry, 2003. **13**(7): p. 1676-1680.
121. Laassiri, S., et al., *Nitrogen transfer properties in tantalum nitride based material.* Catalysis Today, 2017. **286**: p. 147-155.
122. Goto, Y., A. Daisley, and J.S.J. Hargreaves, *Towards anti-perovskite nitrides as potential nitrogen storage materials for chemical looping ammonia production: Reduction of Co_3ZnN, Ni_3ZnN, Co_3InN and Ni_3InN under hydrogen.* Catalysis Today, 2021. **364**: p. 196-201.
123. Yamaguchi, S., et al., *Nitrogen Dissociation via Reaction with Lithium Alloys.* ACS Omega, 2017. **2**(3): p. 1081-1088.
124. Yan, H.X., et al., *Lithium Palladium Hydride Promotes Chemical Looping Ammonia Synthesis Mediated by Lithium Imide and Hydride.* Journal of Physical Chemistry C, 2021. **125**(12): p. 6716-6722.
125. Wang, R.Z., et al., *Zn Promotes Chemical Looping Ammonia Synthesis Mediated by LiH-Li_2NH Couple.* Chemsuschem, 2023. **16**(22).
126. Feng, S., et al., *Electrodriven Chemical Looping Ammonia Synthesis Mediated by Lithium Imide.* ACS Energy Letters, 2023: p. 1567-1574.
127. Wu, H., et al., *Plasma-Driven Nitrogen Fixation on Sodium Hydride.* Advanced Energy Materials, 2023. **13**(27).
128. Wang, P.K., et al., *Breaking scaling relations to achieve low-temperature ammonia synthesis through LiH-mediated nitrogen transfer and hydrogenation.* Nature Chemistry, 2017. **9**(1): p. 64-70.

129. Brown, S., et al., *Ambient Carbon-Neutral Ammonia Generation via a Cyclic Microwave Plasma Process.* ACS Applied Materials & Interfaces, 2023. **15**(19): p. 23255-23264.
130. Pfromm, P.H. and W. Aframehr, *Green ammonia from air, water, and renewable electricity: Energy costs using natural gas reforming, solid oxide electrolysis, liquid water electrolysis, chemical looping, or a Haber-Bosch loop.* Journal of Renewable and Sustainable Energy, 2022. **14**(5).
131. Perry, J., et al., *Perovskite-support enhanced metal hydride chemical looping ammonia synthesis.* International Journal of Hydrogen Energy, 2026. **198**: p. 152673.
132. Liu, L. and X.B. Chen, *Titanium Dioxide Nanomaterials: Self-Structural Modifications.* Chemical Reviews, 2014. **114**(19): p. 9890-9918.
133. Zhang, T.T., X.B. Zhang, and F. Chang, *Synergistic Photothermal Acceleration of Ammonia Synthesis Using Defective TiO_2 Supported Ru Catalysts.* Industrial & Engineering Chemistry Research, 2025. **64**(30): p. 14879-14887.
134. Ren, W.T., et al., *Sea urchin-like NiPt/$TiCeO_2$ catalyst for rapid and efficient hydrogen production from hydrous hydrazine.* Journal of Rare Earths, 2025. **43**(8): p. 1668-1676.
135. Subraveti, S.G., et al., *Machine Learning-Based Multiobjective Optimization of Pressure Swing Adsorption.* Industrial & Engineering Chemistry Research, 2019. **58**(44): p. 20412-20422.
136. Mukherjee, R. and U.M. Diwekar, *Multi-objective Optimization of the TEG Dehydration Process for BTEX Emission Mitigation Using Machine-Learning and Metaheuristic Algorithms.* Acs Sustainable Chemistry & Engineering, 2021. **9**(3): p. 1213-1228.
137. Duan, Z.C., et al., *Building retrofit multiobjective optimization using neural networks and genetic algorithm three for energy carbon and comfort.* Scientific Reports, 2025. **15**(1).
138. Yu, Z.Y., et al., *Machine learning-driven prediction of coal pyrolysis product distribution and multi-objective optimisation of Pareto frontier.* Energy, 2026. **359**.
139. Sin, G., *Global sensitivity analysis using Monte Carlo estimation under fat-tailed distributions.* Chemical Engineering Science, 2024. **294**.